5-2017

Infrared Energy Conversion in Plasmonic Fields at Two-Dimensional Semiconductors

Gregory Thomas Forcherio
University of Arkansas, Fayetteville

Recommended Citation

Forcherio, Gregory Thomas, "Infrared Energy Conversion in Plasmonic Fields at Two-Dimensional Semiconductors" (2017). *Theses and Dissertations*. 1896.
http://scholarworks.uark.edu/etd/1896

Infrared Energy Conversion in Plasmonic Fields at Two-Dimensional Semiconductors

A dissertation submitted in partial fulfillment
of the requirements for the degree of
Doctor of Philosophy in Microelectronics-Photonics

by

Gregory Thomas Forcherio
Southeast Missouri State University
Bachelor of Science in Engineering Physics and Mathematics, 2012
University of Arkansas
Master of Science in Microelectronics-Photonics, 2014

May 2017
University of Arkansas

This dissertation is approved for recommendation to the Graduate Council.

Dr. D. Keith Roper
Dissertation Director

Dr. Gregory J. Salamo Committee Member	Dr. Surendra P. Singh Committee Member
Dr. Hameed A. Naseem Committee Member	Dr. Rick L. Wise Ex-Officio Member

The following signatories attest that all software used in this dissertation was legally licensed for use by Mr. Gregory T. Forcherio for research purposes and publication.

Mr. Gregory T. Forcherio Student	Dr. D. Keith Roper Dissertation Director

This dissertation was submitted to http://www.turnitin.com for plagiarism review by the TurnItIn company's software. The signatories have examined the report on this dissertation that was returned by TurnItIn and attest that, in their opinion, the items highlighted by the software are incidental to common usage and are not plagiarized material.

Dr. Rick L. Wise Program Director	Dr. D. Keith Roper Dissertation Director

ABSTRACT

Conversion of infrared energy within plasmonic fields at two-dimensional, semiconductive transition metal dichalcogenides (TMD) through plasmonic hot electron transport and nonlinear frequency mixing has important implications in next-generation optoelectronics. Drude-Lorentz theory and approximate discrete dipole (DDA) solutions to Maxwell's equations guided metal nanoantenna design towards strong infrared localized surface plasmon resonance (LSPR). Excitation and damping dynamics of LSPR in heterostructures of noble metal nanoantennas and molybdenum- or tungsten-disulfide (MoS_2; WS_2) monolayers were examined by parallel synthesis of (i) DDA electrodynamic simulations and (ii) near-field electron energy loss (EELS) and far-field optical transmission UV-vis spectroscopic measurements. Susceptibility to second-order nonlinear frequency conversion processes, $\chi^{(2)}$, for monolayer MoS_2 and WS_2 were measured to be 660±130 pm V^{-1} and 280±18 pm V^{-1}, respectively, by Hyper Rayleigh Scattering. Femtosecond conversion of resonant irradiation to injection of plasmonic hot electrons into the TMD were measured in EELS at a maximum of 11±5% quantum efficiency for an optimized physicochemical Au-WS_2 junction. Measured nonlinear second harmonic generation (SHG) from a ca. 1 µm MoS_2 monolayer was enhanced 17-84% by local electric field augmentation from a single 150 nm Au nanoshell to a conversion efficiency of up to 0.023% W^{-1}. Capacitive coupling between nanoshells arranged into dimers further augmented SHG activity from MoS_2. New theoretical and experimental insights into energy conversion interactions between coupled plasmonic and excitonic materials spanning the linear and nonlinear optical regimes were established towards their implementation as an optoelectronic platform.

ACKNOWLEDGEMENTS

The completion of this dissertation would not have been possible without the generosity, patience, and inspiration from many people. Foremost, I want to thank my advisor, Dr. Keith Roper for his guidance and mentorship. I am indebted to his belief in my abilities as a researcher and providing me the opportunity to pursue a graduate degree. I am grateful for the strong collaborative interactions with my colleagues in the NanoBio Photonics group; especially Dr. Phillip Blake, and Dr. Drew DeJarnette, and Jeremy Dunklin. Contributive efforts from other colleagues and innumerous undergraduates, no matter how minimal, have not been taken for granted. I would like to thank my committee members, Drs. Surendra Singh, Greg Salamo, and Hameed Naseem, for their valuable feedback in support of this dissertation.

I graciously thank Drs. Luigi Bonacina and Jean-Pierre Wolf at the University of Geneva and Dr. Ronan Le Dantec at University of Savoy Mont Blanc for their generous participation in my work, willingness to host me abroad, and open use of their nonlinear optics facilities. I am grateful to Dr. Mourad Benamara for his time spent dedicated to my transmission electron microscopy training. I appreciate the oversight from Dr. Vasyl Kilin in multi-photon confocal microscopy and the Hyper Rayleigh Scattering measurements from Jérémy Riporto. I thank Drs. Claudia Backes and Yana Vaynzof at University Heidelberg for providing novel, *in situ* synthesized samples to use in my work. Encouragement from Drs. Dave Probst, Peggy Hill, and Jian Peng at Southeast Missouri State University and Dr. Mark Lundstrom at Purdue University sharpened my focus to pursue research at the University of Arkansas.

Lastly, I want to express my most sincere thanks to my family for their love and unwavering encouragement. I owe more than I can express in words to my wife, Heather, who

has been unconditionally patient over the past five years with the long hours and weekend nights spent completing this dissertation. My parents, Chris and Brenda, inspired me to be my very best since I was a child. Completion of this dissertation would not have been possible without them.

Financial Support. I am forever indebted to the organizations who financially invested in my research endeavors and professional development; in particular, the National Science Foundation Graduate Research Fellowship Program and the University of Arkansas Graduate School and Department of Chemical Engineering. Any opinions, findings, and conclusions expressed in this dissertation are my own and do not necessarily reflect the views of the National Science Foundation.

DEDICATION

I dedicate this dissertation to my precious daughter, Emma, who makes my work more meaningful with each smile.

TABLE OF CONTENTS

CHAPTER 1

INTRODUCTION

CHAPTER 2

SURFACE PLASMON PHOTONICS

CHAPTER 3

TWO-DIMENSIONAL TRANSITION METAL DICHALCOGENIDES

CHAPTER 4

INTERFACING MONOLAYER TRANSITION METAL DICHALCOGENIDES WITH NANOANTENNAS

CHAPTER 5

ENERGY CONVERSION BY PLASMONIC HOT ELECTRON TRANSPORT

CHAPTER 6

SURFACE PLASMON-ENHANCED NONLINEAR ENERGY MIXING

CHAPTER 7

CONCLUDING REMARKS

LIST OF FIGURES

LIST OF TABLES

LIST OF NOMENCLATURE

Acronyms & Abbreviations

Al	Aluminum
Al:ZnO	Aluminum-Doped Zinc Oxide
AFM	Atomic Force Microscopy
BSE	Bethe-Salpeter Exciton Method
BEM	Boundary Element Method
CCD	Charge-Coupled Device
CVD	Chemical Vapor Deposition
CDA	Coupled Dipole Approximation
CLR	Coupled Lattice Resonance
CMOS	Complementary Metal-Oxide Semiconductor
Cu	Copper
DFT	Density Functional Theory
DMT	Density Matrix Theory
DDA	Discrete Dipole Approximation
DFG	Difference Frequency Generation
DLS	Dynamic Light Scattering
EELS	Electron Energy Loss Spectroscopy
EFTEM	Energy-Filtered Transmission Electron Microscopy
ELDOS	Electromagnetic Local Density of States
FFT	Fast-Fourier Transform
FDTD	Finite Difference Time Domain
FEM	Finite Element Method
FWHM	Full Width at Half Maximum

Ga:ZnO	Gallium-Doped Zinc Oxide
GIF	GATAN Post-Column Imaging Filter
Au	Gold
$AuCl_3$	Gold Chloride
AuNA	Gold Nanoantenna
AuNS	Gold Nanosphere or Nanoshell
HAADF	High-Angle Annular Dark-Field
HRS	Hyper Rayleigh Scattering
InSb	Indium Antimonide
InAs	Indium Arsenide
ITO	Indium Tin Oxide
LSP	Localized Surface Plasmon
LSPR	Localized Surface Plasmon Resonance
MoS_2	Molybdenum Disulfide
$MoSe_2$	Molybdenum Diselenide
MoO_3	Molybdenum Trioxide
Nd:YAG	Neodynmium-doped Yttrium Aluminum Garnet
NiSi	Nickel Silicide
1D	One-Dimensional
OR	Optical Rectification
pNA	Para-Nitroaniline
PL	Photoluminescence
PMT	Photomultiplier Tube
PVP	Poly(vinylpyrrolidone)
SEM	Scanning Electron Microscopy

Ag	Silver
SFG	Sum Frequency Generation
SH	Second Harmonic
SHG	Second Harmonic Generation
SiO_x	Silica
SiO_2	Silicon Dioxide
STEM	Scanning Transmission Electron Microscopy
TiN	Titanium Nitride
TiSi	Titanium Silicide
TEM	Transmission Electron Microscopy
TMD	Transition Metal Dichalcogenide
WS_2	Tungsten Disulfide
WSe_2	Tungsten Diselenide
2D	Two-Dimensional
UV-vis	Ultraviolet-visible
XPS	X-Ray Photoelectron Spectroscopy
ZnO	Zinc Oxide
ZrN	Zirconium Nitride

Symbols

σ_{abs}	Absorption Cross Section [m^{2}]
σ_{TMD}	Beer-Lambert Absorption Correction Factor for TMD [m^{3}]
N	Carrier Concentration [m^{-3}]
C	Concentration [m^{-3}]
$p^{(n)}$	Dipole Moment Polarization [C m]
A	Dipole-Dipole Interaction Matrix [V m C^{-1}]

$\hbar$	Dirac Constant [eV s or J s]
γ	Drude Damping Rate [eV]
m_o	Effective Electron Mass [g]
α_{eff}	Effective Polarizability [C m^2 V^{-1}]
E	Electric Field [V m^{-1}]
F	Electric Field Enhancement Factor [unitless]
ϵ	Electric Permittivity [unitless]
$\chi^{(n)}$	Electric Susceptibility [n = 1, unitless; n = 2, m V^{-1}; n = 2, m^2 V^{-2}…]
qχ	Electron Affinity [eV]
e	Electron Charge [C]
m	Electron Mass [g]
G	Experimental Constant [unitless]
σ_{ext}	Extinction Cross Section [m^2]
ω & λ	Frequency or Wavelength of Light [m, eV, or s^{-1}]
Γ	Full Width at Half Maximum [m or eV]
β	Hyperpolarizablity [m^4 V^{-1} or esu]
α_{TMD} & α_{pNA}	Hyper Rayleigh Scattering vs. Species Concentration Slope [a.u. m^3]
I	Intensity [W m^{-2} or a.u.]
d	Inter-Atomic or Inter-Dipole Separation [m]
L	Length of Nonlinear Crystal [m]
L_{TMD}	Mean Length [m]
N_{TMD}	Mean Layer Number [unitless]
X	Measured Second Harmonic Generation Enhancement Factor [unitless]
qϕ	Metal Work Function [eV]
η_{norm}	Normalized Second Harmonic Conversion Efficiency [W^{-1}]
ϵ_o	Permittivity of Free Space [F m^{-1}]
ω_p	Plasma Frequency [m, eV, or s^{-1}]
α	Polarizability [C m^2 V^{-1}]
$P^{(n)}$	Polarization Density [C m^{-2}]
η	Quantum Efficiency of Plasmon Damping Mechanism [unitless]
n	Refractive Index [unitless]
S	Retarded Dipole Sum [V C^{-1} m^{-2}]

σ_{sca}	Scattering Cross Section [m^2]
$q\phi_{SB}$	Schottky Barrier [eV]
$\eta_{2\omega}$	Second Harmonic Conversion Efficiency [unitless]
c	Speed of Light [$m\ s^{-1}$]
T_2	Surface Plasmon Dephasing Time [s]
V	Volume of Nanoparticle [m^3]
k	Wave Vector [m^{-1}]

CHAPTER 1

INTRODUCTION

Advancements in solar photovoltaic, wind turbine, geothermal, and biofuel technologies have decreased proportional fossil fuel dependence by 10% over the past half century.[1] Policies enacted by the International Energy Agency aim for a 160 gigatonne reduction in carbon dioxide emissions with 33% capacity increase by 2035 to accommodate a population nearing 9 billion.[1–3] Despite progress of alternative energies, nearly 60% of generated energy is lost to heat.[4,5] Recovery of waste heat potentiates an emission-free 10 terawatt reduction in energy demand,[5,6] motivating ample research in thermoelectric materials and thermophotovoltaics since the 1950s.[7–10] However, efficiencies and balance-of-system costs inherent to these methods have limited their implementation to niche markets undeterred by high investment capital.[4,8,11] Herein, two alternative schemes unique to an emerging class of materials which could allow conversion, and utilization, of radiative waste heat through optical resonances are studied.

1.1 Motivation

In addition to decarbonization of energy resources, the U.S. Department of Energy advocates decreasing device power consumption is essential to a sustainable future.[1] Energy consumption and processing speed of electronic transistors improved with geometric downscaling according to Moore’s Law for over 40 years. However, progress today is limited by ohmic heat confined at sub-50 nm transistor nodes.[12] Dissipation traditionally relies on forced convection, conduction, and/or evaporation. Dissipation by radiation could provide additional, parallel rejection processes with rapid dynamics not requiring additional equipment or contact.

Recycling infrared photons radiated by electronic components provides opportunities to enhance heat rejection and integrate electro-optical interconnects into the next-generation of optoelectronic devices. Optical interconnection between electronic transistors avoids ohmic losses at 10^3x higher data densities while offering additional processing capabilities, such as wavelength-division multiplexing.[12,13] Interconnects comprise 80% of total microprocessor energy consumption.[13] Inefficient emission from bulk silicon in the visible to near-infrared spectrum and size of existing optic-electronic transition components has precluded hybrid electronic and optic operations.[12–14] Concomitant conversion of heat into electrical signals beyond the Seebeck effect[8] could augment rejection and diversify signal functions. A material with engineered optical resonance characteristics to enable conversion of energy between frequencies or signal modality (i.e., electric or optic) could provide a new optoelectronic material platform.

1.2 Hypothesis

Resonant photon-electron interactions in nanomaterials could support passive infrared energy conversion mechanisms for optoelectronics beyond conventional thermodynamic paths:

- conversion of infrared energy into hot carriers
- nonlinear frequency conversion toward higher energies

1.3 Hot Carrier Generation

Optical resonances of sub-wavelength metal architectures, called nanoantennas, generate energetically hot electrons through plasmon excitation. Incident electromagnetism at the energy which a nanoantenna is intrinsically resonant (determined by structural morphology and elemental composition) induces collective oscillations of its free electrons, known as a localized surface plasmon resonance (LSPR).[12,15] Relaxation, or damping, of the LSPR initiates transfer of its energy into hot electron-hole pairs in the metal through Landau damping over 1-100 fs.[16] "Hot" attribution refers to the energy of the carrier exceeding its thermal energy (on order of 10^{-2} eV).

Nonradiative relaxation of plasmonic hot electrons traditionally offers two pathways: (i) phonon scattering into the metal as the carriers fall back to the Fermi level and (ii) interfacial interactions (e.g., entrapment into defects). [17–21] A semiconductor in near proximity to the metal nanoantenna can serve as an acceptor for hot electrons, thus offering an additional relaxation pathway.[16,22,23] Figure 1.1 shows an energy band diagram for a metal-semiconductor interface. Conduction band of the semiconductor may accept plasmonic hot electrons when their energy exceeds the metal-semiconductor Schottky barrier, $q\phi_{SB}$.[22] The Schottky barrier is equal to the difference between the metal work function, $q\phi$, and semiconductor electron affinity, $q\chi$, viz.[24]

$$q\phi_{SB} = q\phi - q\chi \quad . \qquad \text{(Equation 1.1)}$$

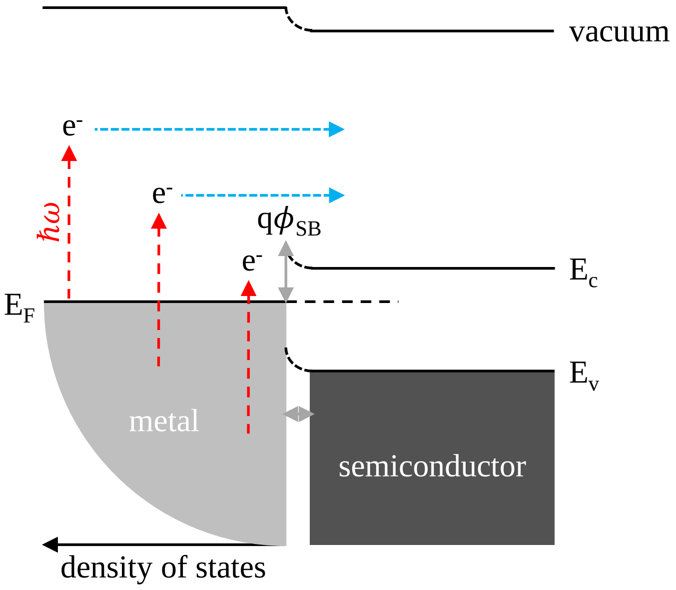

Figure 1.1: Energy band diagram of an unbiased metal-semiconductor junction at thermal equilibrium, signifying contact between a metal nanoantenna and an adjacent semiconductor. Resonant plasmon excitation, of energy $\hbar\omega$, on the metal nanoantenna generates hot electrons, which may transfer into the semiconductor if their energy exceeds the Schottky barrier ($q\phi_{SB}$).

Conversion of infrared energy exceeding the Schottky barrier through transduction into plasmonic hot electrons followed by transport into a semiconductor represents one possible heat rejection mechanism beyond conventional thermodynamic paths. Within the context of optoelectronic devices, radiated waste heat could be converted into electric signals. Reports estimate transport efficiency of plasmonic hot electrons from metals to titanium dioxide, aluminum-doped zinc oxide, or cadmium sulfide at 2-10%.[25–27] Radiative recombination of hot electrons transported into a semiconductor quantum well has been proposed as an energy upconversion scheme, with theoretical efficiency as high as 25% for 5 nm silver nanocubes.[28] In such a scheme, recombination across the semiconductor bandgap allows re-radiation at a higher energy than the initial photon exciting the plasmonic hot electron (energy as low as qϕ_{SB}). Photocurrent from plasmonic hot electrons has also been utilized in photodetector schemes[29] and catalysis processes, such as the hydrogen evolution reaction.[30]

1.4 Nonlinear Optical Frequency Mixing

The optical behavior of a material can be described by its polarization in response to an incident electromagnetic field. Macroscopic polarization density, $\boldsymbol{P}$, of a material is driven by applied electric fields, $\boldsymbol{E}$, with strength given by the product of free space permittivity, ϵ_o and its intrinsic electric susceptibility, χ.[31] However, a more rigorous description of electric polarization reveals that total polarization is a sum of distinct n^{th}-order polarizations where $n \in \mathbb{N}$, *viz.*

$$\begin{aligned} \boldsymbol{P} &= \sum_{n=1}^{N} \boldsymbol{P}^{(n)} = \epsilon_o \sum_{n=1}^{N} \chi^{(n)} \boldsymbol{E}^n \qquad \text{(Equation 1.2)} \\ &= \epsilon_o\left(\chi \boldsymbol{E} + \chi^{(2)}\boldsymbol{E}^2 + \chi^{(3)}\boldsymbol{E}^3 + \cdots + \chi^{(N)}\boldsymbol{E}^N\right) \end{aligned}$$

and $\chi^{(n)}$ are the n^{th}-order electric susceptibilities,[32,33] assuming a dispersionless material. Polarization of the first-order (i.e., $n = 1$) is referred to as the linear optical response. Higher order polarizations which do not scale linearly with the applied electric field (i.e., $n \neq 1$) are responsible for nonlinear optical behavior. Time-varying nonlinear polarization of charge creates new frequency components in the radiated electromagnetic field, referred to as frequency mixing.[33] This work focuses on frequency mixing phenomena arising from the 2nd-order nonlinear response as a possible radiative heat rejection mechanism beyond conventional thermodynamic paths.

1.4.1 Electrodynamic Theory

Consider the simplistic case of simultaneous irradiation of a nonlinear material with two different frequencies of light. Time-variant second-order nonlinear polarization in response to the excitation electric fields (given by $\boldsymbol{E}(t) = E_1 e^{-i\omega_1 t} + E_2 e^{-i\omega_2 t} + c.c.$) takes the form

$$\begin{aligned}\boldsymbol{P}^{(2)}(t) = \epsilon_o \chi^{(2)} \big[& {E_1}^2 e^{-i2\omega_1 t} + {E_2}^2 e^{-i2\omega_2 t} + 2E_1 E_2 e^{-i(\omega_1+\omega_2)t} \\ & + 2E_1 E_2^* e^{-i(\omega_1-\omega_2)t} + (E_1 E_1^* + E_2 E_2^*) e^0 + c.c. \big]\end{aligned} \qquad \text{(Equation 1.3)}$$

with dipole oscillation frequencies at $2\omega_1$, $2\omega_2$, $\omega_1 + \omega_2$, $\omega_1 - \omega_2$, and 0. Derivation of the wave equation from Faraday's and Ampere's Laws (assuming nonmagnetic material with no free currents) for optically nonlinear materials shows each frequency component in $\boldsymbol{P}^{(2)}$ acts as a source of electromagnetic radiation, *viz.*[33]

$$\nabla^2 \boldsymbol{E} - \frac{n^2}{c^2} \frac{\partial^2 \boldsymbol{E}}{\partial t^2} = \frac{1}{\epsilon_o c^2} \frac{\partial^2 \boldsymbol{P}^{(2)}}{\partial t^2} \qquad \text{(Equation 1.4)}$$

where n is the refractive index of the material and c is the speed of light. Larmor's theorem states that electromagnetic radiation emitted from a material originates from accelerated charges polarized within the material,[31] consistent with the $\partial^2 \boldsymbol{P}^{(2)} / \partial t^2$ term in Equation 1.4.

Intensity of nonlinear radiation from the excited material is dependent on the collective phase for each oscillating dipole relative to phase of the excitation fields as they propagate through the material.[32,33] If the excitation fields are given by $\boldsymbol{E}(t) = E_1 e^{-i(k_1 x - \omega_1 t)} + E_2 e^{-i(k_2 x - \omega_2 t)} + c.c.$ at some point x in the material (along the propagation vector), then observed intensity of the new frequency component ω_3 depends on the phase condition $k_3 = k_1 + k_2$. Intensity of the nonlinearly-generated radiation at ω_3 is directly proportional to the phase coherence Δk via[33]

$$I_3 \propto \left[\chi^{(2)}\right]^2 I_1 I_2 L^2 \operatorname{sinc}^2\left(\frac{\Delta k x}{2}\right) \qquad \text{(Equation 1.5)}$$

where I_1 and I_2 are the excitation intensities. Under this notation, the quantity $2/\Delta k$ is defined as the phase coherence length. After integrating Equation 1.5 over the length of the material, L, the characteristic length for constructive coherence leading to maximum I_3 is given by

$$L_{coh} \equiv \frac{2}{\Delta k} = \frac{2c}{n_1\omega_1 + n_2\omega_2 - n_3\omega_3}\ . \qquad \text{(Equation 1.6)}$$

In the case of frequency doubling ($\omega_3 = 2\omega_1$ or $2\omega_2$), the characteristic L_{coh} simplifies to:

$$L_{coh} = \frac{\lambda_\omega}{2\pi(n_\omega - n_{2\omega})} \qquad \text{(Equation 1.7)}$$

which highlights utilization of nanomaterials for nonlinear optics. Phase matching can be neglected for materials with dimension beneath the wavelength scale, e.g., ca. 1-10 µm for infrared irradiation, since the phase of radiating dipoles are always coherent. In the case of infrared irradiation, L_{coh} is generally on the order of microns.

1.4.2 Second-Order Frequency Conversion Processes

Second-order nonlinear interactions between a material and light intrinsically results in new frequency sources radiated from the material, called frequency mixing. The processes of creating radiation at $2\omega_1$, $2\omega_2$, $\omega_1 + \omega_2$, $\omega_1 - \omega_2$, and 0 frequencies are referred to as nonlinear second harmonic generation (SHG), sum frequency generation (SFG), difference frequency generation (DFG), and optical rectification (OR), respectively.[32,33] Each process is shown schematically in Figure 1.2. The energy of two distinct photons combine and re-radiate as a single photon in SHG and SFG. Energy of a single high frequency photon can re-radiate as two photons in DFG with energy-conserved components of (i) the incident lower frequency (referred to as optical parametric amplification of ω_2) and (ii) the difference frequency. A static electric field across the material is created in OR.

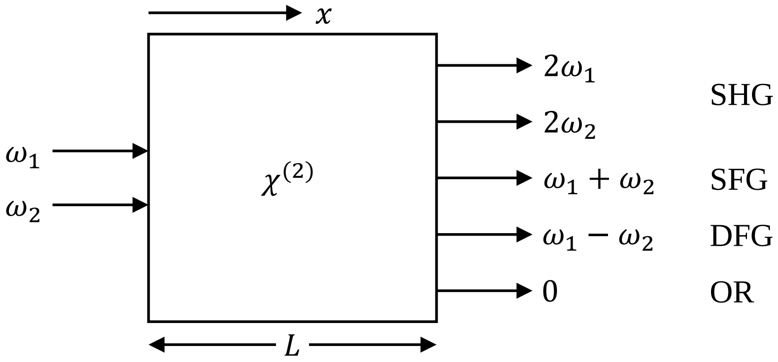

Figure 1.2: Schematic representation of frequency mixing processes arising from second-order nonlinear interaction of a material with two excitation frequencies, ω_1 and ω_2.

Nonlinear frequency mixing was first observed in 1961 by Franken *et al*. using quartz to generate the second harmonic (SH) of a ruby laser.[34] Underlying electrodynamic relations for SHG and other nonlinear processes were developed by Bloemberg *et al*.[35] in 1962 following successive discoveries of SFG, DFG, and OR in potassium dihydrogen phosphate crystals.[36,37] Frequency conversion processes have since become a foundation for fiber-based telecommunication systems, wavelength-tunable lasers,[38] materials characterization,[39] and advanced microscopy[40] and tomography[41] techniques for examining biological entities.

Observation of second-order frequency mixing phenomena is limited to materials whose intrinsic crystal structure is non-centrosymmetric; in other words, the time-averaged nonlinear polarization is zero for centrosymmetric materials. Nonlinear atomic polarization $\boldsymbol{P}^{(2)}$ of a centrosymmetric crystal generates opposing dipole moments equal in magnitude as the excitation electric field oscillates (i.e., from +$\boldsymbol{E}$ to –$\boldsymbol{E}$) with time. Hence,

$$-\boldsymbol{P}^{(2)} = \epsilon_o \chi^{(2)} [-\boldsymbol{E}]^2 = \epsilon_o \chi^{(2)} \boldsymbol{E}^2 \qquad \text{(Equation 1.8)}$$

which is true only if the material's intrinsic $\chi^{(2)}$ along some i, j, and k crystalline orientation is equal to 0, since $\boldsymbol{P}^{(2)}$ and $\boldsymbol{E}$ are finite and ϵ_o is a constant. Therefore, the crystal structure of a material must be non-centrosymmetric to observe second-order nonlinear effects. Conventional nonlinear crystals exhibit a $\chi^{(2)}$ up to ca. 400 pm V^{-1}, but typically less than 10 pm V^{-1}.[33] It is noted however, that a finite nonlinear signal originates from surface contributions in all materials, regardless of crystal structure, where centrosymmetry is broken at interfaces and lattice defects.[39]

1.5 Research Objective

This work examined conversion of infrared energy from two-dimensional transition metal dichalcogenides (TMD)[42–44] within plasmonic fields of nanoantennas[12,45,46] via two mechanisms: (i) plasmonic hot electron transport and (ii) enhanced second harmonic generation (SHG). Monolayer TMD were renowned for their extraordinary SHG activity[47] arising from their reported $\chi^{(2)}$ up to 10^4 pm V^{-1}.[48–54] Nanoantennas augment local electric field 10-100x by confining incident energy into surface plasmons,[12,55] and thus offered higher power densities for nonlinear phenomena from TMD. Plasmonic hot electron interactions had been inferred in nanoantenna-TMD heterostructure devices,[56–58] but remained to be quantified. Overall, little was known about the electromagnetic interplay between TMD and nanoantennas. Rapid experimental progress since initial work in 2013 had outpaced development of descriptive frameworks by which to interpret experimental results. This work provided new insights into the resonant energetics and damping between coupled plasmonic and excitonic materials across the linear and nonlinear optical regimes.

CHAPTER 2

SURFACE PLASMON PHOTONICS

Electromagnetic energy may be concentrated to sub-wavelength scales at augmented field intensities by nanoantennas in the form of coherent electron oscillations, called localized surface plasmons.[12,15] Nanoantennas are nanoscale architectures whose morphology and arrangement are engineered to manipulate light,[59,60] sometimes in ways that defy materials found in nature.[61,62] This chapter surveys the electrodynamical framework, materials, and architectural parameters which guided nanoantenna design for infrared energy conversion processes.

2.1 Surface Plasmon Excitation

Subwavelength structures, called nanoantennas, allow manipulation of electromagnetic energy through their ability to support plasmons.[46] Plasmons are quasi-particles of electromagnetically-induced coherent oscillations of electron gas in condensed matter. The structural morphology, elemental composition, physical arrangement, and environment of nanoantennas determines their absorption and scattering of electromagnetic energy.

2.1.1 Localized Surface Plasmon Resonance

Coherent electron gas oscillations confined to the surface of a nanoantenna are referred to as localized surface plasmons (LSP).[15,63] The energy, or frequency, at which a LSP is induced on a given nanoantenna is referred to as the localized surface plasmon resonance (LSPR). Figure 2.1 schematically depicts dipole LSPR excitation on a subwavelength sphere, explored initially by Gustav Mie in the early 20th century.[64] Expanding the radial dimension of the sphere accommodates excitation of multi-pole LSPR, such as a quadrupole, hexapole, etc. due to phase retardation across the sphere.[65] The LSPR is intrinsically a function of size,[66,67] shape,[63,66,68,69] and elemental composition[70–72] of a nanoantenna. The LSPR is extrinsically dependent on dielectric screening in media local to the nanoantenna.[59,73–75]

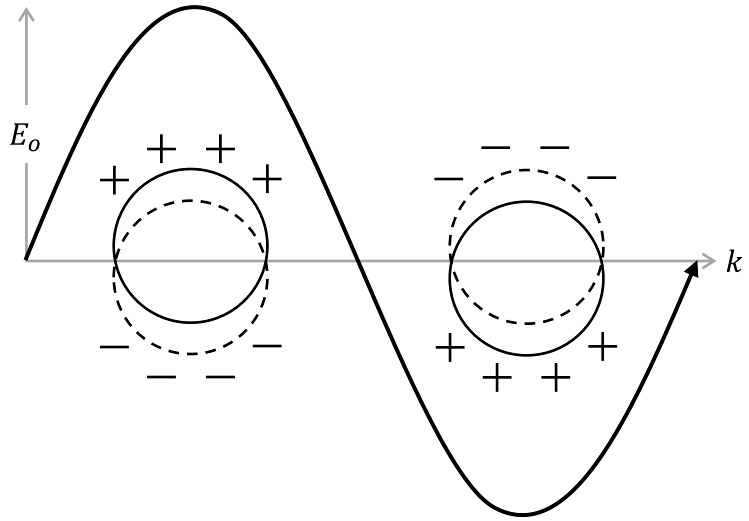

Figure 2.1: Electromagnetic wave propagating in free space inducing a dipolar localized surface plasmon on a subwavelength sphere. E_o is the electric field amplitude and k is the wave vector.

2.1.2 Fano Resonant Diffractive Coupling

Periodically arranging nanoantennas into regular lattices at constants near or above their LSPR wavelength results in Fano resonant coupling between LSP and diffractive modes, causing emergence of a coupled lattice resonance (CLR).[76–78] In-phase diffractive scattering induces coherent plasmonic oscillation across the lattice with enhanced net electric field strength, provided that the diffraction length falls within the intrinsic polarizability envelope of the nanoantennas.[79] Figure 2.2 schematically depicts CLR excitation for (a) rectilinear and (b) hexagonal lattice arrangements of nanoantennas. Rectilinear lattices consist of nodes at regular intervals in cardinal directions (d_y and d_x, respectively). Square lattices (i.e., $d_y = d_x$) are a subset of rectilinearity that exhibit an isotropic response to $\hat{x}$ and $\hat{y}$ polarization due to $\pi/2$ rotational symmetry.[80] Hexagonal lattices exhibiting $\pi/6$ rotational symmetry with an anisotropic polarization response.

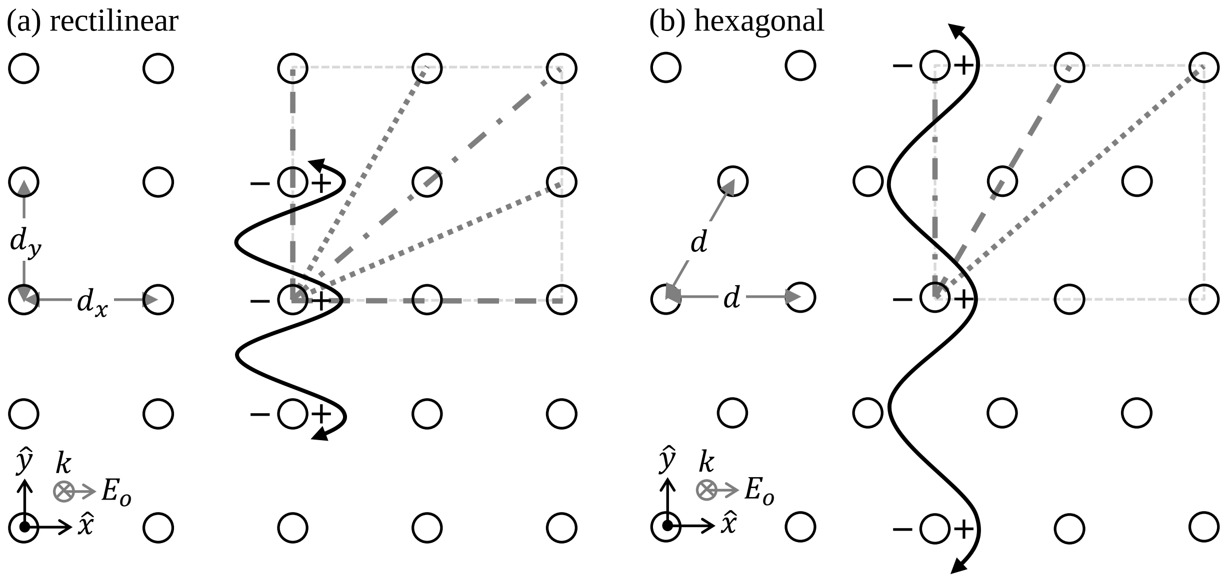

Figure 2.2: Schematic representations of CLR excitation in (a) rectilinear and (b) hexagonal lattices of nanoantennas. Grid in upper right quadrant of each lattice type coordinates inter-node diffraction at the lattice constant (dashed), primary diagonal (dot-dashed), and off-axis positions (dotted) relative to the center node.

Two primary plasmon resonant modes are supported by diffractive-coupling nanoantenna lattices: (i) the dipolar surface plasmon and (ii) the CLR. The higher energy dipolar surface plasmon originates from the LSP, but is blue-shifted by tens of nanometers[81] via destructive Fano interference spanning between the inherent LSPR and lattice constant lengths. Diffractive coupling is intrinsically a function of the lattice constant and incident polarization[65,80] and extrinsically a function of environment local to the lattice.[65,75,81,82] Fano resonances based upon near-field interactions between surface plasmons on adjacent, nearby nanoantennas[77,78,83–86] were not considered in this work.

2.2 Computational Models

Optics of nanoantenna systems may be modeled by finite difference time domain (FDTD),[87] boundary/finite element methods (BEM/FEM), T-matrix,[88] and coupled/discrete dipole approximations (CDA/DDA) to Maxwell's equations.[74,89,90] Discretization of time and space in FDTD, FEM, and T-matrix offer precise numerical solutions to Maxwell's equations at significant computational expense. Computational memory advantages of BEM are limited to nanoantennas whose volume may be approximated as a one-dimensional (1D) surface contour,[91] e.g., nanodiscs. DDA and CDA together offer reduced computational time,[92,93] elegant consideration of inhomogenous local environments,[82] and the unique flexibility to describe fabricated nanoantennas with distorted, complex morphologies.[94] This section describes utilization of CDA and DDA to guide design and describe optical behavior of nanoantennas.

2.2.1 Coupled Dipole Approximation

The CDA solves Maxwell's equations for two-dimensional (2D) nanoantenna lattices by treating each constituent nanoantenna as a point dipole with polarizability, α, characteristic of its size, morphology, and elemental composition.[74,95,96] Dipole polarization induced on each nanoantenna, $\boldsymbol{p}$, in response to an applied electric excitation field, $\boldsymbol{E}_o$, is calculated according to its α, *viz.*

$$\boldsymbol{p} = \frac{\alpha \boldsymbol{E}_o}{1 - \alpha S} \qquad \text{(Equation 2.1)}$$

where S represents the retarded dipole sum, which accounts for near-field and far-field dipole radiation from adjacent nanoantennas comprising the lattice.[74] At lattice constants comparable to the excitation wavelength, accrued far-field diffraction between lattice nodes dominate S. Optical extinction of an orthogonally incident wavevector, k, arises from the degree to which polarization of the lattice is out of phase with the incident field (i.e., $\boldsymbol{p}/\boldsymbol{E}_o$). Resultant extinction may be expressed by

$$\sigma_{ext} = 4\pi k \, \Im\left(\frac{1}{1/\alpha - S}\right) . \qquad \text{(Equation 2.2)}$$

The CDA is limited to situations for which analytical descriptions of S for a given lattice and nanoantenna α exist. The rapid, semi-analytical solution for the CDA (rsa-CDA) exploits rotational symmetry of square lattices to ease computation of S.[79,95] Analytical dipole α is available for centrosymmetric nanoantennas such as spheres, spheroids, and toroids in homogeneous environments.[79,97,98] Corrections to sphere α to account for quadrupole interactions[79] and/or immersion in lossy, multi-layered environments[99] may be implemented. However, external calculation of α is required for situations involving (i) arbitrary nanoantenna morphologies or (ii) complex dielectric super/sub-strates.

2.2.2 Discrete Dipole Approximation

The DDA solves Maxwell's equations for absorption and scattering of electromagnetic waves by arbitrary, three-dimensional ensembles of polarizable dipoles according to their elemental composition(s) and unique arrangement.[89,100] A subwavelength target, e.g., a non-symmetric nanoantenna on a substrate, is discretized into a cubic lattice of dipoles with characteristic dielectric functions; α for each dipole comprising the target is calculated according to a Lattice Dispersion Relation.[101] Extinction and absorption cross sections of the ensemble are readily deduced from polarization magnitudes at each i^{th} sub-volume of the target, $\boldsymbol{P}_i$, in response to its local electric field, *viz*.

$$\boldsymbol{P}_i = \alpha_i \left(\boldsymbol{E}_{o,i} - \sum_{j \neq i}^{N} \boldsymbol{A}_{ij} \boldsymbol{P}_j \right) \qquad \text{(Equation 2.3)}$$

where $\sum_{j \neq i}^{N} \boldsymbol{A}_{ij} \boldsymbol{P}_j$ accounts for interactions between dipoles. Here $\boldsymbol{A}_{ij}$ is the dipole-dipole interaction matrix including radiative retardation; it is a three-dimensional, more rigorous analog to S in the CDA. Extinction and absorption cross sections are then computed according to Equations 2.4-2.6 after solving for all $\boldsymbol{P}_i$ in the target.

$$\sigma_{ext} = \frac{4\pi k}{|\boldsymbol{E}_o|^2} \sum_{j=1}^{N} \Im\left(\boldsymbol{E}_{o,j}^{*} \cdot \boldsymbol{P}_j \right) \qquad \text{(Equation 2.4)}$$

$$\sigma_{abs} = \frac{4\pi k}{|\boldsymbol{E}_o|^2} \sum_{j=1}^{N} \left\{ \Im\left[\boldsymbol{P}_j \cdot \left(\alpha_j{}^{-1}\right)^* \boldsymbol{P}_j^*\right] - \frac{2}{3} k^3 \left|\boldsymbol{P}_j\right|^2 \right\} \qquad \text{(Equation 2.5)}$$

$$\sigma_{sca} = \sigma_{ext} - \sigma_{abs} \qquad \text{(Equation 2.6)}$$

Near- and far-field optical responses of arbitrarily shaped nanoantennas interfaced with complex dielectric sub- and/or super-strates, called a target, are described uniquely by the DDA. An example DDA target is shown in Figure 2.3. Electric field-enhancement factors for the target are calculated according to the Clausius-Mossotti relation.[102] Far-field optics of 1D chains and 2D rectilinear lattices of targets are calculated by a generalization of the Mueller scattering matrix.[103] Detailed electromagnetic data comes at the expense of requiring 10^3-10^6 dipoles for computational convergence, thus necessitating DDA simulations execution on high-memory, multi-core processing clusters.

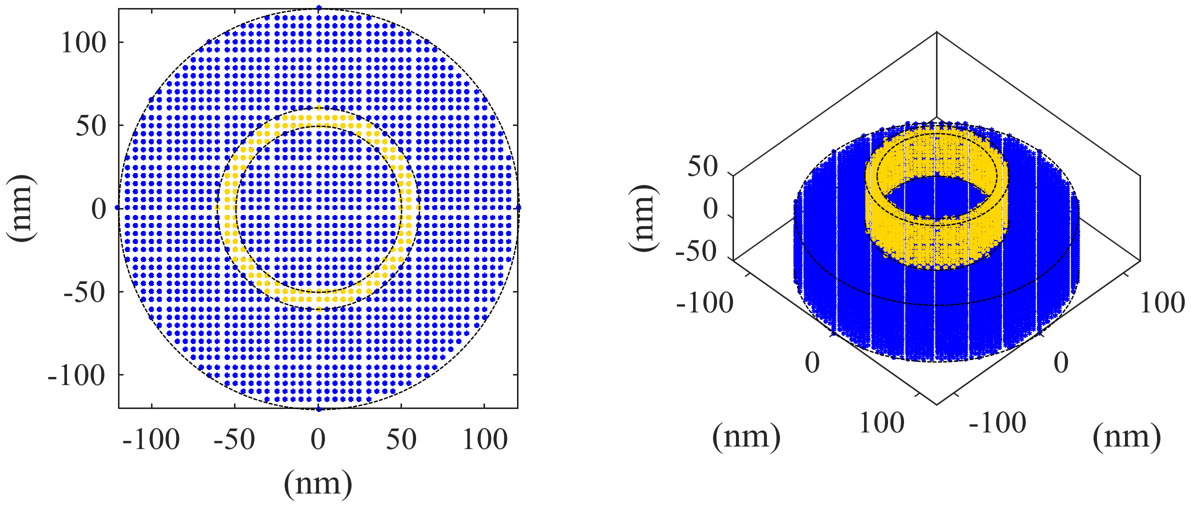

Figure 2.3: Example DDA target comprised of a nanoring supported by a cylindrical substrate discretized into 21,219 dipoles according to a 5 nm inter-dipole spacing. Nanoring dimensions are 60 nm outer radius, 10 nm wall thickness, and 50 nm height. Substrate dimensions are 120 nm radius and 50 nm height. Point dipoles comprising the target are illustrated as spheres; yellow and blue represent the nanoring and substrate, respectively.

The DDA is available as open-source software from Draine and Flatau as DDSCAT.[100–103] Recent implementations by Masiello and Henrard adapt the DDA algorithm to electron-excitation, called eDDA[104] and DDEELS,[105] respectively. Nanoantenna excitation by an electron uniquely induces resonances not observable under light excitation, deemed "dark" modes. Comprehensive characterization of both bright and dark modes comprising the overall plasmonic mode structure is unique to electron excitation.

2.2.3 Multi-Scale Synthesis of Discrete & Coupled Dipole Approximations

The DDA and CDA was synthesized to rapidly describe far-field optical extinction from lattices composed of arbitrary nanoantenna-dielectric nodes, where DDA calculated an effective α in the absence of analytical descriptions.[92] Effective α of DDA targets were calculated via

$$\alpha_{eff} = \sum_j \frac{d^3 \boldsymbol{P}_j}{\boldsymbol{E}_{o,j}} \qquad \text{(Equation 2.7)}$$

where d is the inter-dipole spacing of the discretized target. Synthesized DDA-CDA allowed rapid (i) optimization of lattice constant for optimal CLR activity at 40,000x reduced computation time[75,92] and (ii) interrogation of near-field dielectric screening and energy exchange impacts on coupled nanoantenna interactions in complex dielectric environments.[82]

Utility of the multi-scale DDA/CDA approach was benchmarked against experimental transmission UV-vis spectra from a 2D square lattice of 160 nm gold (Au) nanospheres lithographed onto indium tin oxide (ITO) covered silica (SiO_x),[82] which exhibited resonance features unexplainable by the CDA.[81] A scanning electron microscopy (SEM) image of the sample is shown in Figure 2.4(a). The DDA was first used to examine SiO_x- and ITO-dependent dynamics of plasmon excitation and accrued damping for a single 160 nm Au nanosphere embedded 0%, 15%, and 30% by surface area into the substrate.[106] Red-shifts in LSPR scaled with substrate interaction (i.e., embedment). Atomic polarization within the substrate increasingly suppressed the Coulombic restoring force acting against the plasmon oscillation, thus decreasing net energy required for plasmon excitation.[65] Enhanced electric near-field plots in Figure 2.4(b) show plasmonic energy transfer and surface plasmon dipole pattern alterations unique to both SiO_x and ITO.[82] Overall, SiO_x accrued additional radiative scattering losses while ITO improved non-radiative absorption and energy confinement.

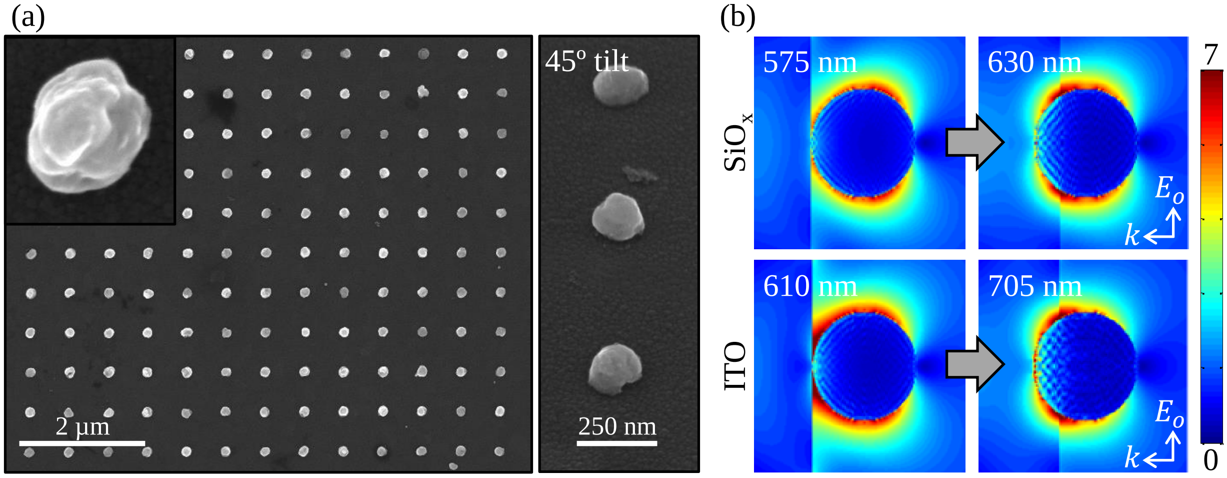

Figure 2.4: (a) SEM micrographs of a 2D square lattice of 160 nm Au nanospheres lithographed onto ITO-covered SiO_x. (b) Electric near-field enhancement (E/E_o) at the LSPR for Au nanospheres embedded 0% (left column) and 30% (right column) by surface area into SiO_x (top row) and ITO (bottom row). Wavelengths of LSPR for each are inset.

Extraction of DDA-calculated α_{eff} for a 160 nm Au nanosphere interacting with SiO_x or ITO into the rsa-CDA showed ITO primarily red-shifted near-field LSPR and glass primarily affected far-field diffractive interactions.[82] Figure 2.5 shows experimental transmission UV-vis extinction spectra (black) reproduced by superposed theoretical spectral signatures of distinct nanosphere-substrate interaction scenarios (15% dashed; 30% dotted) with SiO_x (blue and cyan) or ITO (red and orange). Symbols label the origin of each spectral feature. Spectral features at 490 nm, 532 nm (dipole surface plasmon of the lattice), and 670 nm (a CLR) were anticipated by the CDA with analytical sphere α and Maxwell Garnett (MG) effective medium theory[107,108] (black symbols).[81] Expanded bandwidth of the 670 nm feature, presence of secondary shoulders, and near-infrared resonances 750-800 nm could not be explained using analytical α with MG in the CDA. The multi-scale approach employed herein rapidly characterized *a priori* the bandwidth, relative intensity, and wavelength occurrence for each of these previously unknown resonances.

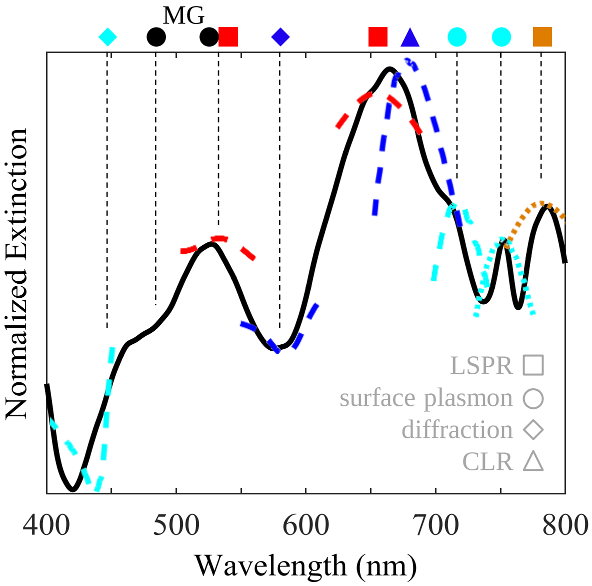

Figure 2.5: Experimental transmission UV-vis extinction spectra (solid black) with superposed theoretical optical extinction signatures (dashed and dotted colored) from single and ordered 160 nm Au nanospheres interacting with SiO_x (blue and cyan) or ITO (red and orange).

2.3 Material Considerations

Utilization of a metal, semiconductor, or ceramic as a plasmonic nanoantenna has direct impacts on its capabilities to resonantly confine, transport, or transduce electromagnetic energy. Research in light-matter interactions has focused on noble metals since Michael Faraday's discovery of stable Au colloids in the mid-19th century.[109] Despite historical significance of metals, research into plasmonically-active semiconductors and ceramics recently accelerated because of their (i) activity near the 1.55 µm telecommunication frequency, (ii) compatibility with CMOS technology, and (iii) lower intrinsic losses.[70–72] Design of nanoantennas for operating within large temperature gradients requires careful survey of a material's intrinsic plasma frequency range and losses, as well as its ability to structurally withstand high temperatures.

Table 2.1 summarizes the intrinsic plasmonic activity of different metal, ceramic, and semiconductive materials according to their underlying Drude-Lorentz dielectric function parameters and respective melting points. Drude-Lorentz dielectric theory expresses $|\boldsymbol{P}|$ of a material by its intrinsic electric permittivity function, $\epsilon(\omega)$, according to inter- and intra-band optical interactions/losses, *viz.*[110]

$$\epsilon(\omega) = \epsilon'^{(\omega)} + i\epsilon''(\omega) = \varepsilon_b + \sum_j \frac{f_j {\omega_{p,j}}^2}{{\omega_j}^2 - \omega^2 - i\omega\gamma_j} \qquad \text{(Equation 2.8)}$$

where ϵ_b signifies core-electron polarization, $f_j\omega_{p,j}$ is the free-electron intraband plasma frequency strength, ω_j is some resonant interband transition, and γ_j is the total damping rate from electron scattering by electrons, phonons, and lattice defects (e.g., grain boundaries). The real component, $\Re(\epsilon)$, signifies polarization strength. The imaginary component, $\Im(\epsilon)$, signifies losses. Equation 2.9 gives the bulk ω_p from j^{th} resonance-induced carrier concentration (N), electron charge (e), permittivity of free space (ϵ_o), and effective electron mass (m_o).

$${\omega_p}^2 = \frac{Ne^2}{\epsilon_o m_o} \qquad \text{(Equation 2.9)}$$

LSPR for quasistatic nanoantennas is directly related to the bulk ω_p, but occurs at lower energies due to surface damping (increasing γ in Equation 2.8) and screening by the local environment.[111]

Metals exhibit ω_p between 8.7 eV to 12.7 eV, leading to LSPR in the UV to visible spectrum.[70,71,112–114] Melting points range from 660 ˚C to 1085 ˚C.[115] High losses at the plasmon frequency from interband transitions [$\Im(\epsilon) \sim 10^0$-10^1] and at 1.55 µm from intraband transitions make them undesirable for many applications, especially electrical-optical transition circuitry components.[116] Notwithstanding relatively low melting points ranging from 660 ˚C to 1085 ˚C precluding use in high temperature applications,[115] aluminum (Al), silver (Ag), and copper (Cu) also suffer from oxidation in natural environments which raise additional degradation concerns.[70,117,118] Relatively high ϵ_b of metals make them the strongest resonators in Table 1 (data not shown). However, complex nanoantenna morphologies[75,86,119–121] and Fano coupling interactions[92,122–124] are required to shift LSPR activity into the infrared spectrum, which involves high capital lithography processes with generally low throughout.[125–127]

Table 2.1: Comparison of common plasmonic materials and their experimentally measured optical characteristics according to Drude-Lorentz dielectric theory.

material		**resonant spectrum**	$\boldsymbol{\omega_p}$ **[eV]**	$\mathfrak{I}(\boldsymbol{\varepsilon})$ **at** $\boldsymbol{\omega_p}$	$\mathfrak{I}(\boldsymbol{\varepsilon})$ **at 1.55 µm**	$\boldsymbol{\gamma_p}$ **[eV]**	**melting point [˚C]**
metals [70,71,112-118]	Al	UV-visible	12.7	10^0	46	0.13	660
	Ag	visible	9.2	10^1	3-4	0.02	962
	Au	visible	8.9	10^1	11	0.07	1064
	Cu	visible	8.7	-	15	0.07	1085
ceramics† [70,-72,112,116,128-130]	TiN	visible-NIR	1.92-2.43	3.1-8.2	20	0.18-0.51	2930
	ZrN	visible-NIR	-	2	8-55	0.52	2980
	Al:ZnO‡	NIR	0.71-2.03	0.8-1.6	0.1-1.3	0.04-0.31	660-1975*
	Ga:ZnO	NIR	1.99	10^{-1}	0.59-1.2	0.12-0.22	30-1975*
	ITO	mid-IR	0.62-1.07	0.5-1.4	0.2-1.5	0.16	1526-1926
	NiSi	mid-IR	4.6-7.4	-	12	10^{-1}	993
	TiSi	mid-IR	4.2	-	10	10^{-1}	1470
semicond. [71,130,131]	InAs	mid-IR	0.12-0.22	0.4-0.6	-	10^{-1}	942
	InSb	mid-IR	0.18	2.7	-	10^{-1}	527
	ZnO	long-IR	0.30	1-3	-	-	1975

† passively tunable according to deposition temperature/environment and dopant concentration
‡ demonstrated active tunability according to electrical bias
* cited range of known melting points for subcompounds comprising the alloy

Ceramic and semiconductive materials offer (i) intrinsic LSPR throughout the infrared spectrum at lower loss,[70,71] (ii) generally higher melting points than metals,[115] and (iii) compatibility with CMOS fabrication technology.[71,72] The ϵ of ceramics is passively tunable, unlike metals, according to their deposition temperature and environment (e.g., nitrogen versus argon gases) and dopant concentration.[112,128] Transparent conducting oxides [aluminum/gallium-doped zinc oxide (Al:ZnO/Ga:ZnO) and ITO][70,112,116,128–130] and transition metal nitrides [titanium/zirconium nitride (TiN/ZrN)][72,116,128] exhibit ω_p between 0.62 eV and 2.43 eV leading to near- to mid-infrared LSPR. Active ϵ tunability has been demonstrated for Al:ZnO and ITO with electric bias.[116] High temperature applications may be best suited for TiN and ZrN, whose melting points exceeding 2900 ˚C ensure structurally robust nanoantennas. Silicides [nickel/titanium silicide (NiSi/TiSi)] exhibit many metal-like Drude-Lorentz characteristics, but with LSPR in the mid-infrared due to high damping rates.[71] Semiconductive III-V indium arsenide/antimonide (InAS/InSb)[71] and II-VI zinc oxide (ZnO)[71,130,131] support LSPR in the mid- to long-infrared spectrum, but their understanding as a plasmonic material remains immature.

Overall, Al:ZnO or ITO appeared as ideal candidates for surface plasmon-functionalized energy conversion of infrared radiation in optoelectronics. Both materials exhibit low loss at the plasmon and telecommunication frequencies (ca. 1526 ˚C to 1975 ˚C melting points for resistance to high temperature deformation)[115] and comparable ϵ_b to metals for intense, broad-band field enhancements.[70] Compatibility with conventional CMOS processing supports facile integration into current electronic platforms.[116] Active and passive LSPR tunability offers on-board tailoring of optical activity to unique thermal environments.[116] However, Al:ZnO and ITO plasmonics have remained in the prototyping phase primarily due to lack of: (i) widely disseminated, reproducible data for plasmonic interactions, (ii) availability of infrared-compatible spectroscopic tools to validate models, and (iii) refined chemical synthesis techniques relative to noble metals. Therefore noble metal, in particular Au, nanoantennas were used herein as prototypes to explore the underlying hypothesis of this dissertation.

2.4 Morphology Influences

Morphological acircularity and annularity influences on the evolution of the electromagnetic local density of states (ELDOS) for plasmonic nanoantennas were characterized using computational electron energy loss spectroscopy (EELS; detailed later in § 5.1) to guide nanoantenna design.[94] Available plasmonic states of a nanoantenna may be tailored to application-specific energies by engineering its morphology.[66,75,97,132,133] Concomitantly, LSPR can deviate from design as a consequence of structural aberrations accrued from self-assembly and/or oxidization in natural environments.[118,132] To date, plasmonic mode structures have been computed for nanodiscs,[134] nanoellipses,[135] nanobipyramids,[136] triangular nanoprisms,[137–139] nanorods,[140] split-ring resonators,[141] and dynamic disc transformations into triangular prisms.[142] Plasmonic mode structures obtained in EELS[143] only qualitatively describe the ELDOS however.[144] Direct quantitative correlation is precluded by differences in respective electric-field distributions of a photon versus a propagating electron.[135,145]

Figure 2.6 shows the evolution of plasmon mode structure within the ELDOS of a 60 nm radius Au nanodisc (upper left) as a result of 1.5x aspect radial elongation and annulation.[94] Au was used because its quasistatic LSPR in the visible spectrum readily allowed facile observation of morphological changes to plasmonic activity across a wide energy range. EELS spectra were computed with eDDA (v2.0).[146] Impact points of the electron beam were the center (blue), half major/minor radius (purple/cyan), and full major/minor radius (red/green).

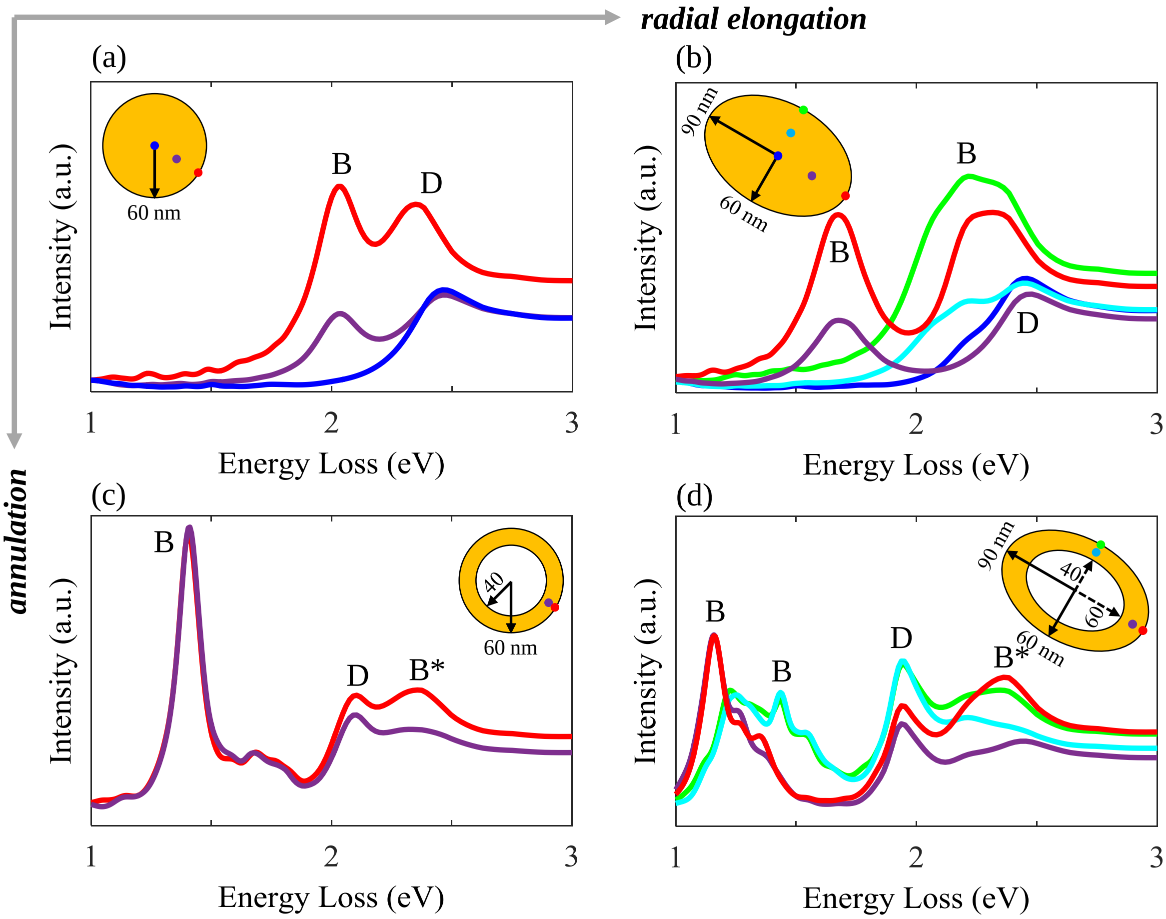

Figure 2.6: Computational EELS spectra for a 60 nm radius (a) Au nanodisc subjected to (b) 1.5x aspect ratio elongation, (c) annulation, and (d) 1.5x aspect ratio elongated annulation. Electron beam impact points were at the nanoantenna center (blue), major axis edge/mid-point (red/purple), and minor axis edge/mid-point (green/cyan). Structure schemes for each nanoantenna are inset. Height was held constant at 20 nm. "B" and "B*" indicate bonding and anti-bonding bright plasmon modes. "D" indicates dark plasmon mode.

Each impact point induced a spatially-unique bright or dark plasmon resonance mode in the ELDOS. Bright plasmon modes (labeled B and B* for bonding and anti-bonding, respectively) are resonances which exhibit a finite net dipole moment ($\sum \vec{p} \neq 0$), thus enabling both photon and electron induction. Electron beams are also capable of exciting dark plasmon modes (labeled D) with net zero dipole moment ($\sum \vec{p} = 0$) which cannot be directly induced by photons. Thus, resonances not observed in light-excitation DDSCAT (v7.3)[100] simulations were classified as dark modes.[147] In the quasistatic limit for Au, the bright and dark modes converge at 2.45 eV where the real component of its dielectric function crosses zero, i.e., the bulk ω_p.[148] The two modes split and shift upon radial elongation (upper right), annulation (lower left), and concomitant elongation and annulation (lower right) due to phase retardation and inter-surface capacitive coupling.

Centrosymmetric nanoantennas just beyond the quasistatic regime yielded distinct bright and dark plasmon resonances.[94] Figure 2.6(a) shows bright and dark plasmon resonances at 2.03 eV and 2.45 eV for a 60 nm radius nanodisc. The 2.03 eV bright mode corresponded to a dipole LSP, as previously reported for optical excitation.[149] Expansion of the radial dimension would (i) red-shift the dipole LSP and (ii) accommodate multipole LSP resonances in the ELDOS. Angular rotational symmetry of the nanodisc precluded resonant energy dependence on the angular coordinate. The dark mode at 2.45 eV represents the bulk plasma energy of Au.[150] The bulk mode for Au has been observed for other structures.[150–152] Though not inducible by photons, an optically excited bright dipole LSP can decay into a dark mode via coupled excitation of an adjacent structure.[77,86] Corresponding EELS supporting mode-type classifications in Figure 2.6(a) can be found in Refs. 94, 153, and 151.

Radial elongation of the nanodisc to a 1.5x aspect ratio, in Figure 2.6(b), caused a second, lower energy bright mode to emerge due to radial asymmetry.[94] Nanorods analogously support two bright modes in their ELDOS, observed in polarized optical excitation along transverse (rod diameter) and longitudinal (rod length) axes.[154] Major axis excitation induced a 1.67 eV bright LSP. Minor axis excitation induced a 2.21 eV bright LSP, blue-shifted by 0.17 eV from the initial centrosymmetric disc bright mode. Dipole LSP are known to red-shift from increasing the radial dimension of an axis because of phase retardation, per Mie theory of oblate spheroids.[64] The 2.45 eV dark “bulk” mode was preserved despite structural asymmetry. Optical excitation of an ellipse can controllably decay into a dark mode on an adjacent ellipse by tuning physical orientation between the two.[155] Corresponding EELS maps supporting mode-type attribution may be found in Refs. 151 and 152.

Distinct dipole "bonding" and "anti-bonding" bright plasmon resonances arose from annulation of the nanodisc,[94] caused by capacitive charge interactions between the inner and outer ring walls.[92,119] Resonances at 1.41 eV, 2.11 eV, and 2.36 eV in Figure 2.6(c) corresponded to bright bonding, dark, and bright anti-bonding plasmon modes,[156] respectively. Corresponding EELS maps corroborating mode-type attribution may be found in Ref. 94. The bright resonances agreed within 0.17 eV to 0.03 eV of experimental and theoretical reports of comparably sized rings.[75,92,119] High energy anti-bonding exhibits dipole moments on each wall, anticipated to occur near 2.4 eV according to a Drude-type dielectric model.[119] Anti-bonding modes were not observed in EELS experiments on smaller nanorings.[157] Low energy bonding exhibits collective negative and positive charge on opposing walls, and was anticipated to occur near 1.2 eV according to a Drude-type dielectric model.[119] Charge distributions for each bright mode type are illustrated in Ref. 119. Increasing the ring aspect ratio (wall thickness to radius) converges the bonding resonance to that of a disc LSPR,[119] as described earlier. The 2.11 eV dark resonance would create net zero dipole moments ($\sum \vec{p} = 0$) within the ring wall.[94] Such a charge distribution would not be possible under optical excitation because each subwavelength ring wall experiences a static electric field.[145] Dark modes were not observed in EELS experiment of rings with 7-10 nm wall thicknesses.[157]

Simultaneous elongation and annulation hybridized the nanoantennas' ELDOS between that of a nanoring and a nanoellipse.[94] Figure 2.6(d) shows 1.16 eV bright minor axis bonding, 1.44 eV bright major axis bonding, 1.94 eV dark plasmon, and 2.42 eV bright anti-bonding resonances. Occurrence of bonding along each axis, emergence of anti-bonding behavior, and a preservation of a single dark mode are consistent with hybridization of the ring and ellipse plasmonic mode structures. For example, consider the 1.5x aspect ratio nanoellipse in Fig. 1(b) subjected to annulation. Annulation at the considered structure dimensions (i) red-shifted the bright mode by 0.62 eV, (ii) red-shifted the dark mode, and (iii) caused a bright anti-bonding mode to emerge at 2.36 eV. Annulating the nanoellipse [transition from (b) to (d) in Figure 2.6] indeed caused both bonding modes to red-shift, red-shifted to dark mode down to 1.94 eV, and induced a bright anti-bonding mode at 2.42 eV. Bright bonding mode energy for the 0.6x aspect ratio major axis was lower than that of the 0.7x aspect ratio minor axis, consistent with previous optical reports.[75,92] A parallel analysis could have been performed by elongating the nanoring to a 1.5x aspect ratio to arrive at the same result.

2.5 Summary

Material and structural morphology influences on discrete localized (e.g., LSPR) and coupled (e.g., CLR) surface plasmon resonance modes comprising the ELDOS of nanoantennas were elucidated, enabling their design towards nonlinear infrared frequency conversion processes. Electrodynamic frameworks of the CDA and DDA to describe plasmonic phenomena were described. A survey of Drude-Lorentz theory parameters and melting points across metals, ceramics, and semiconductors indicated Al:ZnO and ITO were well-suited as nanoantenna materials for the proposed hypothesis. However, an immature understanding of their plasmonic properties and available spectroscopic tools limit their implementation over traditional noble metals, such as Au. Excitation by a swift electron in the DDA distinguished emergence and energy-shifting patterns for bright and dark plasmonic modes of a Au nanodisc subjected to elongation and/or annulation. Radial elongation caused a second bright plasmon resonance to emerge at a lower energy. Annulation split the initial bright mode into discrete higher-energy anti-bonding and lower-energy bonding bright modes. Elliptical annulation hybridized the effects. Overall, the foundational electrodynamic and material frameworks to optimize nanoantennas for infrared functionality were described.

CHAPTER 3

TWO-DIMENSIONAL TRANSITION METAL DICHALCOGENIDES

Monolayer group-VI transition metal dichalcogenides (TMD) exhibit remarkable light-matter interactions arising from their direct bandgap,[42] presence of van Hove singularities,[158] and lack of crystalline inversion symmetry.[50] A TMD crystal is comprised of a single transition metal and two chalcogen atoms. Van der Waals bonding between monolayers comprise bulk TMD, which have been studied extensively since the 1960s.[159–161] The discovery of graphene in 2004[162] renewed interest in TMD materials to exploit the optical, electronic, and physical properties unique to monolayers, most notably, in photocatalysis[163] and field-effect transistors.[164] Monolayer TMD exhibit extraordinary optoelectronic and nonlinear optical activity,[50] and thus were chosen as the base material for prototyping energy conversion within plasmonic fields.

3.1 Overview

Group-VI TMD crystals are van der Waals bonded semiconductive monolayers of the formula MX_2, comprised of a transition metal (M; molybdenum or tungsten) occupying trigonal prismatic sites between two hexagonal chalcogen layers (X; sulfur, selenium, or tellurium).[43] Figure 3.1 shows the crystal structure of a single-layer TMD. Different structural polytypes occur based on trigonal or octahedral coordination of the transition metal with the chalcogens: 2H, 3R, or 1T.[165,166] TMD naturally form the 2H phase, but may be reversibly changed to the "metallic" 1T phase[167] by external optical/electrical stimuli[56] or elemental doping.[168] TMD are not limited to semiconductive behavior; TMD based on group-V transition metals (e.g., niobium or tantalum) range from metallic to superconductive.[165] Scope of this work was limited to group-VI TMD monolayers, specifically molybdenum and tungsten disulfide (MoS_2 and WS_2, respectively).

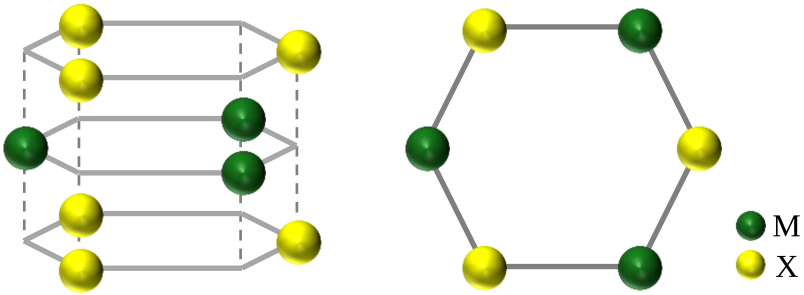

Figure 3.1: Crystal structure of a TMD monolayer with the transition metal atoms (M) in green and chalcogen atoms (X) in yellow.

The optical properties of TMD change with layer number comprising the total thickness.[42,169] Bulk TMD are indirect-bandgap semiconductors. In the monolayer limit however, quantum confinement alters their electronic band structure to accommodate direct transitions across the K point of the Brillouin zone near 2 eV range and suppresses the bulk-form indirect transition.[42] The linear optical properties of various TMD are tabulated in Refs. 43 and 44. The fundamental direct bandgap is referred to as the A bandgap and higher-energy direct transitions are referred to as the B, C, etc. bandgaps by convention. The A and B transitions both occur across the K point but are distinct in energy because of spin-split valence bands, accrued from spin-orbital coupling.[43] Such interactions enable TMD to be used in spintronics,[170] where the spin state could serve as a degree of freedom for storing data.[171] Electrical properties of TMD, e.g., 10^8 on/off ratio[172] and 1000 cm^2 V^{-1} s^{-1} carrier mobility[173] demonstrated in monolayer MoS_2 field-effect transistors, are reviewed in Refs. 44 and 165.

3.2 Fabrication Techniques

Two-dimensional (2D) monolayer TMD may be fabricated naturally or synthetically by exfoliation from bulk crystals or chemical vapor deposition (CVD) growth, respectively. Weak inter-layer van der Waals forces and strong intra-layer covalent bonds facilitate access to single TMD monolayers from natural bulk crystals from a strategically applied force, called exfoliation. Scaling monolayer TMD crystals to wafer-scale lengths has motivated refinement of synthetic protocols based on gaseous chalcogens reacting with oxidized transition metals at high temperature and vacuum to form monolayers on specific substrates. The MoS_2 and WS_2 samples used herein were fabricated by (i) liquid exfoliation into water or ethanol and (ii) CVD onto silica (SiO_x) atop a silicon (Si) wafer.

Exfoliation of TMD by mechanical,[42,164] chemical,[168,174] and liquid[175–177] techniques have been described. Mechanical exfoliation of single-crystalline TMD at 1-10 µm length scales using adhesive tape is suitable for fundamental studies and prototyping, but suffers from low throughput and no control over thickness.[44,178] Chemical exfoliation produces gram quantities of sub-1 µm TMD monolayers by overcoming van der Waals force between layers with the hydrogen evolution reaction, where water interacts with lithium ions intercalated between TMD layers (via *n*-butyllithium).[168,174,179] However, the process induces a phase change to the metallic 1T phase and a 300 ˚C annealing step[168] is required to restore the semiconducting 2H phase desired for optoelectronic applications. Liquid exfoliation techniques span many protocols which bypass chemical oxidation of the bulk materials in favor of some direct strategy,[175–177] most namely the utilization of an ultrasonic probe to shear monolayers from the bulk crystal into a solvent.[180,181]

Synthetic CVD growth involves strategic placement of chalcogen and transition metal oxide precursors in a pressure- and temperature-controlled tube furnace. The chalcogen powder precursor is vaporized and then reduced with the transition metal onto a substrate.[182–185] CVD processes form triangular TMD monolayers due to their trigonal crystal structure. Typical sizes range from 1-100 µm length scales depending on purities of precursors, substrate, and environment.[185–187] However, recent precursor refinements have advanced the technique to give polycrystalline monolayer films across centimeter scales[188] and even 100 mm wafers.[189]

3.2.1 Liquid Phase Exfoliation

Liquid phase exfoliation presents a readily accessible, potentially scalable method for technologies based on few- to mono-layer TMD.[175–177] Figure 3.2 schematically depicts TMD liquid exfoliation broken down into two stages: ultrasonic exfoliation and iterative centrifugation cascades for size selection. Bulk TMD powder (234842 and 243639; Sigma Aldrich, St. Louis, MO USA) was mixed into aqueous sodium cholate at ca. 25 mg ml^{-1}. Sodium cholate (C1254; Sigma Aldrich, St. Louis, MO USA) provided suspension stability and minimized aggregation.[190] The initial sonication and low-speed centrifugation served as a cleaning/purification step. The primary exfoliation step occurred over a 12 hour duration at 360 W to exfoliate the mixture down to mono- and few-layer TMD crystals. After a low-speed centrifugation to remove aggregates and residual bulk crystallites, an iterative series of centrifugations at increasing speeds from 2 krpm to 10 krpm were performed to size-select TMD.[181] Figure 3.3 shows representative scanning transmission electron microscopy (STEM) images of exfoliated (a) MoS_2 and (b) WS_2.

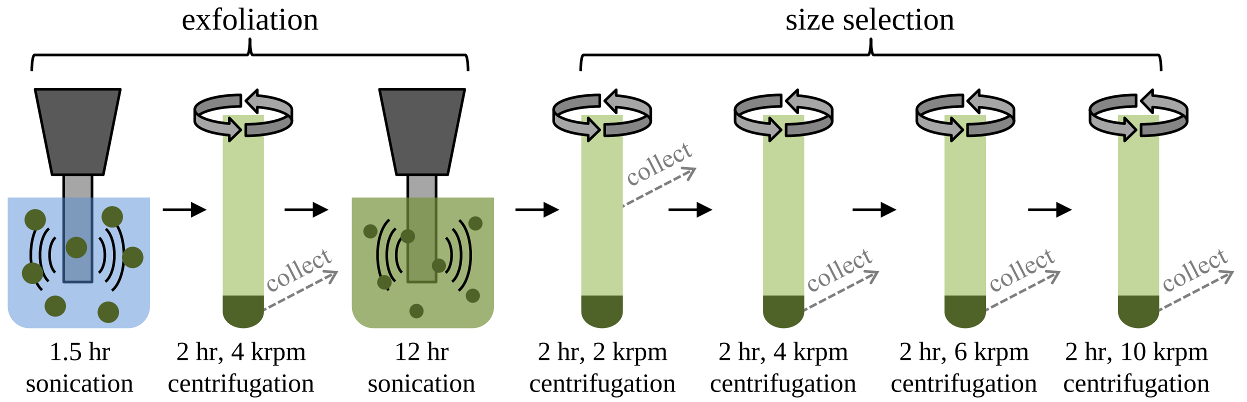

Figure 3.2: Process schematic for liquid phase exfoliation of 2D TMD crystals. Monolayer TMD are obtained from interactive liquid cascade centrifugations after a 12 hr ultrasonic exfoliation.

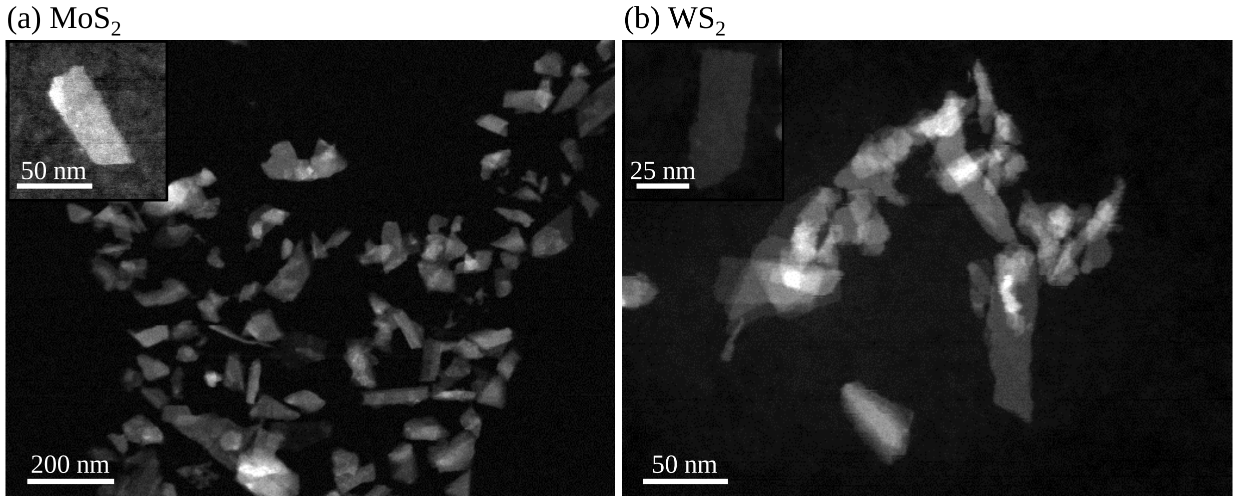

Figure 3.3: High-angular annular dark field STEM (HAADF-STEM) images of liquid exfoliated few- to mono-layer (a) MoS_2 and (b) WS_2 flakes. Accelerating voltage was 200 kV.

Mean size of exfoliated MoS_2 and WS_2 crystals comprising the dispersions were sub-100 nm in length and monolayer in thickness as measured *in situ* by empirical absorbance spectrum metrics.[180,181] The absorbance spectrum contains size/thickness-dependent signatures of electronic structure changes at the crystal edges and quantum confinement.[42,180] Quantitative relationships between absorbance spectra features of disulfide TMD and their dimensions were previously determined according to statistical analyses from transmission electron microscopy (TEM) and atomic force microscopy (AFM) with corroboration by dynamic light scattering (DLS).[181,191] Mean layer quantity per flake, N_{TMD}, was calculated from to the A exciton wavelength, *viz.*[180,181]

$$N_{TMD} = \begin{cases} 2.3 \times 10^{36} e^{-54{,}888/\lambda_A}, & \mathrm{MoS_2} \\ 6.35 \times 10^{-32} e^{\lambda_A/8.51}, & \mathrm{WS_2} \end{cases} . \qquad \text{(Equation 3.1)}$$

Mean length, L_{TMD}, was calculated according to the ratio of absorbance intensity (I) at two carefully selected wavelengths which express their size-dependent scattering behavior[176,192] arising carrier confinement at the crystal edge by Equation 3.2,[180] where intensity at the B exciton and 345 nm were selected for MoS_2 and 235 nm and 290 nm were selected for WS_2.[180,181] Error in N_{TMD} and L_{TMD} were estimated be less than 10%.[180]

$$L_{TMD} = \begin{cases} \dfrac{3.5\dfrac{I_B}{I_{345\,nm}} - 0.14}{11.5 - \dfrac{I_B}{I_{345\,nm}}}, & \text{MoS}_2 \\[2ex] \dfrac{2.3 - \dfrac{I_{235\,nm}}{I_{290\,nm}}}{0.02\dfrac{I_{235\,nm}}{I_{290\,nm}} - 0.0185}, & \text{WS}_2 \end{cases} \qquad \text{(Equation 3.2)}$$

3.2.2 Chemical Vapor Deposition

CVD growth of monolayer TMD presents a scalable avenue amenable with existing high-volume microelectronics manufacturing infrastructure. Figure 3.4 schematically depicts a typical CVD procedure to synthesize monolayer TMD onto a Si wafer in a tube furnace. Taking MoS_2 as an example, sulfur powder is vaporized (ca. 650 ˚C) and carried downstream by an inert gas to partially reduce molybdenum trioxide (MoO_3) into volatile MoO_{3-x} which subsequently adsorbs onto the target substrate and continues reaction with the sulfur to form MoS_2.[183,193]

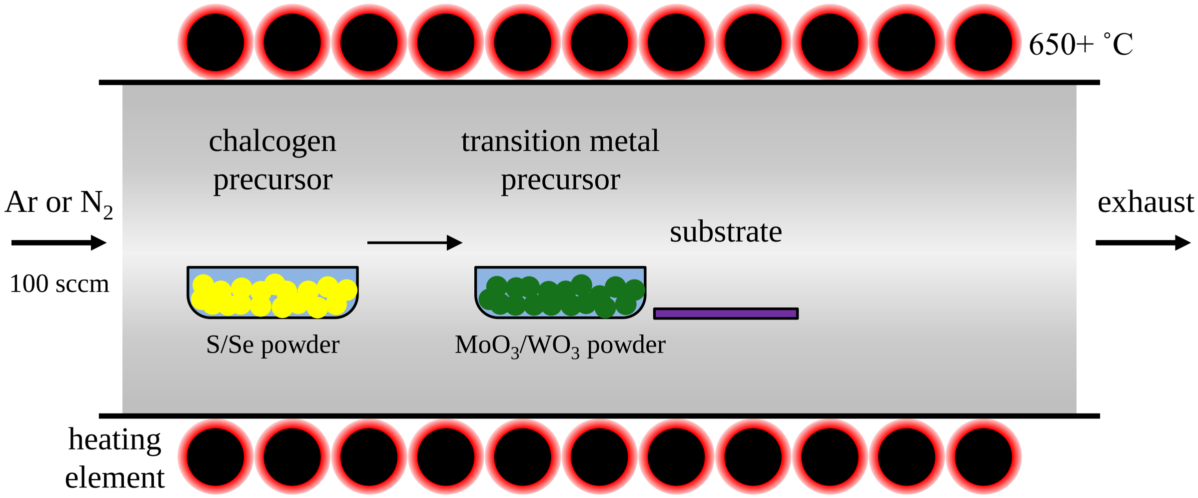

Figure 3.4: Typical process schematic for CVD growth of monolayer group-IV TMD in a tube furnace. Vaporized chalcogen atoms are transported downstream to react with the transition metal trioxides to form monolayer MoS_2, WS_2, $MoSe_2$, or WSe_2 on the adjacent substrate.

The resultant triangular TMD are predominantly monolayer thickness in the absence of defects or use of secondary seed precursors which promote multi-layer nucleation.[186] Continued growth causes the triangular, single crystalline domains to eventually merge and form polycrystalline films.[187] Table 3.1 summarizes 13 reported protocols spanning MoS_2,[183,186–189,194,195] WS_2,[185,189,193] molybdenum diselenide ($MoSe_2$),[184,196] and tungsten diselenide (WSe_2);[197] each are unique to specific furnace configurations. However in the absence of a rigorously tested internal CVD protocol, CVD-synthesized monolayer MoS_2 was sourced externally (CVD-MOS2; 2Dsemiconductors, Scottsdale, AZ USA). Figure 3.5 shows (a) optical bright-field images and (b) scanning electron microscopy (SEM) images of triangular monolayer MoS_2 crystal domains synthesized by CVD.

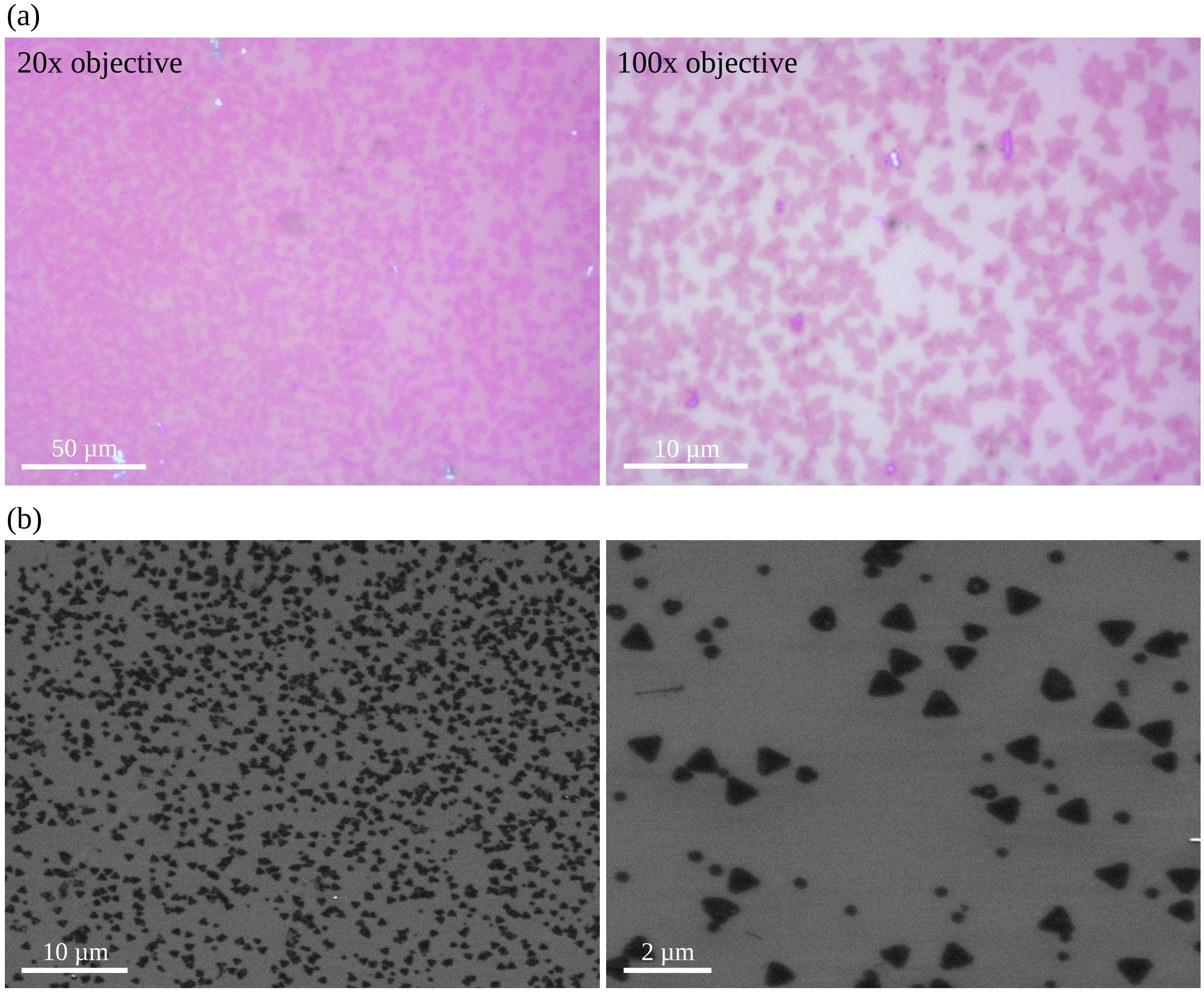

Figure 3.5: (a) Optical 20x and 100x objective bright-field images and (b) SEM images of CVD-synthesized MoS_2 monolayers on a Si wafer. Accelerating voltage was 5 kV.

Table 3.1: Protocol parameters for CVD synthesis of MoS_2, WS_2, $MoSe_2$, and WSe_2.

MX_2 protocol		size order limit	MX_2 Precursors		Environment			Substrate Locale	Seed
			X	M	Gas	Flow [sccm]	T [˚C]		
MoS_2	Lee [182]	1 mm	S powder	MoO_3 powder	N_2	N/A	650	above MoO_3	GO†
	Najmaei [185]	100 µm	S powder	MoO_3 ribbons	N_2	200	850	away	-
	van der Zande [186]	100 µm	S powder	MoO_3 powder	N_2	10	700	above MoO_3	-
	Kim [187]	1 cm	H_2S gas	MoO_3 powder	Ar	200	600	away	-
	Kang [188]	1 cm (wafer)	$(C_2H_5)_2S$ gas	$Mo(CO)_6$ gas	Ar/H_2	150	550	away	-
	Liu [193]	10 µm	S powder	MoO_3 powder	Ar	50	625	above MoO_3	-
	Ling [194]	10 µm	S powder	MoO_3 powder	Ar	5	650	above MoO_3	PTAS‡
WS_2	Cong [184]	100 µm	S powder	WO_3 powder	Ar	100	750	above WO_3	-
	Kang [188]	1 cm (wafer)	$(C_2H_5)_2S$ gas	$W(CO)_6$ gas	Ar/H_2	150/5	550	away	-
	McCreary [192]	10 µm	S powder	WO_3 powder	Ar	100	825	above WO_3	PTAS‡
$MoSe_2$	Wang [183]	100 µm	Se pellets	MoO_3 powder	Ar/H_2*	50	750	above MoO_3	-
	Chang [195]	1 µm	Se pellets	MoO_3 powder	Ar/H_2*	40/10	700	away	-
WSe_2	Huang [196]	10 µm	Se powder	WO_3 powder	Ar/H_2*	80/20	925	away	-

† reduced graphene oxide
‡ perylene-3,4,9,10-tetracarboxylic acid tetrapotassium salt
* H_2 required to selenize the transition metal trioxide precursor[183,196]

3.3 Spectroscopic Characterization

Transmission UV-vis absorbance, photoluminescence (PL), and Raman spectroscopies were performed to interrogate the optoelectronic and physical properties of MoS_2 and WS_2. Figure 3.6 shows normalized transmission UV-vis absorbance spectra for (a) MoS_2 and (b) WS_2 liquid exfoliated into water with each exciton transition labeled. The A and B transition occurred at 1.87 eV and 2.06 eV, respectively, for MoS_2. The A and B excitons both correspond to direct transitions across the K point of the Brillouin zone, but differ in energy because of spin-split valence bands.[42] The C transition occurred at 3.14 eV. The C exciton corresponds to a van Hove singularity where electronic bands are locally parallel between Γ and Λ points (called the "nesting" region), which is responsible for its large bandwidth.[198,199] The A, B, and C excitons of WS_2 occurred at 2.02 eV, 2.44 eV, and 3.41 eV, respectively. The high energy absorbance maxima beyond the C transition (4.02 eV for MoS_2 and 5.35 eV for WS_2) has not been examined or attributed in the literature, but was ostensibly related to an additional exciton transition.

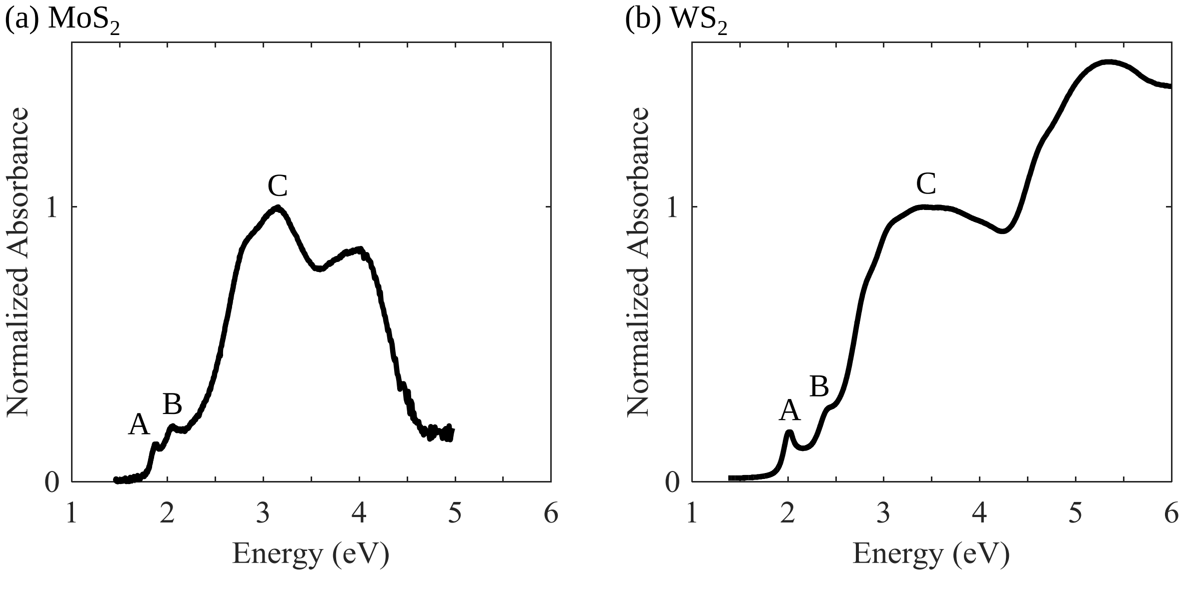

Figure 3.6: Normalized transmission UV-vis spectra of (a) MoS_2 and (b) WS_2 showing the A, B, and C exciton transitions. Spectra were each normalized to the C transition.

To confirm direct bandgap behavior and provide a benchmark for A exciton energy from high-quality monolayer MoS_2, PL was examined from CVD-synthesized MoS_2,[200] shown in Figure 3.7. A PL peak at 1.86 eV was observed, corresponding to the A exciton and was consistent with other reports.[187,201,202] Strong PL emission confirmed direct bandgap behavior. PL is negligible from indirect bandgap semiconductors, where electrons require assistance from phonons to jump from the valence to conduction band and thus preclude efficient radiative recombination.[110] A small shoulder occurred around 2 eV which corresponded with the B exciton, whose emission is suppressed in monolayer TMD.[42] CVD-grown WS_2 was not available for study.

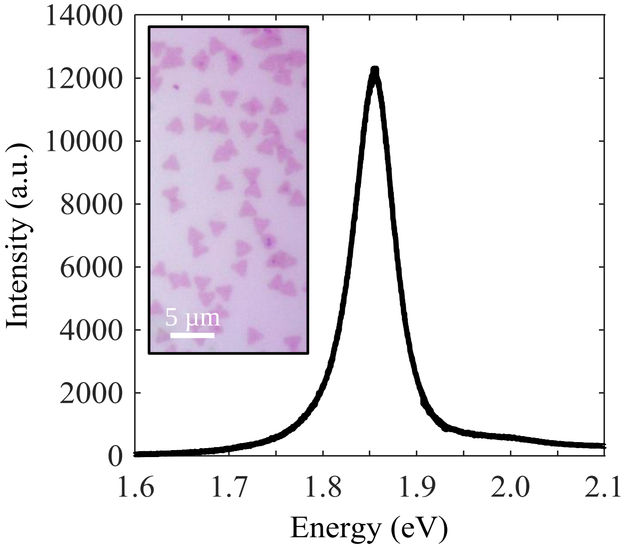

Figure 3.7: PL emission from CVD grown MoS_2 on a Si wafer with maxima at 1.86 eV. Excitation wavelength was 488 nm (2.54 eV).

Layer-dependent changes in the coupling between K electronic transitions and molecular vibrations (i.e., phonons) provided Stoke shift signals as a fingerprint of N_{TMD}. Figure 3.8 shows normalized Raman spectra of the Stoke shift signals from liquid exfoliated (dashed) and CVD-grown (solid) MoS_2,[200,203] whose E_{2g}^1 and A_{1g} frequencies confirmed monolayer thicknesses for each. The E_{2g}^1 peak corresponds to in-plane vibrations of chalcogens against the transition metal, which are dominated by inter-layer Coulombic screening interactions.[204,205] The A_{1g} peak corresponds to out-of-plane opposing vibrations of chalcogens, which are dominated by van der Waals forces between layers.[204] Liquid exfoliated MoS_2 exhibited Raman peaks at 384 cm^{-1} and 408 cm^{-1} for E_{2g}^1 and A_{1g} modes, respectively. The CVD-synthesized MoS_2 exhibited Raman peaks at 385 cm^{-1} and 407 cm^{-1} for E_{2g}^1 and A_{1g} modes, respectively; lower frequency peaks at 350-365 cm^{-1} were noise arising from the normalization. The E_{2g}^1 and A_{1g} Raman frequencies fell within reported thresholds for monolayers.[204] Intensity and width of Raman signatures vary arbitrarily between samples and hold no information.[204] CVD-grown WS_2 was not available for benchmarking against liquid exfoliated WS_2.

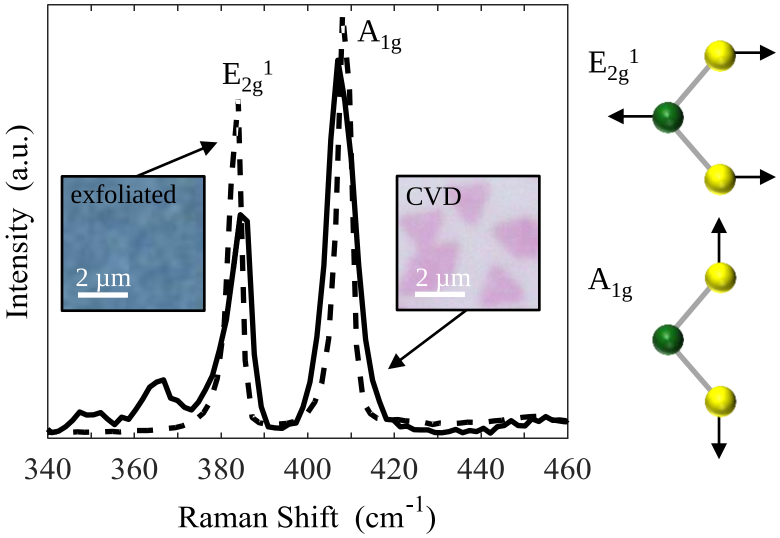

Figure 3.8: Raman spectra of liquid exfoliated (dashed) and CVD-synthesized (solid) MoS_2 on SiO_x. In-plane E_{2g}^1 and out-of-plane A_{1g} vibrational modes are labeled and shown schematically. Optical images from areas which were measured are inset. Excitation wavelength was 488 nm.

3.4 Measurement of $\chi^{(2)}$ for Monolayer Transition Metal Disulfides

Strength of second order nonlinear frequency mixing from material may be quantified by its intrinsic nonlinear susceptibility, $\chi^{(2)}$.[32] Measurements of $\chi^{(2)}$ for monolayer MoS_2 and WS_2 to date[48–52] vary across 10^2-10^4 pm V^{-1} because of reliance on indirect classical calculations based on α-quartz references and/or Green's function, where "bulk" versus "sheet" treatment significantly impacts the calculation.[49] Models estimate $\chi^{(2)}$ at 10^2 pm V^{-1} off-resonance and up to 10^3 pm V^{-1} on-resonance using density functional theory (DFT) with and without a scissors correction,[49,206] density matrix theory (DMT),[54] and the Bethe-Salpeter exciton (BSE) method.[53] Disagreement in $\chi^{(2)}$ spanning three orders of magnitude motivated independent, direct measurements to circumvent established indirect methods.

Hyper Rayleigh Scattering (HRS) directly measured $\chi^{(2)}$ at 523 nm herein to be 660±130 pm V^{-1} and 280±18 pm V^{-1} for liquid exfoliated MoS_2 and WS_2 monolayers, respectively.[207] Liquid exfoliated TMD permitted use of HRS, a technique which CVD and mechanically exfoliated crystals (on which previous studies were based) cannot accommodate. HRS was originally developed to study hyperpolarizability, β, of organic molecule solutions,[208] and has since been used to study β and $\chi^{(2)}$ of inorganic nanoparticles.[209,210] Briefly, a polarized, 1 ns pulsed 1064 nm Nd:YAG laser (Wedge HB; Bright Solutions, Cura Carpignano, IT) was focused into a quartz cuvette containing the TMD dispersion and second harmonic (SH) signal at 532 nm was orthogonally collected without an analyzer and measured by a photomultiplier tube (PMT). See Figure 3.9 and Ref. 207 for details.

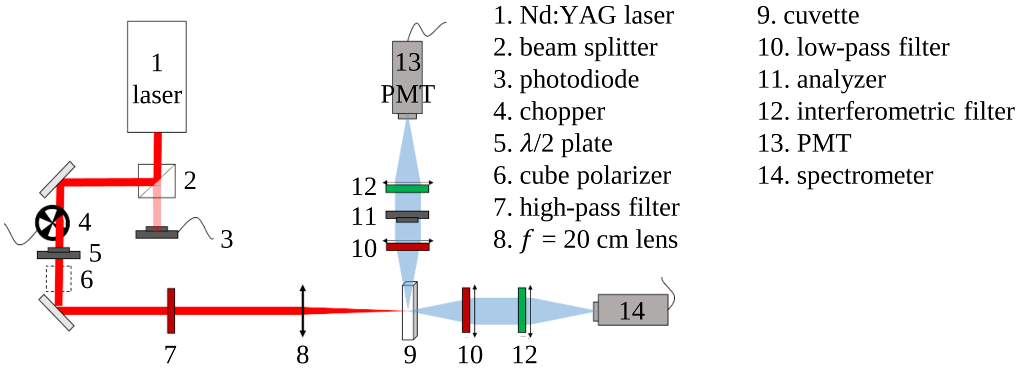

Figure 3.9: Schematic for HRS measurements of MoS_2 and WS_2 by a 1064 Nd:YAG laser.

3.4.1 Hyper Rayleigh Scattering

HRS interrogates the orientation-averaged nonlinear efficiency of nanoparticle suspensions by correlating intensity scattered SH signal with nanoparticle concentration.[208–210] Intensity of HRS is defined as the incoherent sum of scattered SH frequencies by a composite media:

$$I_{HRS} = {I_\omega}^2 G \sum_i C_i F_i \langle {\beta_i}^2 \rangle \qquad \text{(Equation 3.3)}$$

where I_ω is the excitation intensity, $\langle \beta \rangle$ is the isotropic second-order hyperpolarizability of material i with concentration C, F is a local field enhancement factor, and G is an experimental constant. Unlike $\chi^{(2)}$ treatment of polarization density ($\boldsymbol{P}^{(2)}$) in macroscale crystals, β describes the magnitude of an induced second-order dipole moment, ${\boldsymbol{p}_{HRS}}^{(2)}$, on a subwavelength molecule driven by the local electric field, $\boldsymbol{E}_{loc} = F\boldsymbol{E}_o$, *viz.*

$${\boldsymbol{p}_{HRS}}^{(2)} = \beta {\boldsymbol{E}_{loc}}^2 \ . \qquad \text{(Equation 3.4)}$$

“Hyper Rayleigh Scattering” is nomenclature convention given to SH scatterers whose size fall within the subwavelength Rayleigh regime. Independent size/spatial characterization of nanoparticles comprising the ensemble permits straightforward conversion of per-nanoparticle β to bulk crystal $\chi^{(2)}$.

Second-order $\langle \beta \rangle$ for exfoliated MoS_2 and WS_2 were measured to be 4.03±0.78x10^{-24} esu and 4.90±0.30x10^{-25} esu,[207] respectively, using the HRS external reference protocol with para-nitroaniline (pNA).[210] Here, I_{HRS} was recorded as a function of TMD concentration, as shown in Figure 3.10(a). To determine $\langle \beta_{TMD} \rangle$, the slope $\alpha_{TMD} = {I_\omega}^2 G F_{TMD} \langle {\beta_{TMD}}^2 \rangle$ was scaled against the slope for positive-control pNA with a defined $\langle \beta \rangle$, but with addition of a $e^{-\sigma_{TMD}}$ Beer-Lambert correction factor for self-absorbance of the SH by the TMD,[211,212] *viz.*

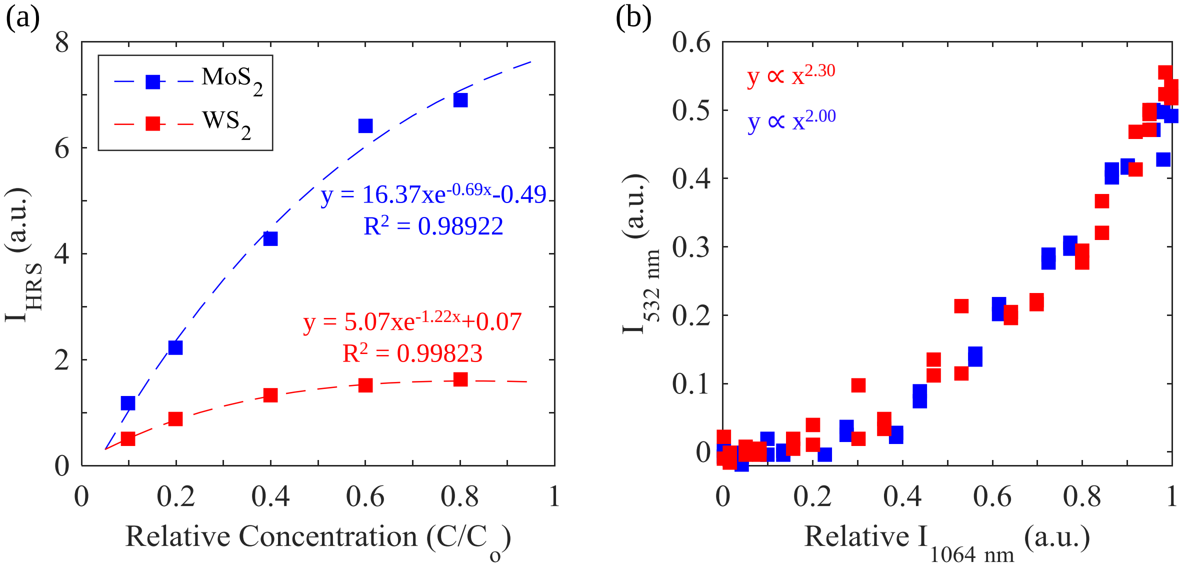

Figure 3.10: (a) HRS intensity as a function of relative MoS$_2$ (blue) and WS$_2$ (red) concentration with superposed regressions of the form $I_{HRS} = \alpha_{TMD}(C/C_o)exp[-\sigma_{TMD}(C/C_o)] + I_{HRS-solvent}$. (b) Representative power dependence of collected signal at C_o for (i) MoS$_2$ and (ii) WS$_2$ confirming second-order nonlinear process.

$$\langle\beta_{TMD}\rangle = \sqrt{\frac{\alpha_{TMD}F_{pNA}}{\alpha_{pNA}F_{TMD}e^{-\sigma_{TMD}}}}\langle\beta_{pNA}\rangle \qquad \text{(Equation 3.5)}$$

The local field correction factor F_{pNA} was calculated *a priori* by the Lorentz-Lorenz correction[208] and F_{TMD} was set to 1 since no analytic expression exists for a 2D sheet. Reference $\langle\beta_{pNA}\rangle$ used was $\sqrt{6/35}\,\beta_{33} = \sqrt{6/35}$ (25.9x10^{-30} esu),[213] where $\sqrt{6/35}$ was the Kleinman weighting factor unique to vertically polarized excitation and unpolarized detection.[208] The excitation intensity, I_ω, and experimental proportionality constant, G, (comprising e.g., collection efficiency) were unchanged between respective trials, and thus assumed constant.

Progressive dilution of the stock MoS$_2$ and WS$_2$ concentrations, C_o = 2.7x10^{11} cm^{-3} and 9.6x10^{12} cm^{-3}, respectively, gave expected linear I_{HRS} behavior at lower relative concentrations with suppressed linearity at higher concentrations by SH (2.3 eV) absorption above the direct TMD bandgap (1.87-2.02 eV). Despite Beer-Lambert absorption at higher concentrations, I_{HRS} scaled quadratically with excitation power with coefficients ranging from 2.0-2.3 at C_o, thus confirming second-order processes [see Figure 3.10(b)].[33] Highest re-absorption was observed for WS_2 (deviations from linear behavior beginning at about C/C_o = 0.4), consistent with its reported higher extinction coefficient than MoS_2.[214] Linear behavior can be readily recovered, however, by dilution to lower concentrations. Dilution decreases the Beer-Lambert absorption correction $e^{-\sigma_{TMD}(C/C_o)}$ from $e^{-0.05} \approx 0.95$ back up to 1, and thus becomes a negligible factor in I_{HRS} from the TMD.[212] Higher concentrations were included in this work for further confidence in physical significance of fitted numerical regressions, despite re-absorption of the SH.

Nonlinear regressions of the form $I_{HRS} = \alpha_{TMD}(C/C_o)e^{-\sigma_{TMD}(C/C_o)} + I_{HRS-solvent}$ performed on the MoS_2 and WS_2 HRS data readily provided necessary parameters to calculate $\langle\beta_{TMD}\rangle$. All fitted parameters with error are tabulated in Table 3.2. Common units between α_{TMD} and α_{pNA} are required prior to use of Equation 3.5, and thus each were normalized to their respective C_o (Avogadro's number for α_{pNA}). The y-axis intercept from the origin calculated by the nonlinear regression intrinsically represented the near-zero SH contribution from the solvent (aqueous sodium cholate) and quartz cuvette.

Table 3.2: Summary of parameters extracted for numerical regressions of the form $y = Axe^{-Bx} + C$ for TMD and linear regressions of the form $y = Ax + C$ for pNA. Data for MoS_2 and WS_2 were taken at different powers and thus pNA data at each respective power was recorded.

	A		***B***	***C***
	relative to C/C_o	**relative to C_o**		
MoS_2	16.3709±4.3698	6.1207±1.6338 x10^{-11}	0.6853±0.2725	-0.4905±0.6401
pNA	2.0380±0.1126	3.3840±0.1870 x10^{-21}	-	-0.0689±0.0207
WS_2	5.0719±0.4177	5.2722±0.0430 x10^{-13}	1.2190±0.0775	0.0665±0.0537
pNA	2.0206±0.0956	3.3550±0.1590 x10^{-21}	-	0.2735±0.0149

3.4.2 Orientation-Averaged $\chi^{(2)}$ Coefficients

The $\chi^{(2)}$ at 532 nm (i.e., 2ω of 1064 nm) for MoS_2 and WS_2 was calculated to be 660±130 pm V^{-1} and 280±18 pm V^{-1}, respectively.[207] Although β expresses second-order nonlinear efficiency on a per-nanoparticle basis, $\chi^{(2)}$ is an intrinsic property of said material and allows direct correspondence with CVD crystals. In the absence of SH surface contributions to I_{HRS}, β is readily converted to $\chi^{(2)}$ by

$$\langle\chi^{(2)}\rangle = \frac{2\langle\beta\rangle}{V} \qquad \text{(Equation 3.6)}$$

where V is the nanoparticle volume with non-centrosymmetric crystal structure (extracted herein from Figure 3.6 and Equations 3.1 and 3.2).[210] Second-order nonlinear processes rely on crystalline non-centrosymmetry of odd-layered TMD; even-layered stacking suppresses second-order response by inversion symmetry restoration.[50,169] Monolayer TMD exhibit D_{3h} point-group symmetry giving a single non-zero $\chi^{(2)}$ tensor element $\chi_{xxx}{}^{(2)} = -\chi_{xyy}{}^{(2)} = -\chi_{yyx}{}^{(2)} = -\chi_{yxy}{}^{(2)}$, where x and y are crystal axes. Thus, brackets indicating orientational averaging were neglected for the special case of monolayer TMD since finite $\chi^{(2)}$ originated from the same tensor element.

Measured $\chi^{(2)}$ by HRS agreed well with other reported experimental and theoretical estimates. Table 3.3 summarizes measured and calculated $\chi^{(2)}$ using a variety of methods for both MoS_2 (row 1) and WS_2 (row 2) monolayers. By comparison to the measured 660 pm V^{-1} $\chi^{(2)}$ for MoS_2, experimental estimates spanning 20-400 pm V^{-1} have been calculated by scaling MoS_2 SH generation (SHG) intensity to an α-quartz reference;[49,50] theoretical estimates by DFT, DMT, and BSE indicate 400-900 pm V^{-1}.[49,53,54,206] By comparison to the measured 280 pm V^{-1} $\chi^{(2)}$ for WS_2, the one reported work to date estimated 170 pm V^{-1} via DFT and measured 9000 pm V^{-1} at 416 nm via a sophisticated Green's function calculation.[52] No measurements of SHG from WS_2 by

1064 nm irradiation have been reported for a direct comparison. Other studies measuring SHG from TMD monolayers were limited to 810 nm irradiation,[48,51] and thus their $\chi^{(2)}$ estimations could not be directly compared herein.

Table 3.3: Literature comparison of measured and calculated $\chi^{(2)}$ values at 532 nm (2ω of 1064 nm excitation) for monolayer MoS_2 and WS_2.

	HRS [pm V^{-1}]	**Measured [pm V^{-1}]**		**Simulated [pm V^{-1}]**		
		α-quartz ext. ref.	**Green's function**	**DFT**	**DMT**	**BSE**
MoS_2	660±130	20-400 [49,50]	-	400† [49,205]	400 [54]	900 [53]
WS_2	280±17	-	9000‡ [52]	170 [52]	-	-

† with and without scissors correction
‡ taken at 416 nm; no measured 532 nm values reported to date

Measured $\chi^{(2)}$ for MoS_2 and WS_2 herein may have been lower-end estimates due to the wide size/thickness heterogeneity of TMD crystals inherent to exfoliated dispersions, despite significant distribution reduction from the cascade centrifugations. Recent reports indicate SHG intensity exponentially decays with N_{TMD} in odd-layer TMD crystals, e.g., a 50% reduction for trilayer (from 1/3 $\chi^{(2)}$ reduction[206]) and an 80% reduction for pentalayer versus the monolayer signal.[169] Crystalline inversion symmetry in even-layered TMD suppresses SHG, in the absence of an electrical bias.[215] Therefore, it was inevitable some TMD crystals comprising the liquid exfoliated dispersion contributed little or no SH signal to the penultimate I_{HRS} from which β and $\chi^{(2)}$ were obtained. Importance of sample preparation for HRS experiments has been detailed.[210]

3.4.3 Discrete Dipole Computation of $\chi^{(2)}$ via Miller's Rule

A nonlinear extension of approximate discrete dipole Maxwell's equations (i.e., DDA) via Miller's rule estimated $\chi^{(2)}$ at 532 nm for MoS_2 to be 460 pm V^{-1}, which was within a factor of 2 of HRS measurements.[207] Miller's rule states that the ratio between nonlinear $\chi^{(2)}$ and the product of linear susceptibilities, χ, at the input and output frequencies is nearly constant for all non-centrosymmetric condensed matter.[33,216] In other words, the nonlinear response is directly related to the linear response scaled by a proportionality factor. The DDA readily calculates linear polarizability, α,[92] and extensively χ, by the Lattice Dispersion Relation.[101] Thereby DDA offered an accessible, *a priori* method to evaluate second-order nonlinear optical behavior at significantly less computational cost than DFT, DMT, or BSE provided (i) availability of a dielectric function and (ii) lack of crystalline inversion symmetry.

Linear polarizability of a 2D rectangular sheet of MoS_2 was calculated by DDSCAT v7.3.[90,100] Its translation to $\chi^{(2)}$ assumed $\Im(\alpha)$ due to its relation to photon scattering.[74] Dielectric data for monolayer MoS_2 was taken from Mukherjee *et al*.[217] Absence of a rigorous dielectric function for monolayer WS_2 precluded its corresponding evaluation. The Miller proportionality factor is a function of material constants: free space permittivity ϵ_o, electron mass m, carrier density $N \sim 10^{22}$ cm^{-3}, electron charge e, and some nonlinear strength coefficient a. Equation 3.7 expresses Miller's rule in the context of SHG.[33]

$$\chi_{2\omega}^{(2)} = \frac{{\epsilon_o}^2 ma}{N^2 e^3} \chi_{2\omega} (\chi_\omega)^2 \qquad \text{(Equation 3.7)}$$

Charge displacement from equilibrium in a nonlinear Lorentz oscillator can be estimated to be on the order of inter-atomic separation, d, such that $a \sim {\omega_o}^2/d$, where ω_o is some resonant oscillation frequency.[33] The C exciton transition for MoS_2 was assumed for ω_o (because of its proximity within the 2ω spectrum) and 2.7 Å for d (corresponding to {100} planes).[218]

Frequency dependence of $\chi^{(2)}$ for monolayer MoS_2 arising from its expanded density of states around the C transition due to its van Hove singularity is shown in Figure 3.11. At 532 nm, $\chi^{(2)}$ was calculated to be 460 pm V^{-1}, within a factor of 2 of the HRS measurement (blue square).

A 1642 pm V^{-1} maxima occurred at 444 nm, coinciding with the C transition. Theoretical estimates by DFT with and without scissors correction (Δ_{SCI}), DMT, and BSE also found close relation between $\chi^{(2)}$ and the C exciton in this spectral region,[49,53,54,206] consistent with these data and those measured by Malard *et al.*[50] Lack of interband transitions above 700 nm (≤ 1.77 eV) minimized impact of χ_{ω} on $\chi^{(2)}_{2\omega}$ despite quadratic dependence in Equation 3.7. Direct absorption at the 660 nm A transition resulted in an intense $\chi^{(2)}$ resonance at higher energy wavelengths, but this regime was not accessible by conventional laser/detection metrology.

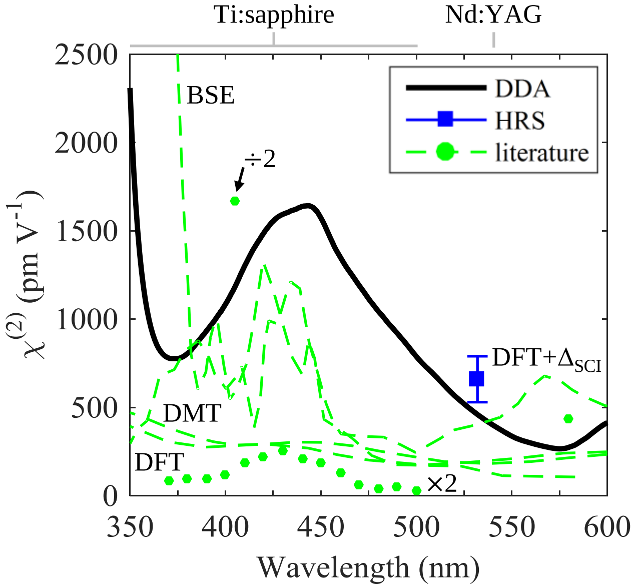

Figure 3.11: Frequency dependent $\chi^{(2)}$ spectra for MoS$_2$ calculated by DDA via Miller's rule. Measured value at 532 nm by HRS is superposed. Literature measurements (circles) and theoretical calculations (dashed lines) from DFT, DFT+Δ_{sci}, DMT, and BSE are also superposed for comparison. Frequencies accessible by Ti:sapphire and Nd:YAG lasers are marked.

3.5 Summary

The linear and extraordinary nonlinear optical properties of 2D MoS$_2$ and WS$_2$, the sulfide class of group-IV TMD, were examined using transmission UV-vis, PL, and Raman spectroscopies and HRS. Fabrication of monolayer TMD crystals by natural exfoliation (specifically, by liquid means) and synthetic CVD was described. Transmission UV-vis and PL spectroscopies revealed three direct optical transitions in the electronic band structure of MoS_2 and WS_2. Raman spectroscopy confirmed monolayer TMD thicknesses by in-plane and out-of-plane phonon interactions unique to monolayers. HRS experiments of nonlinear SHG from liquid exfoliated MoS_2 and WS_2 permitted their first direct $\chi^{(2)}$ measurement of 660±130 pm V^{-1} and 280±18 pm V^{-1} at 532 nm, respectively, and was corroborated by an elegant Miller's rule adaptation to the linear DDA. Overall, the linear and nonlinear optoelectronic properties of 2D TMD monolayers were surveyed and measured for their use in optoelectronics.

CHAPTER 4

INTERFACING MONOLAYER TRANSITION METAL DICHALCOGENIDES WITH NANOANTENNAS

Decorating transition metal dichalcogenide (TMD) field-effect photodetectors,[57,219–221] photocatalysts,[30,58,222,223] and solar photovoltaic cells[224] with metal nanoantennas has demonstrably improved their performance, ostensibly through augmented charge separation and photodoping. Nanoantennas can enhance emission from TMD up to 10x by optimizing plasmon-exciton coupling.[219,221,225,226] However, phonon scattering,[20] photo-induced doping from plasmonic hot electrons,[16] and inherent quenching[227] limit TMD emission enhancements by surface plasmons. Advancement beyond initially promising prototypes has been constrained by inability to interpret experimental results with compact, experimentally validated models. The discrete dipole approximation (DDA) was introduced herein to characterize predominant optoelectronic modes observed in transmission UV-vis extinction spectra of TMD-nanoantenna heterostructures.

4.1 Fabrication Techniques

Plasmonic nanoantennas were interfaced with liquid exfoliated TMD by (i) top-down drop-casting[228] and (ii) bottom-up *in situ* chemical methods.[229] Use of liquid suspensions of TMD (i.e., liquid exfoliated) and nanoantennas (i.e., colloidal dispersions from wet-chemical synthesis) allowed facile, economical heterostructure formation onto a variety of substrates. Heterostructure samples were deposited onto silica (SiO_x) for spectroscopic characterization by a bright-field optical microscope (Eclipse LV100; Nikon Instruments, Melville, NY USA) coupled to a spectrometer (Shamrock 303; Andor Technology, Belfast, UK) and/or transmission electron microscopy (TEM) analysis (Titan^3 80-300; FEI, Hillsboro, OR USA).

4.1.1 Drop Cast

Gold (Au) nanospheres and silver (Ag) nanoprisms were drop-cast onto monolayer molybdenum disulfide (MoS_2) covered SiO_x glass.[230] Au nanospheres 76±13 nm in diameter with poly(vinylpyrrolidone) (PVP) ligand (GEPE75; nanoComposix, San Diego, CA USA) were dispersed in isopropanol to a concentration of 2.3×10^9 mL^{-1}. Ag nanoprisms 53±19 nm in edge length and 10 nm thickness with PVP ligand (SPPN550; nanoComposix, San Diego, CA USA) were dispersed in 5 mM aqueous sodium borate to a concentration of 1.6×10^{11} mL^{-1}. Substrates were cleaned in 25% nitric acid for 30 minutes to improve their hydrophilicity, rinsed in distilled-deionized water, and dried under nitrogen gas. MoS_2 was deposited onto preheated SiO_x by a 1.5 μL drop. Successively, MoS_2-covered SiO_x substrates were heated to 90 ˚C (105 ˚C) for additional drop-cast of 5 μL (10 μL) volumes of Au-isopropanol (Ag-water). The pre-heat rapidly evaporated solvent to minimize aggregation from contact-line pinning. See Ref. 230 for details.

Visual and spectroscopic examples of singularly drop-cast (a) MoS_2, (b) Au nanospheres, and (c) Ag nanoprisms are shown in Figure 4.1, exhibiting no apparent signs of aggregation. Optical images were taken in bright-field reflection mode with a 100x objective. Insets in (a) shows Raman and (b)-(c) transmission UV-vis extinction spectra of the imaged areas. The in-plane E_{2g}^1 and out-of-plane A_{1g} Raman modes for deposited MoS_2 were measured to be 384 cm^{-1} and 408 cm^{-1},[203] respectively, confirming no aggregation.[204] Localized surface plasmon resonances (LSPR) of Au nanospheres and Ag nanoprisms were measured at 561 nm and 687 nm, respectively, in agreement with cuvette measurements; aggregation causes LSPR red-shifts. Although deposited MoS_2 altered the SiO_x surface hydrophilicity prior to forming heterostructures with nanoantennas, no spectral signatures appeared from accrued aggregation beyond the pristine SiO_x surface (to be detailed in forthcoming sections).

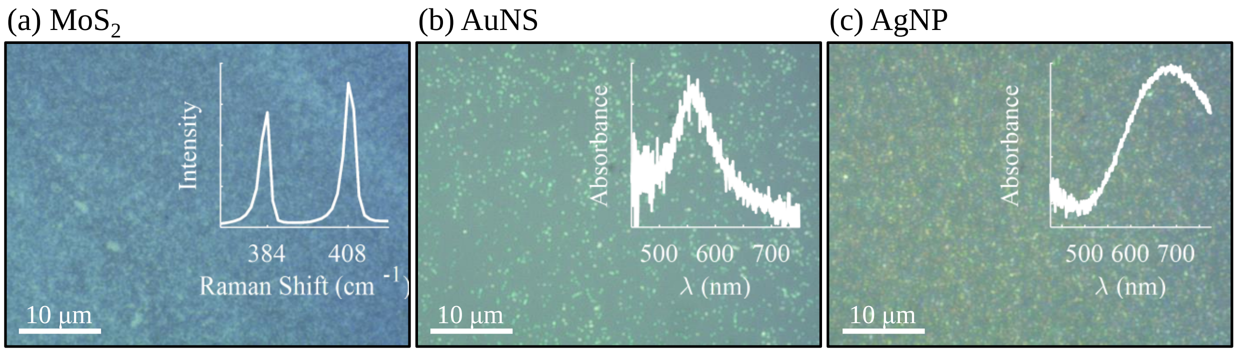

Figure 4.1: Optical bright-field images taken at 100x objective magnification of (a) mono- to few-layer MoS_2, (b) Au nanospheres (AuNS) with 76±13 nm diameter, and (c) Ag nanoprisms (AgNP) with 53±19 nm edge length drop-cast deposited onto SiO_x. Upper insets show (a) Raman and (b)-(c) transmission UV-vis extinction spectras.

4.1.2 in situ *Chemical Reduction*

Stochastic distributions of quasistatic gold nanoantennas were grown *in situ* onto liquid exfoliated tungsten disulfide (WS_2) by a batch chemical reduction process,[229] shown in Figure 4.2. Gold chloride ($AuCl_3$; 334049; Sigma Aldrich, St. Louis, MO USA) was added in bulk to aqueously stabilized WS_2 (see § 3.2.1), whereby Au was reduced to form nanoantennas preferentially at the edges of the WS_2 crystals. Figure 4.3(a)-(c) show aberration-corrected TEM images of three representative Au-decorated WS_2 crystals used in this work. The 2.3 Å (111) Au constant and 1.6/2.7 Å {110}/{111} WS_2 constants were measured by fast-Fourier transform (FFT) in Figure 4.3(d).

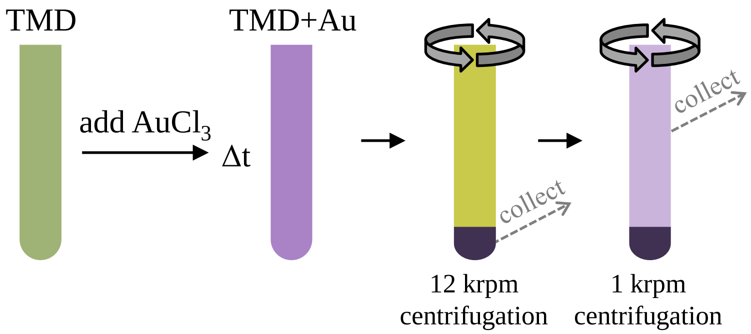

Figure 4.2: Process schematic for *in situ* decoration of liquid exfoliated TMD crystals with AuNA. Gold salt was added to aqueously suspended WS_2 to nucleate/grow AuNA at the edges of the WS_2 crystals. Subsequent centrifugation steps removed residual Au salt and bulk Au.

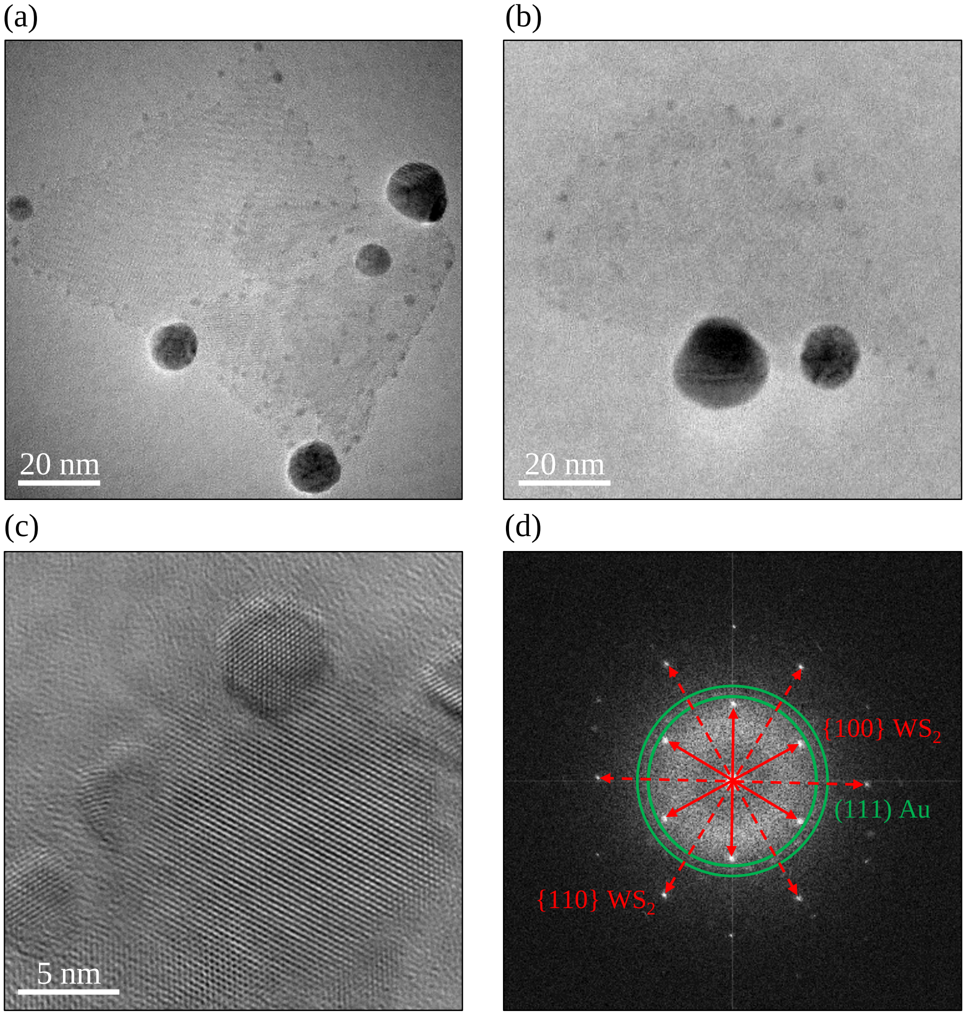

Figure 4.3: (a)-(c) Aberration-corrected TEM images of increasing magnification and (d) FFT of liquid exfoliated WS_2 crystals decorated *in situ* with AuNA.

Dangling sulfur atoms predominantly at the WS_2 crystal edges and basal plane lattice defects served as reduction sites for Au nucleation.[231] Growth of nucleated Au into nanoantennas was controlled by the stoichiometric ratio between $AuCl_3$ and WS_2. A relatively low 1 stoichiometric ratio was chosen herein to promote growth of few Au nanoantennas (AuNA) to 15-30 nm diameter and numerous sub-5 nm nanoantennas. A wide-range exploration of process parameters on the outcome of Au-decorated WS_2 is detailed in Ref. 229. This protocol served as an alternative to drop-cast methods, but ongoing refinement of the chemistry prevented its use throughout this work. Protocols for *in situ* decoration of MoS_2 with Au, Ag, palladium, and platinum sans covalent bonding have also been described.[58,222,232]

4.2 Discrete Dipole Model

Far-field optical extinction spectra showing LSPR and bandgap excitation modes of nanoantenna-MoS_2 heterostructures were modeled using the DDA solutions to Maxwell's equations.[230] A single (i) AuNS of 76 nm diameter and (ii) triangular AgNP of 53 nm (assumed equilateral) edge length with 10 nm height were each discretized into a cubic lattice of point dipoles according to their Cartesian description and placed onto a two-dimensional (2D), dipole-discretized circular plane of MoS_2 atop a SiO_x cylinder. Each dipole was susceptible to electromagnetic polarization by a polarized plane wave according to its specified dielectric function (Au/Ag[113] or MoS_2[217]). Maxwell's equations were solved by DDSCAT v7.3.[100–102] The SiO_x cylinder was given a radius and height equal to twice the nanoantenna radius based on the plasmonic decay length;[97,233] surface plasmons only "see" media within approximately one nanoantenna radius beyond its surface.[106] Figure 4.4 shows the corresponding target heterostructures, discretized for the DDA.

Little precedent existed for use of DDA to accurately simulate optics of 2D materials at the time of this work. Metal-graphene heterostructures were modeled with the DDA beginning in 2014,[234,235] but were not corroborated with experimental results. Boundary element method (BEM) and finite difference time domain (FDTD) algorithms appeared concomitantly with this work to study Au-TMD heterostructures, but were limited to estimating strength of local plasmonic electric fields.[221,236] Open-source DDA (i) significantly reduced computational requirements (e.g., time and memory) over BEM and FDTD and (ii) was not limited to geometries whose volumes may be approximated as one-dimensional surface contour, as in BEM. Neither DDA, BEM, or FDTD can represent TMD edge states[237] because of their classical dielectric function treatment, as opposed to spatial electron density utilized in density functional theory (DFT) models.

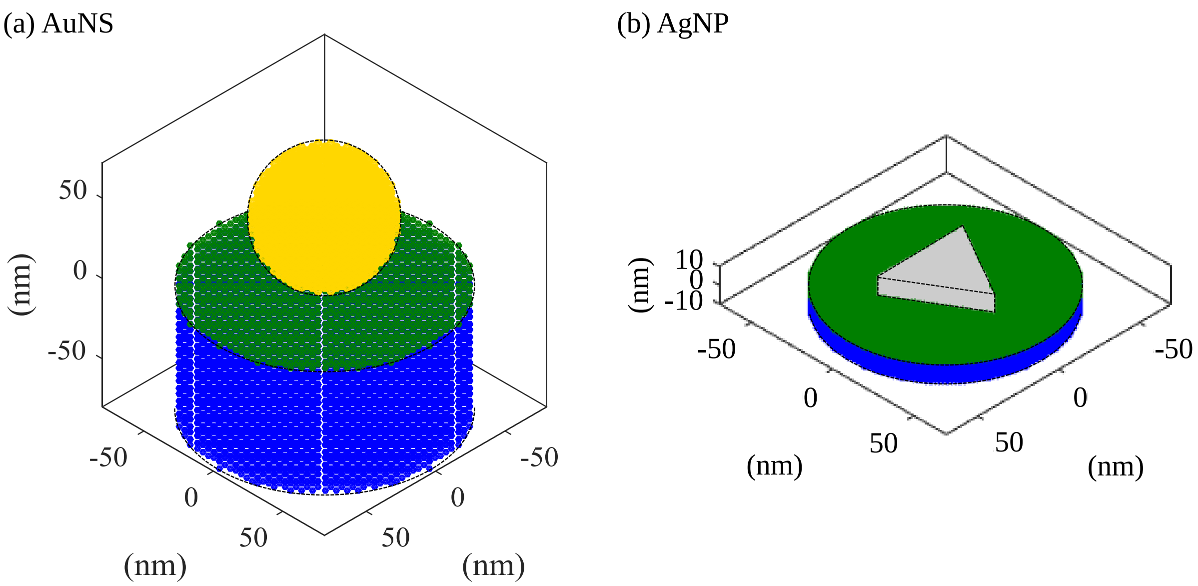
(a) AuNS

(b) AgNP

Figure 4.4: DDA targets of (a) 76 nm Au nanosphere and (b) 53 nm Ag nanoprism on a monolayer of MoS_2 atop a SiO_x substrate. Inter-dipole spacings were 4 nm and 1 nm, respectively. Point dipoles comprising the target are illustrated as spheres: yellow represents Au, gray represents Ag, green represents MoS_2, and blue represents SiO_x.

4.3 Interfacing with Gold Nanospheres

Interfacing monolayer MoS_2 with 76±13 nm Au nanospheres resulted in a hybridized optical extinction spectra with a 4 nm red-shifted LSPR from MoS_2 screening whose bandwidth was expanded 19%, indicative of augmented damping from the MoS_2.[230] Figure 4.5(a) shows measured (solid, LHS axis) and calculated (dashed, RHS axis) optical extinction spectra for a 76 nm diameter Au nanosphere on monolayer MoS_2 atop a SiO_x substrate (black data). Maximas corresponding to nanosphere LSPR and the A exciton of MoS_2 were observed at 566 nm and 670 nm (1.85 eV), respectively. The B exciton was not observable because of the higher intensity

LSPR. For comparison, optical extinction spectra are also shown for independently deposited Au nanospheres (red) and MoS_2 (green). All spectral features were observed in triplicate or greater in multiple areas of each sample to verify reproducibility.

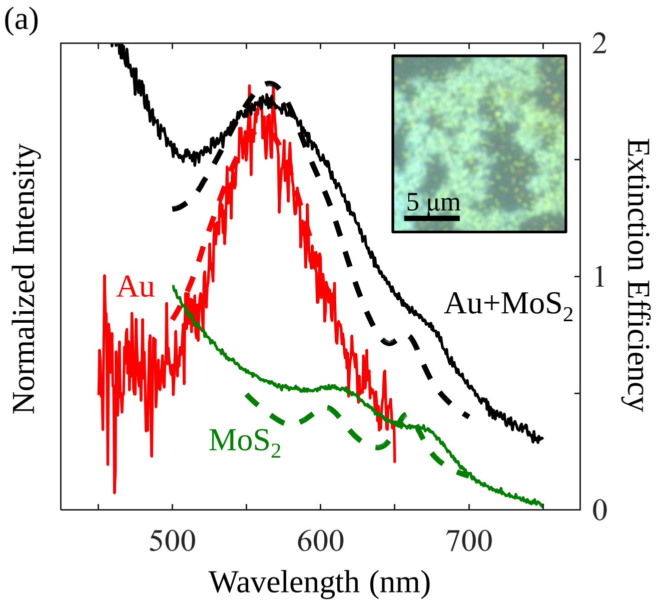

(b) 566 nm (c) 655 nm

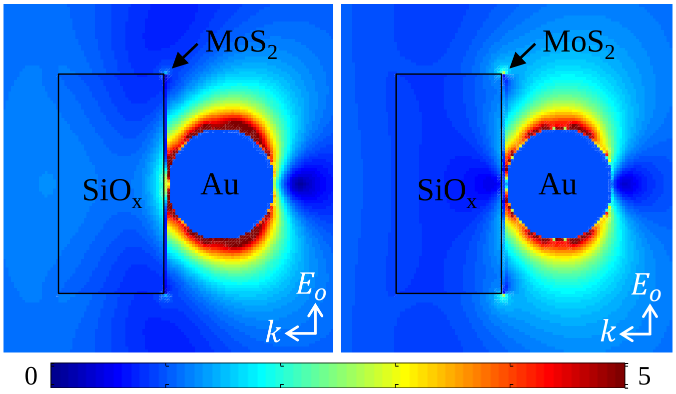

Figure 4.5: Optical response of Au nanosphere-decorated monolayer MoS_2. (a) Optical extinction spectra measured by transmission UV-vis spectroscopy (solid) and calculated by the DDA (dashed) for a 76 nm diameter Au nanosphere (red), monolayer MoS_2 (green), and 76 nm Au nanosphere-decorated MoS_2 (black). Inset shows representative optical bright-field image taken at 100x objective magnification. Enhanced electric near-field plots at (b) 566 nm and (c) 655 nm represent nanoantenna LSPR and monolayer MoS_2 A exciton, respectively. Field within the Au nanosphere was set equal to 1.

Optical extinction spectra for the Au nanosphere-MoS_2 heterostructure calculated by the DDA were consistent with the measured spectra.[230] Predicted LSPR and A exciton resonances of the heterostructure at 566 nm and 657 nm (1.89 eV) were within 1% and 2%, respectively, of their measured wavelengths. A 556 nm LSPR was reported previously for a 60 nm Au nanosphere on monolayer MoS_2 under electron excitation.[58] The A exciton transition blue-shifted by 4 nm (0.01 eV) to 655 nm (1.89 eV) relative to the MoS_2 monolayer control, consistent with reported PL spectra of MoS_2 after addition of Au nanoshells.[219] Absorption enhancements of the A and/or B exciton transitions were not evident, e.g., the LSPR overlaid the B exciton and prevented further analysis. FDTD simulations of 150 nm AuNS on MoS_2 suggest little far-field absorption enhancement of exciton features by surface plasmons.[236] The A and B bandgaps were simulated to occur ca. 30 meV higher than measurements, attributable to differences between the liquid-exfoliated MoS_2 used herein versus CVD-grown MoS_2 employed as the basis for dielectric data incorporated into the DDA.[217] Previous reports for A exciton energy for CVD-grown monolayer MoS_2 span a 60 meV range from 1.82-1.88 eV,[187,202,217,238] likely due to contaminants accrued from preparation/handling protocols.[239]

Excitation of different resonant modes of the Au nanosphere-MoS_2 heterostructure, specifically the LSPR and A exciton, and their unique energy localization characteristics were captured in electric near-field enhancement maps of Figure 4.5(b) and 4.5(c).[230] Excitation of the 566 nm LSPR exhibited electric field enhancement within the MoS_2 monolayer from the plasmonically-excited Au nanosphere. Enhancement magnitude decreased laterally away from their contact point. Concomitantly, the LSPR bandwidth in Figure 4.5(a) expanded ca. 15%. This suggested accrued plasmon damping from the MoS_2 was represented in the near-field map, possibly through radiative scattering and/or nonradiative transport of plasmonic hot electrons.[16,22,240] Electron injection from metal nanocubes into semiconductors was recently inferred from electron-excitation DDA.[241] Imaginary component of dielectric functions empirically represent total Drude damping comprising electron-electron scattering, electron-phonon scattering, and scattering by crystalline defects.[110] However, whether the classical DDA could represent quantum-mechanical changes in electron mass between two distinct materials over time remained uncertain. An experimental estimate of possible plasmonic hot electron transport was not made because of the intrinsic LSPR bandwidth expansion arising from variation in Au nanosphere diameters.[242]

Direct bandgap excitation across the A transition was represented as a ca. 1.5 electric field enhancement factor within the MoS_2 monolayer, shown in Figure 4.5(c). Little to no energy transfer was apparent from the semiconducting MoS_2 to the insulative SiO_x or conductive Au. A dipole was formed across the nanosphere, but was not a LSPR. Electrostatic charge polarization in response to the incident plane wave formed the dipole to satisfy Coulomb's law.[31]

Agreement between the DDA and experimental data was verified independently against measured photocurrent by Lin *et al*. for a four-layer MoS_2 field-effect transistor decorated with 15 nm Au nanospheres,[57] shown in Figure 4.6. A DDA target consisting of a single 16 nm Au nanosphere supported by four stacked layers of monolayer MoS_2 on top of a SiO_2 substrate in an effective refractive index of 1.35 (to account for citrate coating) was constructed based on the description of Lin *et al.* in Ref. 57. Although the given dielectric function for MoS_2 was based on a monolayer, the difference between the A and B exciton energies of a single- versus four-layer differ by less than 10 meV.[42] Reported spectral photocurrent maxima at 540, 600, and 660 nm were attributable to LSPR, B exciton, and A exciton resonances using DDA. The 540 nm photocurrent maxima had been inferred by Lin *et al*. to result from plasmonic activity based on a 517 nm LSPR measured from a liquid suspension of the Au nanospheres in a cuvette.

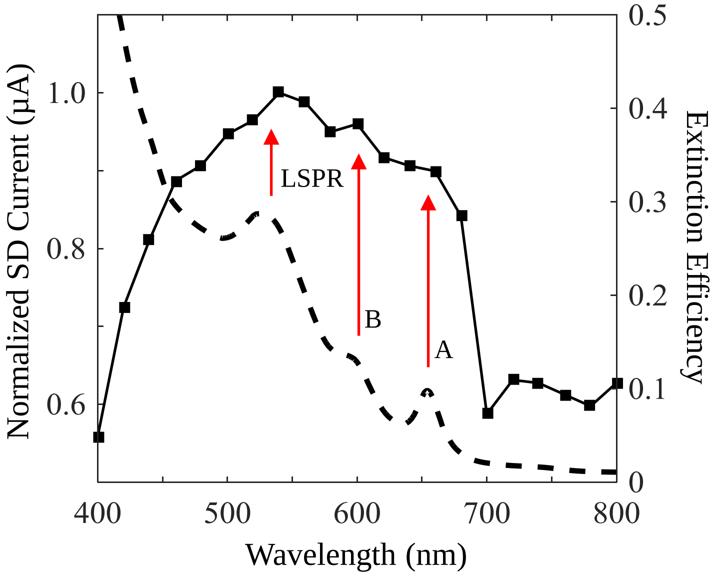

Figure 4.6: Measured source-drain (SD) photocurrent (squares) from 400 nm – 800 nm irradiation of a four-layer MoS_2 field-effect transistor decorated with 15 nm diameter Au nanospheres from Lin *et al*. in Ref. 57. Optical extinction efficiency spectra generated from the DDA is superposed (dashed). LSPR and A/B exciton features are labeled.

4.4 Interfacing with Silver Nanoprisms

Interfacing MoS_2 with 53±19 nm Ag nanoprisms resulted in an 87 nm LSPR red-shift, due to MoS_2 screening, to an energy beneath the A and B exciton transitions whose absorptions appeared enhanced.[230] In contrast to the Au nanospheres, the Ag nanoprisms featured (i) more surface area contact with MoS_2, (ii) lower energy LSPR, and (iii) multiple bright surface plasmon modes. Figure 4.7(a) shows measured (solid, LHS axis) and calculated (dashed, RHS axis) optical extinction spectra for a 53 nm edge length Ag nanoprism on monolayer MoS_2 atop a SiO_x substrate (black data). Maxima corresponding to orientation-averaged nanoprism LSPR was observed at 774 nm. The A and B excitons were not apparent because of the higher intensity LSPR. For comparison, optical extinction spectra are also shown for independently deposited Ag nanoprisms (red) and MoS_2 (green). All spectral features were observed in triplicate or greater in multiple areas of each sample to verify reproducibility.

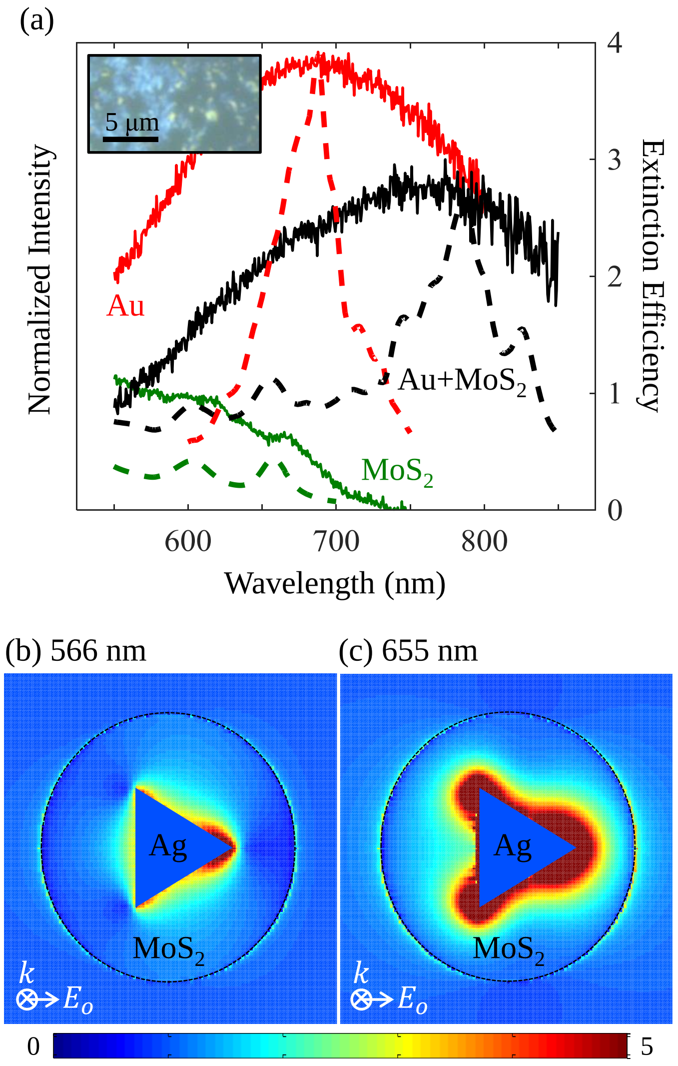

Figure 4.7: Optical response of Ag nanoprism-decorated monolayer MoS_2. (a) Optical extinction spectra measured by transmission UV-vis spectroscopy (solid) and calculated by the DDA (dashed) for a 53 nm edge length Ag nanoprism (red), monolayer MoS_2 (green), and 53 nm Ag nanoprism-decorated MoS_2 (black). Inset shows representative optical bright-field image taken at 100x objective magnification with 5 µm scale. Enhanced electric near-field plots at (b) 655 nm and (c) 788 nm represent monolayer MoS_2 A exciton and nanoantenna LSPR, respectively. Field within the Ag nanoprism was set equal to 1.

Optical extinction spectra for the Ag nanoprism-MoS_2 heterostructure calculated by the DDA were consistent with the measured spectra, albeit with evident exciton transitions and narrower LSPR bandwidth.[230] Calculated spectra were averaged over 0˚ and 90˚ polarizations to reflect their random orientation following deposition.[97] Predicted LSPR, A exciton, and B exciton features of the heterostructure at 788 nm, 655 nm (1.89 eV), and 603 nm (2.06 eV) were within 2% of their measured wavelengths. Extinction intensity of the A exciton was enhanced by 20% after introduction of the Ag nanoprism. As described in § 4.3, the A and B bandgaps were simulated ca. 30 meV higher than measurements, attributable to differences between the liquid-exfoliated MoS_2 used herein versus CVD-grown MoS_2 used to obtain the dielectric function.[217]

Measured LSPR bandwidth was much wider than the simulated bandwidth because of large variation in Ag nanoprism sizes versus the single size considered in the DDA. Optical averaging of LSPR unique to each Ag nanoprism size/geometry comprising the ±35% size distribution (i.e., edge lengths, equilaterally, vertex truncations) contributed to the bandwidth difference. Impacts of triangle edge length and vertex truncation on LSPR of nanoprisms has been detailed elsewhere.[97,233,243] For example, it has been shown that a 10 nm vertex truncation can blue-shift the LSPR of a nanoprism by almost 200 nm.[97] Notwithstanding this anticipated variance, the DDA accurately calculated the central resonant wavelength using mean edge length.

Excitation of the dominant LSPR and A exciton modes of the Ag nanoprism-MoS_2 heterostructure and their unique energy localization characteristics were captured in electric near-field enhancement maps of Figure 4.7(b) and 4.7(c) taken at the Ag-MoS_2 interface.[230] Direct bandgap excitation across the 655 nm (1.89 eV) A transition was represented as a ca. 1.5 electric field enhancement factor throughout the MoS_2 monolayer, shown in Figure 4.7(b). A dipole was formed across the nanoprism, but was not a LSPR. Again, electrostatic charge polarization in response to the incident plane wave formed the dipole to satisfy Coulomb's law.[31] The B exciton was not examined despite its prevalence in the spectra.

Excitation of the 788 nm LSPR indicated a dipolar profile, matching other reports, with apparent electric field enhancement within the MoS_2 monolayer. Concomitantly, the LSPR bandwidth in Figure 4.7(a) expanded ca. 19%. This suggested accrued plasmon damping from the MoS_2 was represented in the near-field map, possibly by radiative scattering and/or nonradiative transport of plasmonic hot electrons.[16,22,240] Larger bandwidth expansion for the Ag nanoprisms versus the Au nanospheres was consistent with the increased surface area contact (i.e., more interaction with the MoS_2). Similar results were found using solely 0˚ or 90˚ polarization, showing Γ expansion was consistent independent of plasmon mode type. Related FDTD simulations report the LSPR electric field enhancement factor of Ag nanodisc-MoS_2 heterostructure corresponded directly with its measured PL enhancement factor.[244] Again, experimental estimate of plasmonic hot electron transport quantum efficiency was not made because of intrinsic LSPR bandwidth expansion from wide variation in nanoprism sizes/geometries.[242]

4.5 Summary

Transmission UV-vis spectroscopy and DDA were used in parallel to characterize the origin of and interactions between resonances in heterostructures of monolayer MoS_2 and Au/Ag nanoantennas. Top-down drop-casting and bottom-up *in situ* synthesis of metal-TMD heterostructures was described. The DDA was introduced as a compact electrodynamic model to describe the linear optoelectronic interactions in metal-TMD heterostructures. Agreement was benchmarked within 2% against experimental transmission UV-vis extinction spectra. Calculated optical extinction spectra revealed (i) LSPR of nanospheres and nanoprisms modulated by MoS_2

screening and (ii) MoS_2 exciton transitions whose absorption were enhanced, depending on proximity to the nanoantenna LSPR. Energy localization and transport between the nanoantennas and MoS_2 was represented in electric near-field plots. Overall, the DDA was introduced as a guiding model to optimize fabrication and electrodynamic description of nanoantenna-decorated TMD monolayers for optoelectronic implementations.

CHAPTER 5

ENERGY CONVERSION BY PLASMONIC HOT ELECTRON TRANSPORT

Interfacing two-dimensional (2D) transition metal dichalcogenides (TMD) with plasmonic nanoantennas was hypothesized to introduce an intrinsic energy conversion mechanism: plasmonic hot electron transport.[245] Energy of localized surface plasmons are transduced through radiative photon scattering into the environment or nonradiative Landau damping into hot electron-hole pairs in the nanoantenna. Following Landau damping, plasmonic hot electrons traditionally decay via (i) phonon scattering into the crystal lattice or (ii) interfacial losses.[17–21] Contact between nanoantennas and a semiconductive TMD potentiate an additional damping pathway for plasmonic hot electrons via transport into the TMD, provided their energy exceeds the metal-TMD Schottky barrier.[16,22,23] Plasmonic hot electron transport into 2D materials has been inferred in catalysis[30,58,223] and photodetection schemes.[29,57,219,220,246] This chapter examined augmented plasmonic damping in metal nanoantenna-TMD heterostructures attributable to transport of plasmonic hot electrons into the TMD.

5.1 Electron Energy Loss Spectroscopy

Electron energy loss spectroscopy (EELS) identifies where and how energy is transduced to a plasmonic nanoantenna through excitation of resonant eigenstates.[247] Swift electrons in the nanometer probe of a scanning transmission electron microscope (STEM) lose energy according to resonant eigenstates of a nanoantenna, e.g., surface plasmon resonance. Inelastically transmitted electrons are dispersed by a magnetic prism according to their kinetic energy and loss intensity is quantified by a CCD detector.[248] This metrology, which analyzes the energy distribution of transmitted electrons, is referred to as the “GIF” and is shown in Figure 5.1. Reviews by Egerton, Garcia de Abajo, and Kociak provide comprehensive discussions of EELS.[91,145,248]

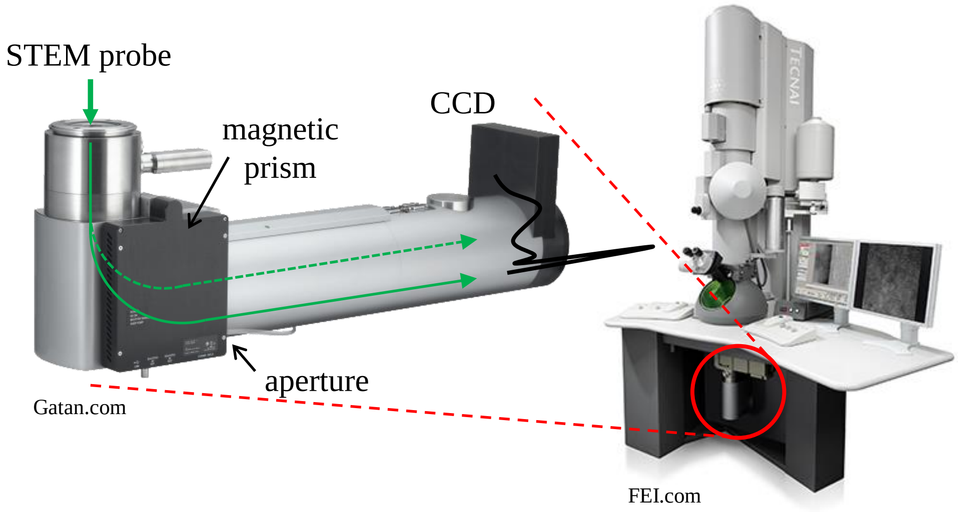

Figure 5.1: Schematic of EELS metrology in a GIF-outfitted STEM. A magnetic prism disperses the electron beam (green) according to energy losses were quantified by the CCD to give an EELS spectrum (black).

EELS spectra is comprised of three distinct regions: (i) the zero-loss peak (ZLP), (ii) the low-loss region, and (iii) the high-loss region.[248] The ZLP feature represents the natural energy spread of the STEM probe and defined the energy resolution of an EELS spectra according to its full width at half maximum (FWHM). The low-loss region quantifies energy loss to valence band interactions, e.g., localized surface plasmon resonance (LSPR) or bandgap excitation. The high-loss region quantifies inner-shell interactions, e.g., ionization edges, to fingerprint different elemental compounds. Low-loss eigenstates less than ca. 3 eV are obfuscated by breadth of the ZLP and require empirical background subtraction algorithms to deconvolute the eigenstate. Typical ZLP background models for subtraction include power-law, log-law, reflected-tail, polynomial, and Lorentzian ZLP fits[150,248] or Richardson-Lucy deconvolution.[249]

EELS allows qualitative insights into the electromagnetic local density of states (ELDOS).[144] Quantitative correlation between EELS and the ELDOS is precluded by differences in the electric-field distributions of a photon versus a swift electron.[135,145] Electric resonance mode types may be spatially distinguished in EELS maps, which correlate loss to particular locales on a nanoantenna. EELS maps are generated by rastering the STEM probe across a nanoantenna whilst recording EELS spectra at discrete intervals.[137–139,141,151,250] Resonances in EELS may be correlated to "bright" optical resonances using modal decomposition.[143] However, EELS was unique in that it may also excite "dark" plasmon resonances which cannot be directly accessed by optical methods. Dark resonances exhibit net a zero dipole moment (i.e., $\sum \vec{p} = 0$) whereas bright modes, such as the LSPR, exhibit a finite dipole moment ($\sum \vec{p} \neq 0$).[94]

EELS was performed herein on a FEI Tecnai G^2 F-20 (FEI, Hillsboro, OR USA) outfitted with a GATAN post-column imaging filter (GIF Quantum 963; GATAN, Pleasanton, CA USA). Energy resolution, as defined by the ZLP FWHM, was approximately 0.55 eV. Energy binning of the GIF was 50 meV. Spatial resolution, as defined by the electron beam diameter, was measured to be 2-3 nm. EELS acquisition conditions were optimized for each experiment according to its unique circumstances, e.g., relative strength of LSPR activity or electron-optic alignment of the STEM column. Generally, EELS spectra were taken at 120-200 kV accelerating voltage and summed from 50-100 distinct 10-200 ms acquisitions, followed by subtraction of the CCD dark current[251] and ZLP removal using power- or log-law fit.

5.2 Plasmon Bandwidth Analysis of Damping Mechanisms

Total bandwidth of a surface plasmon resonance contains signatures regarding the rate and quantum efficiency of its damping mechanisms. Total bandwidth, Γ, was comprised of summative contributions of each i^{th} damping mechanism, Γ_i, *viz*.[240,242]

$$\Gamma = \sum_i \Gamma_i = \Gamma_r + \Gamma_{nr} + \Gamma_c \ . \qquad \text{(Equation 5.1)}$$

Subscript r denotes a radiative contribution, nr denotes nonradiative contributions, and c identifies a putative carrier injection contribution arising from nanoantenna contact with TMD. There is correlation between Γ and the Drude damping rate (denoted γ in Equation 2.8). In the absence of elastic dephasing,[18,242] quantum efficiency, η_i, of the i^{th} damping pathway may be calculated according to Γ_i by Equation 5.2.[240]

$$\eta_i = \frac{\Gamma_i}{\Gamma} \qquad \text{(Equation 5.2)}$$

Bandwidth analysis was performed on surface plasmon resonances induced in EELS to quantify η_c and timescale of possible plasmonic transduction into injected hot electrons from nanoantennas into TMD. The nanometer STEM probe in EELS avoided (i) direct excitation of carriers in the TMD and (ii) diffraction-limited excitation of many nanoantenna, which convoluted similar studies using exciton binding energy shifts,[252] transient absorption spectroscopy,[223,253] and photoluminescence (PL).[242] Previously, LSPR Γ measured in EELS and PL spectroscopy were decomposed using Equation 5.1 to estimate 10% and 20% η_c in gold (Au) nanoantenna-graphene heterostructures.[242,240] Herein, a putative Γ_c contribution to plasmon damping was elucidated by measuring mean Γ for multiple nanoantennas with the appropriate negative control, i.e., $\Gamma_r + \Gamma_{nr}$ versus $\Gamma_r + \Gamma_{nr} + \Gamma_c$. This analysis assumed transport of Landau-damped hot electrons away from the nanoantenna did not redistribute prevalence of other nonradiative mechanisms.

Wien-type monochromation of the STEM probe's Gaussian energy distribution by the GIF convoluts the underlying Lorentzian Γ of the surface plasmon resonance to a measured Voight profile. In other words, measured Voight Γ in EELS is a convolution of the Lorentzian plasmon resonance with the Gaussian ZLP profile. The Lorentzian FWHM may be *a priori* converted to its observable Voight FWHM in EELS, and vice versa, using an empirical relation developed by Olivero and Longbothum with an accuracy of ±0.02%,[254] *viz*.

$$\Gamma_V = 05346\Gamma_L + \sqrt{0.2166{\Gamma_L}^2 + {\Gamma_G}^2} \qquad \text{(Equation 5.3)}$$

where Γ_V, Γ_L, Γ_G are the Voight, Lorentzian, and Gaussian bandwidths, respectively. In this work, Γ_V was the measured FWHM of a plasmon resonance in EELS and Γ_G was the 0.55 eV ZLP FWHM. Ascertaining changes to plasmonic Γ less than 0.55 eV by emergence of additional damping mechanisms remained possible through this relation, despite definition of the ZLP as the ultimate energy resolution of the system.

Plasmon dephasing times bound by Heisenberg's uncertainty principle may be calculated for damping mechanism i according to its Γ_i, *viz*.[18,240]

$$T_{2,i} = \frac{2\hbar}{\Gamma_i} \ . \qquad \text{(Equation 5.4)}$$

Static and dynamic charge transport processes with plasmon hot electrons, as defined by interfacial damping contributions in nonradiative dephasing,[21] differ from hot electron injection. Static charge transfer represents entrapment of hot carriers into trap states near the Fermi level. Dynamic charge transfer involves carriers returning to the nanoantenna and depolarizing coherence of the dipole oscillation, thereby shortening overall surface plasmon lifetime.

To distinguish contributions from Γ_r and Γ_{nr} to the measured Voight Γ, theoretical Lorentzian FWHM were estimated *a priori* using two numerical approaches based on the discrete dipole approximation (DDA) and convoluted with a 0.55-0.60 eV FWHM Gaussian.[247,254] Electron-excitation DDA package eDDA v1.2[104] and light-excitation DDA package DDSCAT v7.3[100,102,103] were used. Complex TMD and SiO_2 dielectric functions were used.[214,217,255] For DDSCAT, scattering (absorption) cross section was normalized against extinction cross section at resonance to calculate Γ_r (Γ_{nr}) after multiplying by the extinction FWHM. Results for DDSCAT were taken at a refractive index for which LSPR matched transmission UV-vis extinction measurements, due to its light excitation treatment. Corresponding estimates based on analytical Mie theory,[64] semi-analytical quasistatic and modified long wavelength approximate dipole polarizability,[97] and an empirical relation based on geometry[18] were also considered.

5.3 Gold Nanospheres on Molybdenum Disulfide

Heterostructures of Au nanospheres and molybdenum disulfide (MoS_2) were interrogated using EELS to quantify the probable extent of energy conversion into plasmonic hot electrons. Heterostructures were fabricated by sequential drop-casting of liquid-exfoliated MoS_2 (60-370 nm length; 1-2 layers; ethanol solvent) and Au nanospheres (76±13 nm; isopropanol solvent) onto a 20 nm silicon dioxide (SiO_2) membrane,[218] as described in § 4.1.1. Use of liquid-exfoliated MoS_2 avoided (i) atomic-scale defects (e.g., ripples[256] or lattice strains[54]) accrued from transferring synthetic TMD to the delicate membrane and (ii) thickness polydispersity of mechanically exfoliated TMD. Monolayer MoS_2 crystals were distinguished according to plasmon signatures at ca. 18-20 eV (bulk plasmon)[257] and 6 eV (π^* plasmon) that were red-shifted and less intense versus their few-layer MoS_2 counterparts.[176,218] A 200 kV STEM probe was placed at the edge (center) of the Au nanospheres to induce a bright (dark) surface plasmons, akin to the nanodisc simulations of Figure 2.6. FWHM of the bright and dark plasmon excitations in the presence and absence of MoS_2 were analyzed by Equation 5.1 to deduce a possible Γ_c contribution to damping.

5.3.1 Plasmonic Mode Structure

EELS analysis of five Au nanospheres in the absence of MoS_2 revealed two resonant plasmon modes: the bright LSPR at ca. 2.11 eV and a dark mode at ca. 2.03 eV.[150,218] Figure 5.2(a) shows representative EELS spectra obtained from edge (red) and center (blue) excitation of ca. 80 nm diameter Au nanospheres in the absence (hollow data points) and presence (filled data points) of underlying MoS_2. Bright and dark modes are labeled "B" and "D," respectively. Figure 5.2(b) and 5.2(c) show the corresponding high-angle annular dark-field (HAADF) STEM images with labeled impact points. Monolayer MoS_2 appeared dark-gray in STEM mode relative to Au because of its low electron-scattering cross section, inherent to an atomically-thin crystal. Screening by ca. 10 nm poly(vinylpyrrolidone) (PVP) ligands encapsulating the Au nanosphere may have red-shifted the dark mode from the 2.45 eV bulk plasma energy anticipated for nanoantennas of this size.[94] A 2.4 eV eigenstate was simulated by eDDA for edge excitation, both in the presence and absence of MoS_2; however, the PVP was not included.

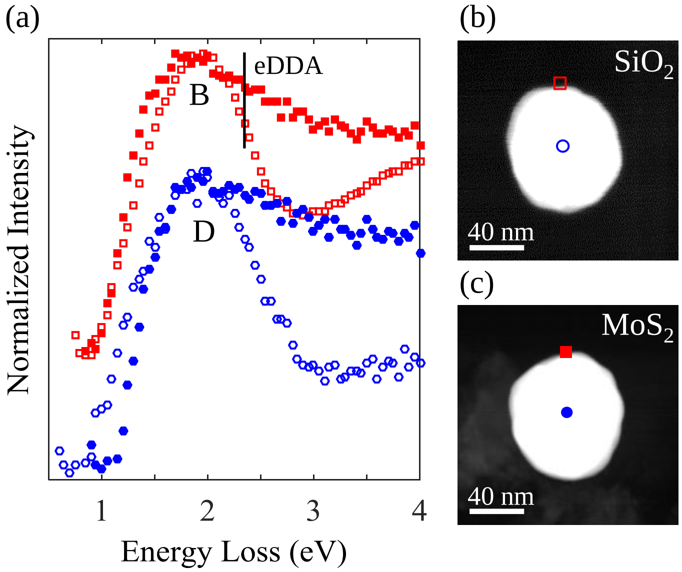

Figure 5.2: (a) EELS spectra from edge (red) and center (blue) impact of a ca. 80 nm Au nanosphere with (filled) and without (hollow) an underlying MoS_2 monolayer. Corresponding HAADF-STEM images are shown in (b) and (c). Spectra were normalized and vertically offset for clarity. Accelerating voltage was 200 kV. Black solid line shows surface plasmon energy simulated using eDDA for edge excitation both with and without MoS_2 (same energy resulted).

Presence of a MoS_2 monolayer beneath the Au nanosphere expanded FWHM of the bright LSPR by ca. 0.08 eV averaged across five measurements, ostensibly due to emergence of additional plasmon damping pathway(s).[22,240,242] Energies of the bright and dark both modes (ca. 2.15 eV and 2.09 eV, respectively) remained essentially unchanged. Graphene also did not significantly change resonant plasmon energies of a Au nanoellipse in a previous report.[240] In another report, MoS_2 red-shifted the bright plasmon resonance of 60 nm silver nanodiscs by 36 meV,[258] which was less than the binning resolution of the GIF. The dark mode FWHM remained unchanged. Reported 10 meV red-shift in A exciton energy for MoS_2 from n-type doping was also beneath resolution of the GIF.[252] eDDA computed a 0.03 eV bandwidth expansion for the bright mode by comparison (data not shown). EELS spectral profiles for Au nanospheres with MoS_2, such as those shown in Figure 2(a), were similar to those without MoS_2, but with more intense 2-4 eV energy loss. This appeared due to absorption in MoS_2 above its 1.85 eV direct bandgap.[42]

Table 5.1 summarizes mean energy occurrence and FWHM for bright and dark plasmonic resonances measured in EELS on ten ca. 80 nm Au nanospheres; five without and five with underlying MoS_2. Presence of the MoS_2 altered resonant energy of the bright (dark) mode from 2.11 eV (2.03 eV) to 2.15 eV (2.09 eV), albeit shifts were statistically insignificant. Welch's t-test confirmed statistical significance of the ca. 0.08 eV FWHM expansion for the bright LSPR with 95% confidence. FWHM change for the dark plasmon mode was insignificant. Thus, putative hot electron transport from the Au nanosphere to the MoS_2 appeared unique to bright plasmonic excitation, consistent with graphene-based heterostructures.[240] Carrier injection into the electrically insulative SiO_2 membrane was neglected as in previous studies.[242,259]

Table 5.1: Mean EELS-measured energy and FWHM for bright and dark plasmonic resonances for ca. 80 nm Au nanospheres (AuNS) with and without an underlying MoS_2 monolayer.

	Diameter [nm]	**Energy [eV]**		**FWHM, Γ [eV]**	
		Bright	**Dark**	**Bright**	**Dark**
AuNS	79±2	2.11±0.01	2.03±0.02	1.28±0.01	1.32±0.02
AuNS-MoS_2	78±2	2.15±0.01	2.09±0.02	1.36±0.02	1.30±0.02

5.3.2 Bandwidth Analysis

Bright surface plasmon resonance energy of ca. 2.1 eV exceeded the 0.9 eV Schottky barrier of Au-MoS_2 interfaces,[194] thus potentiating a finite Γ_c contribution to overall plasmon damping. A corresponding energy band diagram is shown in Figure 5.3.[218] Landau damping of the plasmon resonance created hot electrons[22] one plasmon quanta of ca. 2.1 eV (measured in EELS) above the Fermi level, E_F, and potentiated transfer into the MoS_2 conduction band, E_c. Transfer of these plasmonic hot electrons across the Au-MoS_2 Schottky barrier was measured herein according to a concomitant increase in overall Γ, attributable to emergence of Γ_c. Table 5.2 summarizes measured and simulated bright LSPR Voight Γ, along with its known Γ_r and Γ_{nr} contributions in the absence of MoS_2, to distinguish a possible Γ_c contribution for the Au nanosphere-MoS_2 heterostructure.

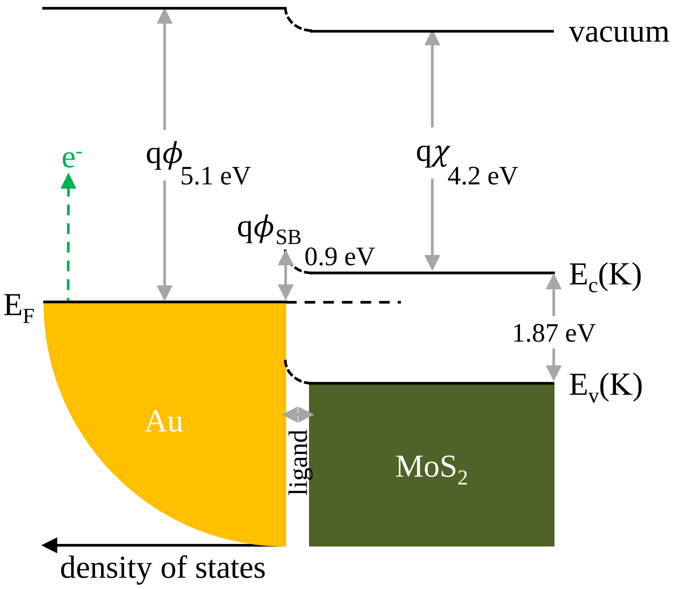

Figure 5.3: Energy band diagram of a Au-MoS_2 junction at thermal equilibrium. Resonant excitation at 2.1 eV of the Au nanosphere exceeded the 0.9 eV Schottky barrier ($q\phi_{SB}$), calculated from the Au work function ($q\phi$) of Au and MoS_2 electron affinity ($q\chi$), and potentiated transport of hot electrons into the MoS_2 conduction band (E_c). Possible quantum confinement effects and finite Au ligand thickness were neglected for simplicity.

Table 5.2: Plasmonic damping of the bright LSPR for ca. 80 nm Au nanospheres (AuNS) with and without an underlying MoS_2 monolayer. Resonant plasmon FWHM, Γ, were calculated using electron- and light-excitation DDA models, labeled eDDA and DDSCAT, respectively.

	Method	**Diameter [nm]**	**Radiative, Γ_r [eV]**	**Nonradiative, Γ_{nr} [eV]**	**Total, Γ [eV]**
AuNS	eDDA†	80	-	-	0.87
	DDSCAT†		0.31	0.57	0.88
	measured‡	79±2	-	-	1.28±0.01
AuNS-MoS_2	eDDA†	78	-	-	0.90
	DDSCAT†		0.35*	0.57	0.92
	measured‡	78±2	-	-	1.36±0.02

† after convolution with 0.60 eV Gaussian ZLP
‡ included PVP
* assumed contribution from MoS_2 to Γ (i.e., 0.88 eV - 0.83 eV) was attributable to Γ_r

In the absence of MoS_2 (i.e., $\Gamma_c = 0$), measured resonant bandwidth of the Au nanospheres on SiO_2 was Γ = 1.28±0.01 eV.[218] Estimates for $\Gamma_r + \Gamma_{nr}$ of 0.87 eV and 0.88 eV were obtained using eDDA and DDSCAT, respectively. Photon and phonon scattering contributed 36% and 64%, respectively, to total damping according to DDSCAT. Measured Γ was 0.41±0.01 eV larger than eDDA simulated Γ, apparently due to concomitant influences of (i) drift in ZLP energy alignment on the GIF over 100 acquisitions, (ii) ZLP background subtraction bias, and/or (iii) interfacial damping by physisorbed PVP on the Au surface.[19,21]

Measured plasmonic FWHM of the Au nanospheres expanded to Γ = 1.36±0.02 eV in the presence of underlying MoS_2.[218] This indicated Γ_c = 0.05±0.03 eV, after 0.87 eV for $\Gamma_r + \Gamma_{nr}$ for the Au nanosphere on SiO_2 (from eDDA), 0.03 eV in accrued Γ_r from MoS_2 (from eDDA), and 0.41±0.01 eV (PVP interfacial effects and contributions intrinsic to EELS metrology and interpretation) from Γ using Equation 5.1. Bandwidth expansion in the DDA models was conservatively attributed to accrued Γ_r through TMD screening. Large Γ_{nr} can limit PL enhancement in MoS_2 from plasmons due to plasmon-phonon scattering transduced by the nanoantenna into the TMD.[225]

A putative η_c of up to 4±2% for transport of plasmonic hot electrons from the Au nanospheres to MoS_2 was conservatively estimated by Equation 5.2 using inferred $\Gamma_c = 0.05 \pm 0.03$ eV and measured $\Gamma = 1.36 \pm 0.02$ eV.[218] Corresponding n-type doping densities may be calculated from plasmon-induced changes to exciton binding energy of MoS_2,[252] but were not considered in this work. Possible interfacial damping from the MoS_2 underlying the residual 0.05 eV Γ expansion was assumed negligible because of the PVP interlayer. Plasmon-excited hot electrons ostensibly dephased into the MoS_2 over a 26±16 fs period, via Equation 5.4. This value fell within the 1-100 fs timescale reported for Landau damping of metallic plasmons.[16] A 200 fs timescale was recently measured by transient absorption spectroscopy for Au nanorods into MoS_2.[253] Lifetime of injected carriers in MoS_2 has been estimated to be 800 ps prior to radiative recombination.[223]

Relatively low conversion efficiency was likely due to the high resistance ohmic junction between the Au nanospheres and MoS_2. High resistance arose from (i) lack of direct physical Au-MoS_2 contact because of the PVP coating around Au and (ii) strict linear momentum conservation constraints. Dielectric spacers between the metal and TMD can mitigate, and even abolish,[260] quantum yield of injected carriers by increasing the resistance of the metal-TMD ohmic junction. Rough, polycrystalline metal interfaces ease electron momentum orientation requirements for transfer of plasmonic hot electrons into adjacent media.[23] Thus, direct physicochemical contact between a reduced nanoantenna and TMD crystal, i.e., an optimal ohmic contact with minimized resistance, was postulated to signify the ultimate extent to which energy could be converted towards plasmonic hot electron injection.

5.4 Effect of Ohmic Contact Quality on Plasmonic Hot Electron Transport

Plasmonic hot electron transport across an optimized Au-TMD ohmic contact, where ca. 20 nm Au nanoantennas (AuNA) were physicochemically bonded to the edges of mono- to few-layer liquid exfoliated tungsten disulfide (WS_2), was measured using EELS.[261] Formation of Au-sulfur bonds was confirmed by x-ray photoelectron spectroscopy (XPS), detailed in Refs. 229 and 261. Briefly, a secondary S2p doublet emerged upon WS_2 reaction with gold chloride ($AuCl_3$) of ca. 1 eV lower binding energy relative to the WS_2 S2p doublet, attributable to formation of Au-sulfur bonds.[262,263] AuNA-decorated WS_2 crystals were fabricated as described in § 4.1.2 and drop-cast onto a 20 nm thick SiO_2 membrane. In previous studies of plasmonic hot electron transport into 2D materials, the ohmic junction was limited to physical contact with the basal plane of the 2D material.[218,223,242,252] AuNA were physicochemically bonded onto the WS_2 edges in this work. Unique lattice terminations at 2D material edges provide extraordinary optical behavior from the basal plane,[180,187,237,264,265] which could be more receptive to plasmonic hot electrons.

A bright ca. 2.1 eV LSPR was measured by EELS for three ca. 20 nm AuNA in the absence of WS_2.[261] Attachment of three comparably sized AuNA to the edge of WS_2 expanded bright LSPR Γ by ca. 0.23 eV, ostensibly due to emergence of additional plasmon damping pathway(s) including hot electron transport.[22,218,242] Figure 5.4(a) shows representative EELS spectra obtained from ca. 20 nm AuNA with (filled data points) and without (hollow data points) attachment to a WS_2 edge, each atop SiO_2. Impact point of the 120 kV STEM probe was at the far edge of each AuNA opposite of the WS_2. This minimized any WS_2 interaction and prevented its losses from obfuscating the LSPR.[218] Figure 5.4(b) and 5.4(c) show HAADF-STEM images with labeled impact points. The *in situ* chemical reduction protocol secondarily resulted in WS_2-free AuNA, thought to originate from reduction by the sodium cholate surfactant used for suspension stability. These AuNA were used as the negative control data.

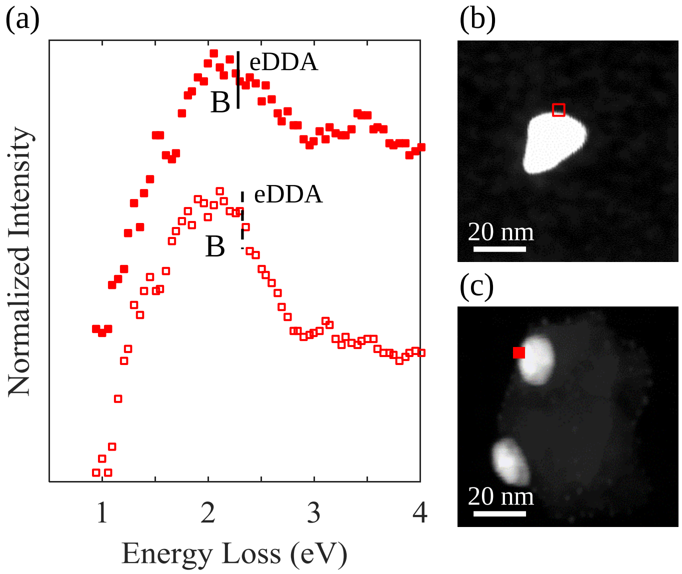

Figure 5.4: (a) EELS spectra from edge excitation of a ca. 20 nm AuNA isolated (hollow) or reduced (filled) onto the edge of a 2D WS_2 crystal. Corresponding HAADF-STEM images are shown in (b) and (c). Accelerating voltage was 120 kV. Spectra were normalized and vertically offset for clarity. Estimates for LSPR according to eDDA in the presence (solid vertical line) and absence (dashed vertical line) of WS_2 are superposed.

A 2.38 eV bright LSPR was anticipated by eDDA (vertical solid line) for a 20 nm Au sphere placed at the edge of a 90x45 nm WS_2 sheet, which signified a simplification of the measured heterostructures sans the SiO_2 membrane.[261] This was red-shifted 0.05 eV relative to the 2.43 eV LSPR in the absence of WS_2 (vertical dashed line). Experimental LSPR may have been red-shifted from the theory due to screening from the SiO_2 and/or quantum confinement.[150] Also, WS_2 edge states were could not be represented because of dielectric function treatment of the WS_2, as opposed to density functional theory models. Dark plasmon resonances inducible at the AuNA center[94] were not examined because damping by hot electron transfer was found to originate from the bright LSPR in § 5.3.1 and other reports.[218,240]

Table 5.3 summarizes mean energy occurrence and FWHM for the LSPR measured in EELS across six ca. 20 nm AuNA; three without and three with attachment to WS_2.[261] LSPR blue-shift from 2.08 eV to 2.15 eV upon interaction with WS_2 was statistically insignificant. Welch's t-test confirmed statistical significance of the ca. 0.23 eV FWHM expansion for the LSPR with 95% confidence. Accrued bandwidth was ostensibly due to ca. 2.1 eV hot electrons transported across the 0.6 eV Au-WS_2 $q\phi_{SB}$; the corresponding energy band diagram is shown in Figure 5.5.[261] However, $q\chi$ value[266] was taken from measurements of the WS_2 basal plane. Possible ELDOS alterations in its band structure associated with physicochemical Au reduction onto WS_2 edges with unique lattice terminations[231] were not considered due to absence of associated data. This $q\phi_{SB}$ was lower than the 0.9 eV Au-MoS_2 $q\phi_{SB}$ studied in § 5.3, and thus potentiated an instrinsically higher η_c.

Table 5.3: Mean EELS-measured energy and FWHM for bright LSPR for three ca. 20 nm AuNA with and without attachment to the edge of a WS_2 crystal.

	Measured Diameter [nm]	**LSPR [eV]**		**FWHM, Γ [eV]**	
		measured†	**eDDA**	**measured**†	**eDDA**‡
AuNA	22±5	2.08±0.04	2.43	1.38±0.05	0.82
AuNA-WS_2	19±4	2.15±0.08	2.38	1.61±0.03	0.86
† included 20 nm SiO_2 substrate and/or nearby AuNP ‡ after convolution with 0.55 eV Gaussian ZLP					

Reduction of AuNA onto the edge of WS_2 expanded the measured resonant bandwidth to Γ = 1.61±0.03 eV from 1.38±0.05 eV in the absence of WS_2. This conservatively indicated Γ_c = 0.19±0.08 eV, after subtracting 0.82 eV for $\Gamma_r + \Gamma_{nr}$ for the AuNA [from eDDA and supported by DDSCAT (data not shown for brevity)], 0.04 eV in in accrued Γ_r from WS_2 (from eDDA), 0.04 eV for SiO_2 interfacial losses,[218] and 0.52±0.05 eV (contribution intrinsic to EELS metrology and interpretation). A portion of the residual 0.19 eV expansion in Γ could result from entrapment of plasmonic hot electrons into WS_2 trap states and/or return of hot electrons back to the AuNA, thereby depolarizing its oscillation.[21] Role of Au-sulfur bonds in plasmon damping remains unclear. Covalent Au-sulfur bonds on organic thiol-coated AuNP notably expands Γ,[267] but crystalline WS_2 is fundamentally distinct from organic substitutents.

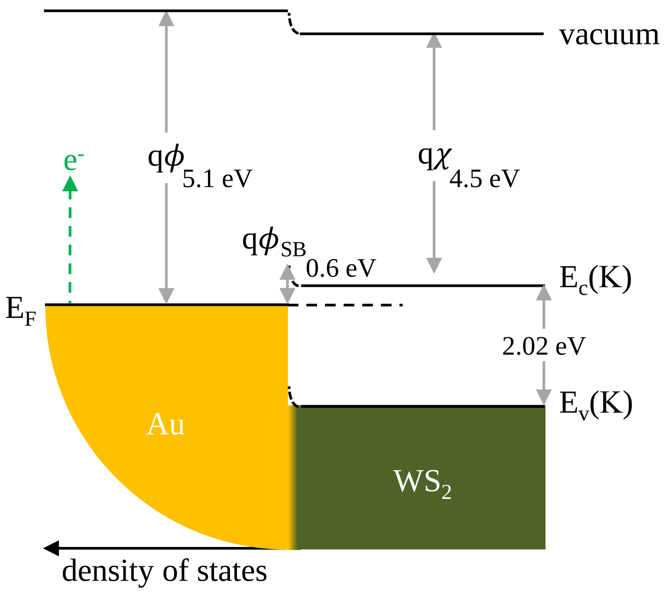

Figure 5.5: Energy band diagram of a Au-WS_2 junction at thermal equilibrium. Resonant excitation at 2.1 eV of the AuNA exceeded the 0.6 eV Schottky barrier ($q\phi_{SB}$), calculated from the Au work function ($q\phi$) of Au and WS_2 electron affinity ($q\chi$), and potentiated transport of hot electrons into the WS_2 conduction band (E_c). Possible quantum confinement effects were neglected for simplicity.

A putative η_c of up to 11±5% was conservatively estimated for putative transport of plasmonic hot electrons from AuNA to WS_2. Changing the relative proximities of STEM probe, AuNA, and WS_2 crystal edge could affect calculation or measurement of η_c due to increased optical activity at WS_2 edges.[180,231,237] Based on measured damping, estimated dephasing time for each Landau-damped plasmonic hot electron to ostensibly transfer into the WS_2 was 7±3 fs. This value was lower than previous estimates ranging from 26 to 200 fs for plasmonic hot electrons to transfer from Au nanospheres and nanorods *across a dielectric spacer* into MoS_2.[218,253] Improved contact quality (i.e., lower resistance) between the AuNA and WS_2 via covalent bonding, lower

Schottky barrier, and eased momentum conservation constraints[23] appeared to increase the transport damping rate.

5.5 Summary

Possible transport of plasmonic hot electrons from 80 nm Au nanospheres and ca. 20 nm AuNA to 2D TMD crystals was measured for the first time by comparing measured plasmonic bandwidth in EELS with those computed using DDA models. The nanometer STEM probe allowed single-particle resolution and avoided confounding effects associated with optical measurements, e.g., direct electron-hole pair generation in the TMD. A quantum yield of up to 4±2% for putative transport of plasmonic hot electrons was estimated for 80 nm Au nanospheres deposited onto MoS_2, albeit with a high resistance ohmic contact due to PVP ligands on the Au. Putative quantum yield of plasmonic hot electron transport increased to 11±5% for ca. 20 nm AuNA physicochemically bonded to WS_2, representing an optimized ohmic junction with minimized resistance and intrinsically lower $q\phi_{SB}$. Plasmonic damping through hot electron transport was found to originate solely from excitation of the bright LSPR. Dark plasmonic modes, whose measurement are unique to electron-excitation in EELS, were found not to contribute to transport of plasmonic hot electrons. Overall, the extent to which electromagnetic energy above the nanoantenna-TMD ϕ_{SB} could be passively converted into plasmonic hot electrons dissipated into TMD was conservatively measured to be 11%.

CHAPTER 6

SURFACE PLASMON-ENHANCED NONLINEAR ENERGY MIXING

Rejection and conversion of infrared energy through nonlinear frequency mixing phenomena[32,33] was tested with two-dimensional (2D) molybdenum disulfide (MoS_2)[42–44] interfaced with gold (Au) nanoshells. Monolayer MoS_2 was selected for its high susceptibility to second-order nonlinear interactions, $\chi^{(2)}$, measured at 660±130 pm V^{-1} at 532 nm.[207] Local electric field augmentation by the metal nanoshells was hypothesized to passively enhance nonlinear energy conversion from the MoS_2.[75,92,94] This chapter quantitatively examined second harmonic generation (SHG) from a MoS_2 monolayer within the electric field of localized surface plasmons using multi-photon confocal microscopy.

6.1 Multi-Photon Confocal Microscopy

Confocal microscopy is a laser-scanning, episcopic imaging technique which detects multi-photon emission (e.g., two-photon scattering for SHG) at improved x-y spatial resolution over conventional optical microscopes.[268,269] It accomplishes this via a pinhole aperture placed in front of the detector at the objective lens focus point to eliminate out-of-focus z-axis contributions. Figure 6.1 schemes the working-principle for a basic multi-photon confocal microscope via optical ray diagram. Detection metrology is comprised of a photomultiplier tube (PMT) array, where each PMT is dedicated to some band of wavelengths tailored by a sequence of dichroic mirrors. Laser-scanning nature of the technique allows hyperspectral image reconstruction, such that a unique scattering spectra may be accessed for each pixel within the confocal image.

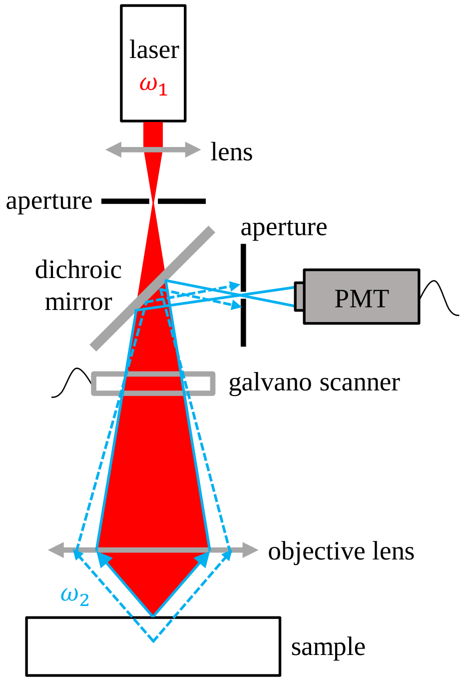

Figure 6.1: Schematic of a multi-photon confocal microscope. An excitation laser (ω_1; red) is focused onto a sample which emits higher frequency signals (ω_2; blue), where $\omega_1 < \omega_2$. In-focus scattered photons are detected by a PMT array. Out-of-focus contributions are blocked by a pinhole aperture.

The "z-scan" technique pioneered by Van Stryland *et al*. was an alternative method to explore the nonlinear optical properties of a material,[270,271] namely the nonlinear refractive index, n_2, and absorption coefficient, α_2. Briefly, the technique examines intensity-dependent transmission changes and phase distortions in a Gaussian laser beam as a nonlinear material is translated through its focus point; hence, its denotation as a z-scan. Changes in transmittance accrued from multi-photon absorption processes,[33] presumed to be dominated by two-photon absorption, enables quantitation of α_2. Intrinsic Kerr self-focusing of the laser within the nonlinear material accrue from $n_2 > 0$,[33] causing minute phase shifts observable in the far-field as changes in transmittance when a small aperture is placed in front of the detector. However, both n_2 and α_2 are third-order nonlinear processes associated with $\chi^{(3)}$.[32,33] This work focuses on $\chi^{(2)}$ frequency conversion. Despite its misleading nomenclature, two-photon absorption falls under third-order classification because: (i) direct dependence on $\Im(\chi^{(3)})$ and (ii) it is a cascaded linear absorption process not limited to non-centrosymmetric crystallinity (as with $\chi^{(2)}$ processes).[33]

SHG from monolayer MoS_2 in the presence and absence of nanoantennas was measured from an inverted, laser-scanning confocal microscope (A1R-MP; Nikon Instruments, Melville, NY USA) coupled to a unpolarized, wavelength tunable Ti:sapphire laser (MaiTai Deep See; Spectra-Physics, Santa Clara, CA USA). A 60x water-immersion objective (1.27 NA CFI Plan Apo IR; Nikon Instruments, Melville, NY USA) focused the rastering laser (100 fs pulse width; 80 MHz) onto the sample. Scattered photons were episcopically collected at 50 nm raster intervals (i.e., each pixel) and delivered to an array of 32 PMT at 2.5 nm wavelength binning. Excitation was limited to a 810-1000 nm spectrum herein because of detector incompatibility with sub-400 nm wavelengths. Data were captured at 1.1 μs of irradiation per pixel, gained by the PMT at 160 V, and averaged over 16 acquisitions to increase signal-to-noise ratio. Power of the laser was 5 mW (± 0.35 mW) across all excitation wavelengths. Diameter of the focused laser beam was ca. 0.8-1.0 μm, per the Abbe criterion.[272] Post-processing of hyperspectral images, including extraction of spectra from regions of interest (ROI), was performed in Nikon NIS-Elements Confocal (v4.3; Nikon Instruments, Melville, NY USA).

6.2 Heterostructure Prototype

Synthetic monolayer MoS_2, grown via chemical vapor deposition (CVD), interfaced with 150 nm Au nanoshells was used as a prototype for enhanced nonlinear infrared frequency conversion. Plasmon enhancement of nonlinear activity, both third- and second-order, has been examined in other nanomaterial heterostructures: ionic polymer bilayer films doped with silver nanospheres,[273] organic dyes with gold nanospheres,[274] barium titanate nanoparticles encapsulated in Au,[275] zinc oxide nanowires on a Au pentamer,[276] rubidium titanyl phosphate with silver nanoantennas,[277] and various instantiations of indium tin oxide (ITO) placed within a Au dimer.[278–280] Intensity of the SH was enhanced 60-1700x over the nonlinear source component, with one citing a 0.00003% conversion efficiency.[273,275–277] The prototype Au-MoS_2 heterostructure herein improves over aforementioned systems by (i) higher $\chi^{(2)}$ of 660 pm V^{-1} versus 6 pm V^{-1} for zinc oxide, 14 pm V^{-1} for the ionic polymer bilayers, 31 pm V^{-1} for rubidium titanyl phosphate, and 34 pm V^{-1} for barium titanate;[281–284] (ii) a polarization independent LSPR; and (iii) nanoantenna morphology amenable to high-volume chemical synthesis.

6.2.1 Fabrication

Figure 6.2(a) shows a scanning electron microscopy (SEM) image of single representative Au nanoshell-MoS_2 heterostructure. Au nanoshells 148±8 nm in overall diameter, with 119±9 nm silica (SiO_x) inner core and poly(vinylpyrrolidone) (PVP) ligand (lot MGM1774; nanoComposix, San Diego, CA USA),[285] were dispersed in water to a concentration of 3.6×10^9 mL^{-1}. These nanoshells were three-dimensional analogs to the 2D nanorings studied in § 2.4 to circumvent need for top-down lithography. An energy-filtered transmission electron microscopy (EFTEM) image of the Au nanoshells is shown in Figure 6.2(b). The Au nanoshells were drop-cast[228] (3 µL volume) onto MoS_2 grown via CVD on a silicon (Si) wafer with 300 nm of thermal oxide (CVD-MOS2; 2Dsemiconductors, Scottsdale, AZ USA) preheated to 105 ˚C. The MoS_2-Si wafer was pre-cleaned to improve hydrophilicity by sequential 3 min immersions into acetone, methanol, and isopropanol followed by a water rinse and dried under nitrogen gas. MoS_2 is a noted catalyst for methanol dissociation,[286] which caused apparent removal of some MoS_2 monolayers from the Si during the methanol immersion step. Nitric acid treatment, an alternative hydrophilic treatment used in § 4.1 for SiO_x, was observed to structurally degrade the MoS_2 (data not shown).

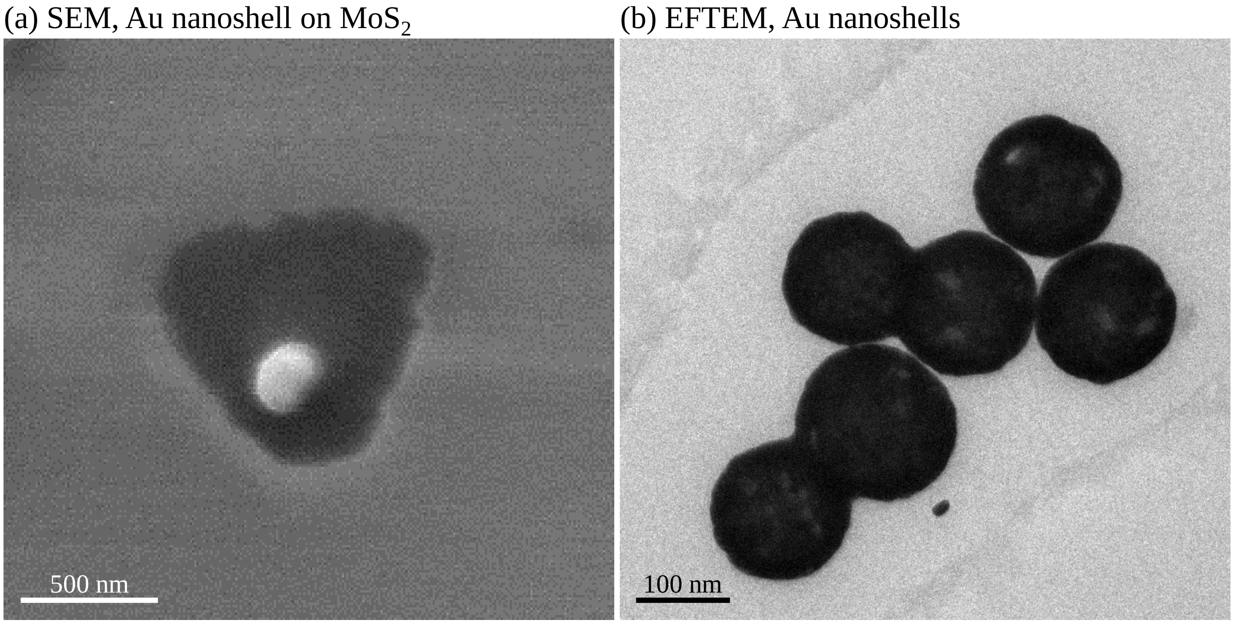

Figure 6.2: (a) SEM image of a representative heterostructure comprised of triangular monolayer of MoS_2 and a Au nanoshell. (b) EFTEM image of the Au nanoshells revealing SiO_x core. Accelerating voltages were 5 kV and 120 kV, respectively.

6.2.2 Nanoantenna Characterization

The Au nanoshells exhibited an *in vacuo* dark plasmon resonance at 1.60 eV and bonding-type bright LSPR at 1.89 eV, as measured in electron energy-loss spectroscopy (EELS) and shown in Figure 6.3(a).[287] An EELS map taken at the 1.89 eV resonance mode revealed loss characteristics indicative of a bright mode (discussed in § 2.4). High-angle annular dark-field (HAADF) scanning transmission electron microscopy (STEM) images of measured nanoantennas corresponding to each spectra are shown in Figure 6.3(b). Despite energy difference of the bright and dark modes falling beneath the 0.55 eV EELS energy resolution, the two apparent modes were not artifacts from zero-loss peak (ZLP) subtraction or other numerical processing. A comparison between one representative EELS spectra before and after ZLP subtraction is shown in Figure 6.3(c). Both modes were evident across measures of six distinct nanoantennas and power-law, log-law, reflected tail, and direct reference subtractions of the ZLP.

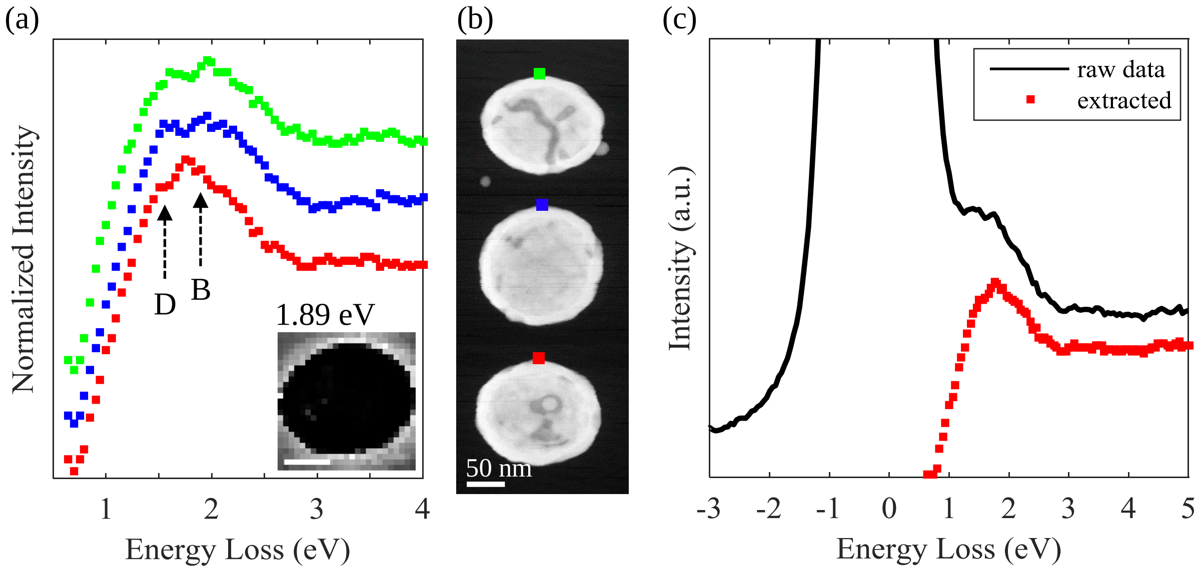

Figure 6.3: (a) EELS spectra from edge excitation of a three representative ca. 150 nm Au nanoshells (15 nm Au shell; 120 nm diameter SiO_x core) exhibiting 1.89 eV bright and 1.60 eV dark plasmonic resonances on average. Spectra were normalized and vertically offset for clarity. Inset to (a) is an EELS map taken at the 1.89 eV mode with 50 nm scale. (b) HAADF-STEM images with labeled impact points corresponding to each of the spectra. (c) Comparison between one EELS spectra with and without ZLP subtraction according to a $y = Ae^{-x} + B$ power-law fit. Accelerating voltage was 120 kV.

The *in vacuo* LSPR energy agreed well with 1.86-1.90 eV estimates from analytical Mie theory[64] and numerical discrete dipole approximation (DDA)[90,100,104] for a 150 nm diameter Au-SiO_x nanoantenna (15 nm Au shell; 120 nm diameter SiO_x core) atop a 20 nm thick silicon dioxide (SiO_2) membrane (data not shown for brevity).[287] Computationally placing a swift electron beam at the edge of the nanoshell (i.e., eDDA[104]) revealed a low energy shoulder from a dark mode. This was consistent with the experimental EELS spectra. However to date, only Au nanoshells at much larger aspect ratios (0.4 versus 0.2 herein) have been characterized using EELS and dark resonances were not considered,[157] which precluded a rigorous comparison with published reports.

The LSPR red-shifted to 1.52 eV (817 nm) upon immersion of the nanoshells into water, which fell within the 700-1000 nm excitation spectrum of the Ti:sapphire excitation laser coupled into the multi-photon confocal microscope outfitted with water-immersion objectives. Figure 6.4

compares experimental transmission UV-vis extinction spectra (solid) with those calculated by DDA (dashed) and Mie theory (dotted). Maximas at 625 nm and 817 nm corresponded to the quadrupole and dipole LSPR, respectively [dipole is plotted in Figure 6.4(b)]. Experimental data were taken from the nanoantennas suspended in water within a cuvette.[285] Experimental LSPR breadth reflects the size distribution. DDA and Mie data were taken at an effective refractive index of 1.40 to account for screening contributions from the PVP ligand (refractive index of 1.52).[106]

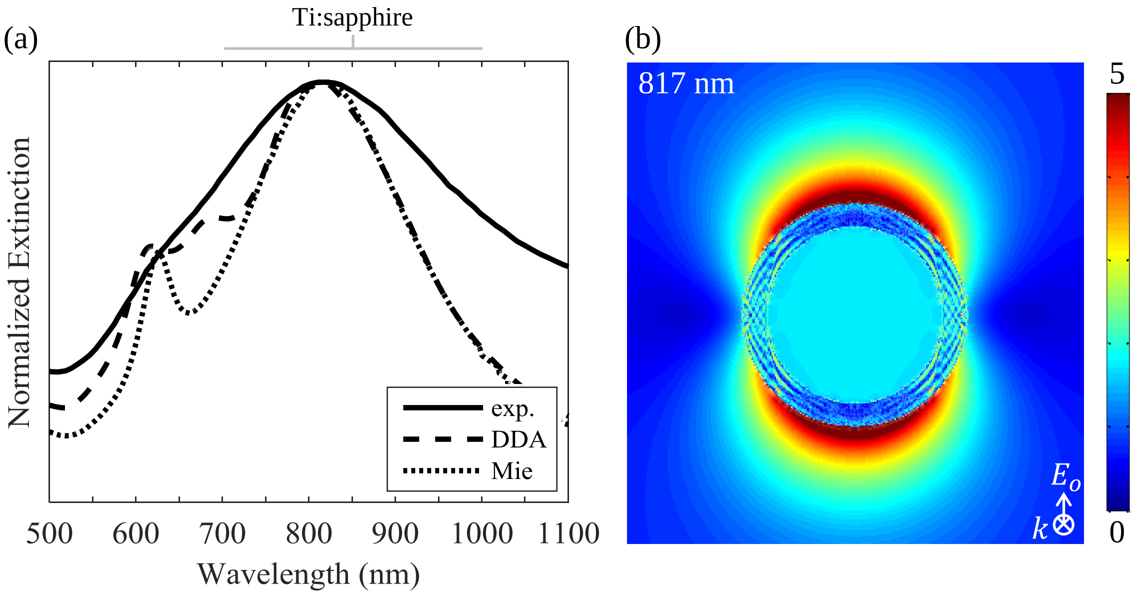

Figure 6.4: (a) Normalized extinction spectra for 150 nm Au nanoshells (15 nm Au shell; 120 nm diameter SiO_x core) in water according to transmission UV-vis measurements (solid), DDA (dashed), and Mie theory (dotted). Results from DDA and Mie theory were taken at an effective refractive index of 1.40 to account for PVP ligands on the Au. (b) Electric near-field enhancement (E/E_o) at the 817 nm dipole LSPR.

6.3 Second Harmonic Generation

Nonlinear SHG intensity from a ca. 1 µm length MoS_2 monolayer in the absence and presence of a plasmonic field from a 150 nm Au nanoshell (15 nm Au shell; 120 nm diameter SiO_x core) was measured using multi-photon confocal microscopy.[288] Figure 6.5 shows calculated linear optical extinction efficiency spectra for the Au nanoshell-MoS_2 heterostructure atop SiO_x

(to account for thermal oxide on the Si wafer) sans any nonlinear optical effects. Electric near-field intensity maps taken at each optical resonance are also shown. Maximas corresponding to MoS_2 C exciton, MoS_2 B exciton coupled with the Au nanoshell quadrupole LSPR, MoS_2 A exciton, and Au nanoshell dipole LSPR were observed at 450 nm, 623 nm, 660 nm, and 820 nm, respectively. The dipole and quadrupole LSPR of the Au nanoshell both red-shifted 3 nm from screening by the MoS_2 monolayer, consistent with related measurements.[230] Single photon (ω) and two-photon frequency (2ω) ranges accessible by the 810-1000 nm excitation spectrum used in the confocal microscope herein are labeled red and blue, respectively, for reference.

Equation 6.1 adapted Equation 1.5 to describe intensity of SHG as a function of competing mechanisms within the heterostructure across the 810-1000 nm excitation spectrum, assuming an undepleted pump and phase coherence.[33]

$$I_{2\omega} = \frac{\epsilon_o \omega^2}{8 n_{2\omega} c} \left[\chi_{2\omega}^{(2)}\right]^2 L^2 |E_\omega|^4 \qquad \text{(Equation 6.1)}$$

As the material source for SHG, monolayer MoS_2 determined $\chi_{2\omega}^{(2)}$ (second-order susceptibility) over L (its thickness) and n (linear refractive index). The Au nanoshells only augmented the excitation electric field intensity, E_ω; their centrosymmetric crystal structure precluded SHG by $\chi^{(2)} = 0$. Calculated linear optical extinction spectra in Figure 6.5 provided qualitative insights towards anticipated SHG trends based on competing influences of MoS_2 $\chi^{(2)}$ in the 2ω regime (blue) versus the Au nanoshell-enhanced E_ω in the ω regime (red). However based on Au nanoshell activity in the ω spectrum, the undepleted pump assumption underlying Equation 6.1 was not anticipated to hold constant across all excitation wavelengths. This constituted a third competing effect on SHG from the heterostructure.

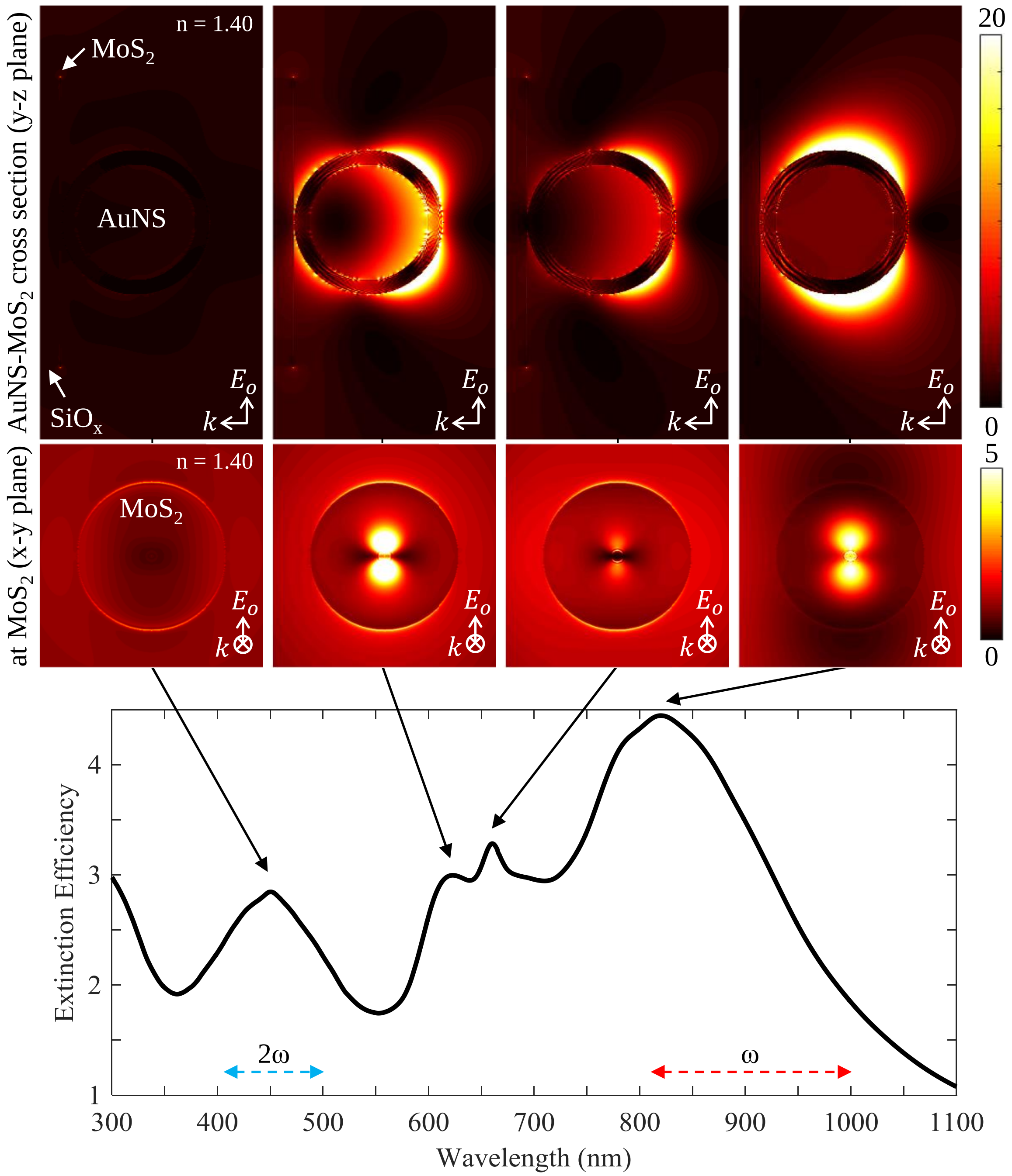

Figure 6.5: Calculated linear optical extinction efficiency of a 150 nm Au nanoshell (AuNS; 15 nm Au shell; 120 nm diameter SiO_x core) and monolayer MoS_2 heterostructure in water. The ω excitation and 2ω detection frequencies measured herein are labeled for reference. Enhanced electric near-field intensity $[(E/E_o)^2]$ plots at 450 nm, 623 nm, 660 nm, and 820 nm at two vantage points: (top) y-z plane cross-section of the AuNS and MoS_2 and (bottom) x-y plane of electric field incident upon the MoS_2 monolayer.

Second harmonic (SH) intensity per unit area was extracted from a ROI encompassing a Au nanoshell-MoS_2 heterostructure or one of its individual components. ROI for each MoS_2 site (with or without Au nanoshells) was selected based on its triangular boundaries. ROI for each isolated Au nanoshell was a circle with equivalent pixel area as the triangular ROI for MoS_2 sites. Total SH intensity per unit area at a given excitation wavelength was taken as raw intensity integrated across the finite SH bandwidth (dependent on temporal coherence of the Ti:sapphire laser). Inhomogeneity of drop-cast protocol secondarily resulted in isolated Au nanoshells and MoS_2 monolayers without Au nanoshells. These sites were analyzed independently as negative control data in § 6.3.1 and 6.3.2 to provide context for SHG from the heterostructure in § 6.3.3.

6.3.1 Molybdenum Disulfide

Nonlinear SHG from monolayer MoS_2 exhibited frequency-dependent intensity with maxima corresponding to expanded density of states from its van Hove singularity.[158,288] Figure 6.6 shows 2ω emission spectra arising from 810-1000 nm ω excitation of a ca. 1 µm length triangular MoS_2 monolayer. A SEM image and SHG micrographs (colored according to wavelength) are shown above; arrows correspond each micrograph with its spectra. Scattered SH signals appeared Lorentzian with ca. 5 nm bandwidths. Inset graph confirms second-order nonlinear behavior with a 1.80 dependence, which was lower than 2.0 likely due to absorption of the SH above the 1.86 eV MoS_2 bandgap. The C transition acts as a loss (absorption of SH signal) and as a SHG gain ($\chi^{(2)}$ resonance) simultaneously. It was noteworthy that SHG from MoS_2 remained finite at excitation wavelengths less than 810 nm and greater than 1000 nm, but acquisition parameters were optimized to fully capture the resonance behavior accessible from Ti:sapphire excitation. Intensity of the SH did not vary with time (data not shown for brevity), indicating no induced photodamage.

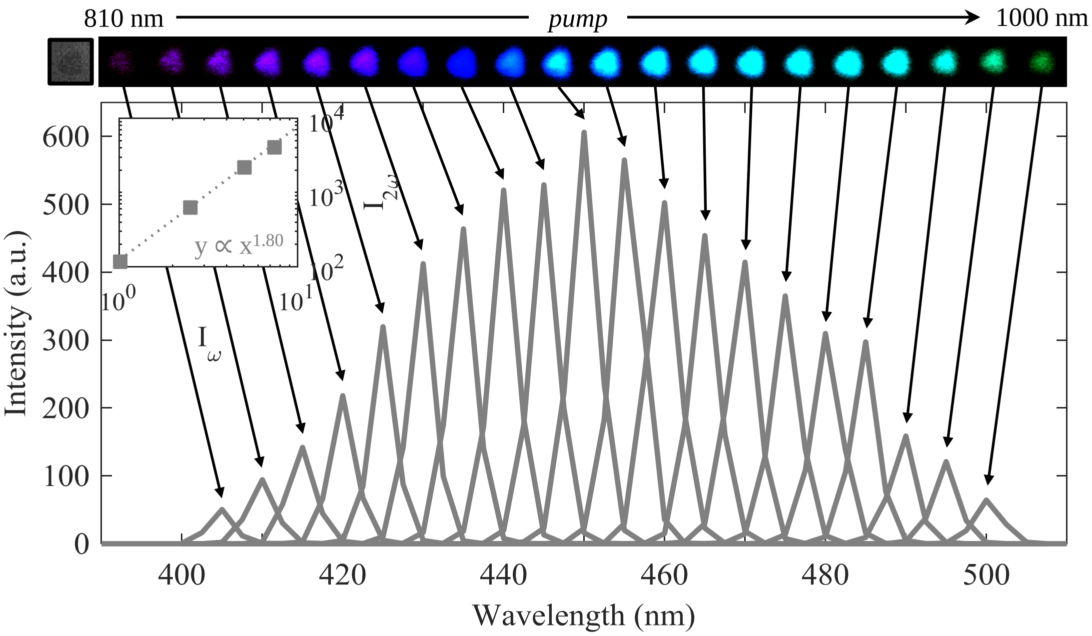

Figure 6.6: Representative SH scattering (per unit area) spectra from a ca. 1 μm MoS_2 monolayer at 810-1000 nm excitation (10 nm step). Inset shows 1.80-power dependence between SH and pump intensities taken at 880 nm excitation, confirming a second-order nonlinear process. SEM and SH micrographs of the MoS_2 crystal at each excitation wavelength are shown (top) with arrows indicating corresponding spectra.

Mean SHG intensity measured from ten distinct monolayer MoS_2 crystals exhibited a maxima at 450 nm associated with the C exciton, which was consistent with the DDA-calculated $\chi^{(2)}$ spectra in Figure 3.11 (see § 3.4.3).[288] Malard *et al*. also measured an association of SHG in this spectrum to the direct C exciton transitions near the Γ point at ca. 2.8 eV (450 nm).[50] Figure 6.7 shows the (a) mean SHG intensity per unit area and (b) mean of sample-normalized SH intensity of ten MoS_2 monolayers, along with superposed DDA-calculated $\chi^{(2)}$ spectra (dashed) and measured linear optical extinction spectra revealing the C transition in (b). Wide error bars in Figure 6.7(a) reflect minute variations in MoS_2 crystal size; SHG signal scales with material volume.[210] Normalizing SHG from each MoS_2 sample and taking the mean at each excitation frequency removed size dependence and allowed insights into the frequency-dependence of SHG arising from its electronic band structure.

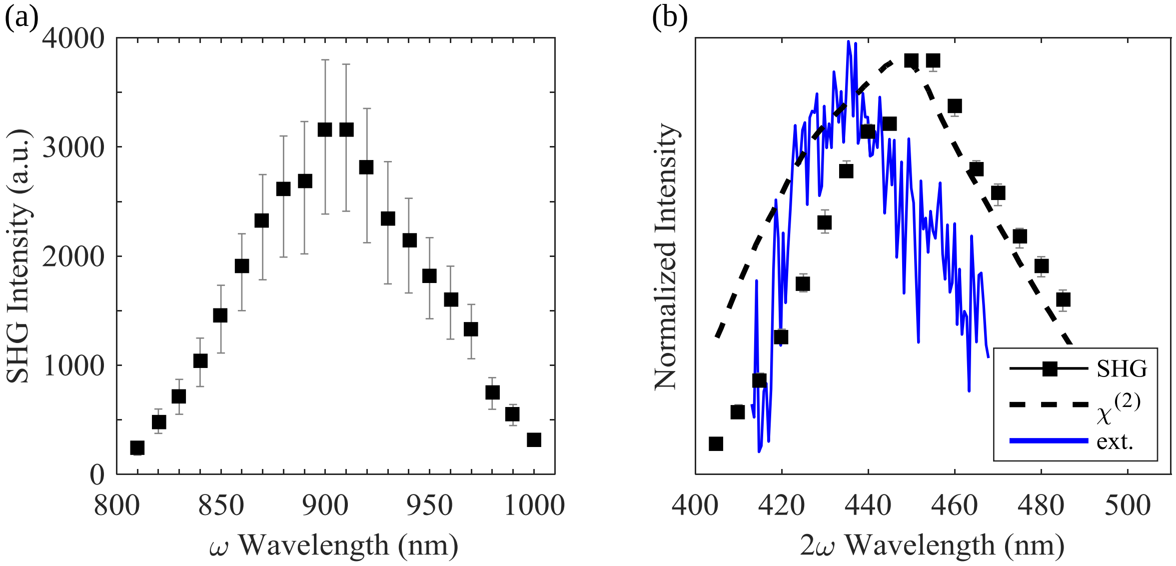

Figure 6.7: SHG behavior of averaged across ten distinct ca. 1 µm MoS_2 monolayers at 810-1000 nm ω excitation (10 nm step). (a) Mean integrated intensity per unit area of the SH versus excitation wavelength. (b) Mean of normalized intensity per unit area versus SH wavelengths (black squares; LHS) with superposed (i) DDA-calculated $\chi^{(2)}$ (dashed) and (ii) linear optical extinction spectra (blue). Error in each graph is the maximum and minimum from the mean; error in (a) accrued from minute variations in MoS_2 crystal size.

Measured SHG trend aligned closely with DDA-calculated $\chi^{(2)}$, which was based on a linear dielectric function and Miller's rule.[33,207,216] Increased states around the C exciton transition, shown in the linear optical extinction spectra, occurred 15 nm offset from the 450 nm SHG maximum, consistent with measurements by Malard *et al*.[50] Computation by density functional theory (DFT), density matrix theory (DMT), and a Bethe-Salpeter exciton (BSE) model of $\chi^{(2)}$ for MoS_2 corroborated these measured SHG trends.[49,53,54,206] A ca. 7 nm offset between maximal measured SHG and theoretical $\chi^{(2)}$ was ostensibly attributable to differences in experimental environment and handling protocols[239] between the MoS_2 sample used herein versus that used to obtain linear dielectric data by Mukherjee *et al*.[217] A 7 nm offset in occurrence of the C exciton maxima was also observed. Polarization-resolved SHG from the MoS_2 crystals to elucidate depolarization or crystal axis orientation was not measured herein, but has been well-characterized elsewhere.[49–51]

6.3.2 *Gold Nanoshells*

The Au nanoshells exhibited broadband luminescence rather than nonlinear SHG.[288] Figure 6.8 shows the negligible mean detected intensity in the 2ω spectrum from 810-1000 nm ω excitation of five Au nanoshells. Centrosymmetric face-centered cubic crystal structure of Au and amorphous structure of SiO_x prohibited SHG beyond minute surface contributions, where crystal symmetry was inherently broken.[289] Broadband luminescent emission independent of excitation frequency was observed, consistent with other reports of high-fluence laser excitation of metal nanoantennas.[290–293] The broadband luminescent emission was attributed to interband relaxation of d-orbital electrons in the Au.[293]

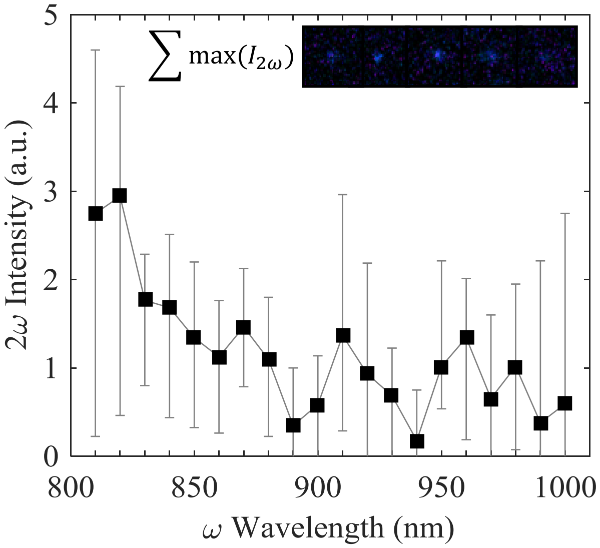

Figure 6.8: Mean 2ω emission intensity (per unit area) averaged across five distinct 150 nm Au nanoshells (15 nm Au shell; 120 nm diameter SiO_x core) from 810-1000 nm ω excitation (10 nm step). Error is the maximum and minimum from the mean. Inset are confocal images of the five individual Au nanoshells according to summed, maximum luminescence from 400 nm to 480 nm detected from a 5 µm z-scan using 820 nm excitation.

Spectral profile of 2ω luminescence was consistent with the LSPR profile in Figure 6.4, where intensity decreased as excitation was detuned from the dipole LSPR, similar to another report.[276] Inset to Figure 6.8 shows confocal images of the five isolated Au nanoshells that were acquired from 820 nm excitation by translating maximal detected 400-480 nm luminescence over a 5 µm z-scan into a 2D projection. This method of secondary image acquisition enabled visualization of singular, isolated Au nanoshells and was corroborated by SEM.

Nonlinear SHG from metal nanoantennas has been observed,[294–299] but with the caveat that progressive deviation from morphological centrosymmetry returned SH signal that would have been otherwise suppressed.[294,300,301] For example, Walsh *et al*. enhanced SHG 40x from Au nanocylinder arrays by plasmon-phonon transduction at various laser intensities to introduce morphological disorder into the otherwise centrosymmetric cylinders.[295] Augmentation of solely surface SHG by plasmon-enhanced local electric fields is an alternative mechanism that has been studied.[298] Spherical Au nanoshells with both centrosymmetric morphology and underlying crystallinity were studied herein, which resulted in negligible SHG.

6.3.3 Molybdenum Disulfide with a Gold Nanoshell

Nonlinear SHG from monolayer MoS_2 was enhanced, ostensibly by the surface plasmon-augmented local electric field from a single Au nanoshell.[288] Figure 6.9 shows 2ω emission spectra arising from 810-1000 nm ω excitation of a ca. 1 µm MoS_2 monolayer in the absence (gray) and presence (red) of one 150 nm Au nanoshell at its center. Corresponding SEM images and SHG micrographs (colored according to wavelength) are shown above; arrows correspond each confocal micrograph with its associated spectra. Inset graph confirms second-order nonlinear behavior of the heterostructure with a 1.77 dependence, which was 0.03 lower than the coefficient for MoS_2 due ostensibly to increased absorption from the Au nanoshell. Again, SHG remains finite at excitation wavelengths less than 810 nm and greater than 1000 nm.

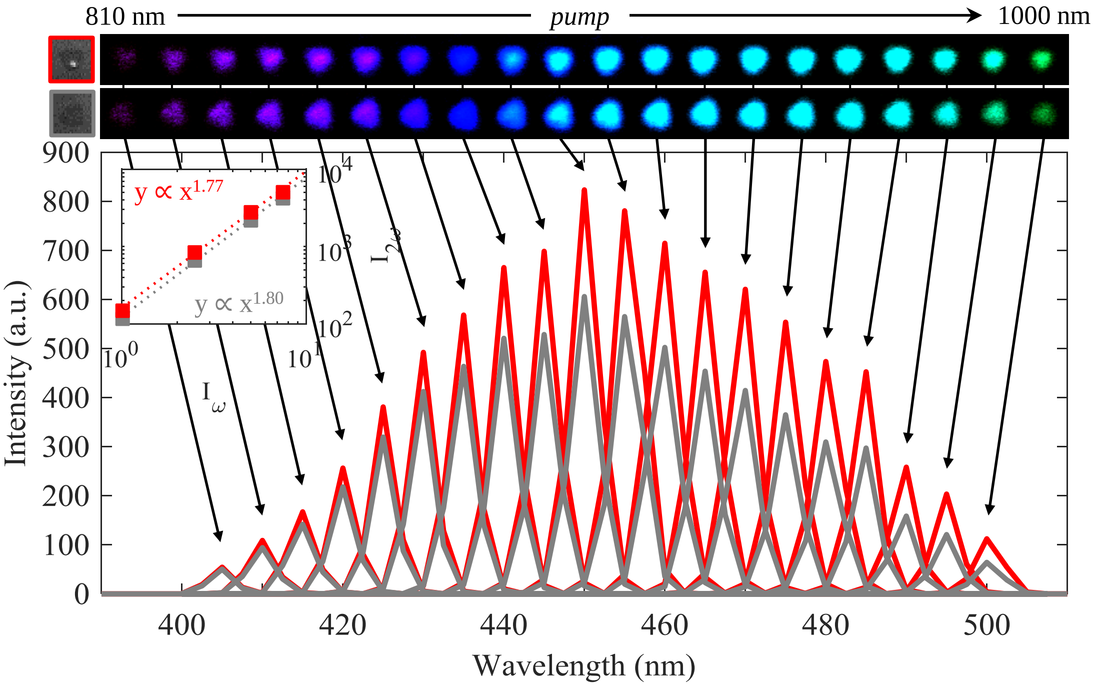

Figure 6.9: SH scattering (per unit area) spectra from a ca. 1 µm monolayer MoS_2 crystal at 810-1000 nm excitation (10 nm step) in the absence (gray) and presence (red) of a single 150 nm Au nanoshell (15 nm Au shell; 120 nm diameter SiO_x core). Inset shows 1.77- and 1.80-power dependence between SH and pump intensities taken at 880 nm excitation, confirming a second-order nonlinear process for the heterostructure and negative control, respectively. SEM and SH micrographs at each excitation wavelength are shown (top) with arrows to corresponding spectra.

Although enhanced 17-84%, frequency-dependence of enhanced SHG from the Au nanoshell-MoS_2 heterostructure shown in Figure 6.10 did not match the anticipated profile based on Equation 6.1 and the linear optical extinction spectrum in Figure 6.5.[288] The LSPR at 820 nm was anticipated to predominate and given higher SHG enhancements. Competition between (i) the plasmon-enhanced local field and (ii) MoS_2 $\chi^{(2)}$ was expected to yield to the former, whereby power dependence in Equation 6.1 was 4 versus 2, respectively.[33] Reported error for MoS_2 was the maximum and minimum from the mean across four crystals adjacent to the heterostructure. Potential consequences from plasmonic hot electron injection remained unclear. Overall, spectrum profile of enhanced SHG from the heterostructure closely resembled $\chi^{(2)}$ of MoS_2 because of nanoantenna design limitations, to be discussed in the forthcoming section.

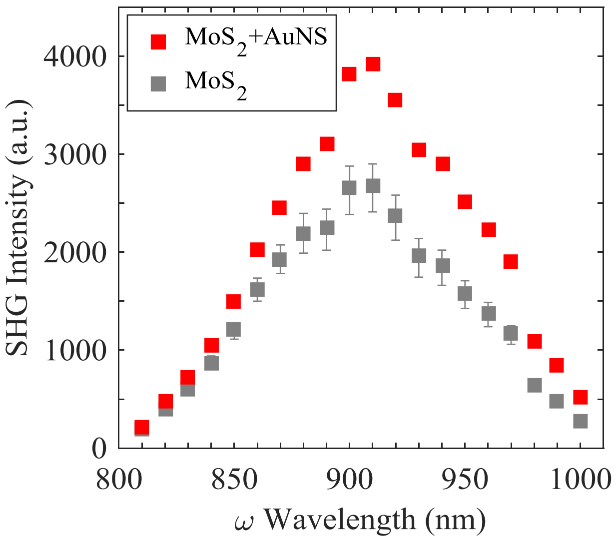

Figure 6.10: Integrated SHG intensity (per unit area) of a ca. 1 µm monolayer MoS$_2$ crystal at 810-1000 nm ω excitation (10 nm step) in the absence (gray; sample size of four) and presence (red; sample size of one) of a single 150 nm Au nanoshell (AuNS; 15 nm Au shell; 120 nm diameter SiO$_x$ core). Error is the maximum and minimum from the mean.

6.4 Enhanced Nonlinear Frequency Conversion Efficiency

Surface plasmon-augmented local fields appeared to be primarily responsible for enhanced SHG conversion efficiency from the Au nanoshell-MoS$_2$ monolayer heterostructure.[288] To date, plasmonic enhancement of SHG from an adjacent material has been quantified by (i) an intensity enhancement factor[274–277] or (ii) enhancement to an effective $\chi^{(2)}$ of the composite media.[273] Although magnitude and frequency dependence of intensity enhancement factors contain fingerprints of the underlying responsible mechanisms, its scope portrays a limited insight. Herein, performance of the heterostructure to convert incident irradiation to a SH was examined heuristically from the viewpoint of a conversion efficiency.

An *ab initio* estimation of SH conversion efficiency, $\eta_{2\omega}$, for MoS$_2$ was calculated to be up to 7x10^{-11}% at 5 mW irradiation per Equation 6.2 under the following assumptions:[302,303] (i) *L* of MoS_2 (6.5 Å) was within the confocal focus depth,[32] (ii) no pump depletion by the 2D MoS_2, (iii) phase coherence,[32,33] and (iv) DDA-calculated $\chi^{(2)}$ via Miller's rule.[207]

$$\eta_{2\omega} = \eta_{norm}\,(I_\omega L^2) \qquad \text{(Equation 6.2)}$$

$$\eta_{norm} \equiv \frac{2\pi^2\left[\chi_{2\omega}^{(2)}\right]^2}{{n_\omega}^2 n_{2\omega} c \epsilon_o {\lambda_\omega}^2} \qquad \text{(Equation 6.3)}$$

To allow direct comparison of SHG performance with other nonlinear materials, Equation 6.3 defines the normalized SHG conversion efficiency, η_{norm}, of excitation wavelength λ_ω. Note η_{norm} was independent of L and I_ω. An absolute calculation of $\eta_{2\omega}$ according to the relative measured intensities of the SH and excitation beams was precluded absent rigorously characterized signal losses in the confocal microscope (e.g., reflection losses at each lens/mirror, quantum efficiencies of PMT, etc.).

The η_{norm} for monolayer MoS_2 on SiO_x across the 810-1000 nm excitation spectrum was calculated using (i) DDA-simulated $\chi^{(2)}$ (via Miller's rule and corroborated by Hyper Rayleigh Scattering measurements; see § 3.4)[207] and (ii) n taken from Mukherjee *et al.*[217] In contrast to examining $\chi^{(2)}$ as the sole precursor for SHG spectrum profiles, Equation 6.3 also accounts for the wavelength and optical dispersion at the SH and excitation frequencies. Under the condition that local electric field augmentation by the Au nanoshell enhanced SHG, η_{norm} for MoS_2 was multiplied by DDA-calculated $(E/E_o)^2$ power enhancement factors at each excitation wavelength. This represented a theoretical η_{norm} for the heterostructure according to Equation 6.2. For a heuristic comparison, η_{norm} for MoS_2 was multiplied by the measured SHG enhancement factors at each excitation wavelength (i.e., ratio of curves in Figure 6.10). This comparison allowed attribution of measured SHG enhancement to enhanced local fields from the Au nanoshell in the absence of other gain mechanisms.

Enhanced optical power "delivered" to the MoS_2 monolayer from the Au nanoshell was first calculated by the DDA to account for frequency-dependent violation of the undepleted pump approximation underlying Equation 6.1.[288] Maximum optical power enhancement factor at the MoS_2 by the Au nanoshell dipole LSPR was 1.25, shown in Figure 6.11. Despite detuning away from the dipole LSPR, the enhanced optical power was nearly constant (within ±5%) across the 810-1000 nm excitation spectrum. This design deficiency was because of the spherical morphology of the Au nanoshell. Surface plasmon strength decays exponentially across space.[60,73,304] Herein, 75 nm separated the MoS_2 monolayer from the dipole axis of the Au nanoshell. Presence of PVP ligands (ca. 10 nm in length) likely exacerbated this issue.

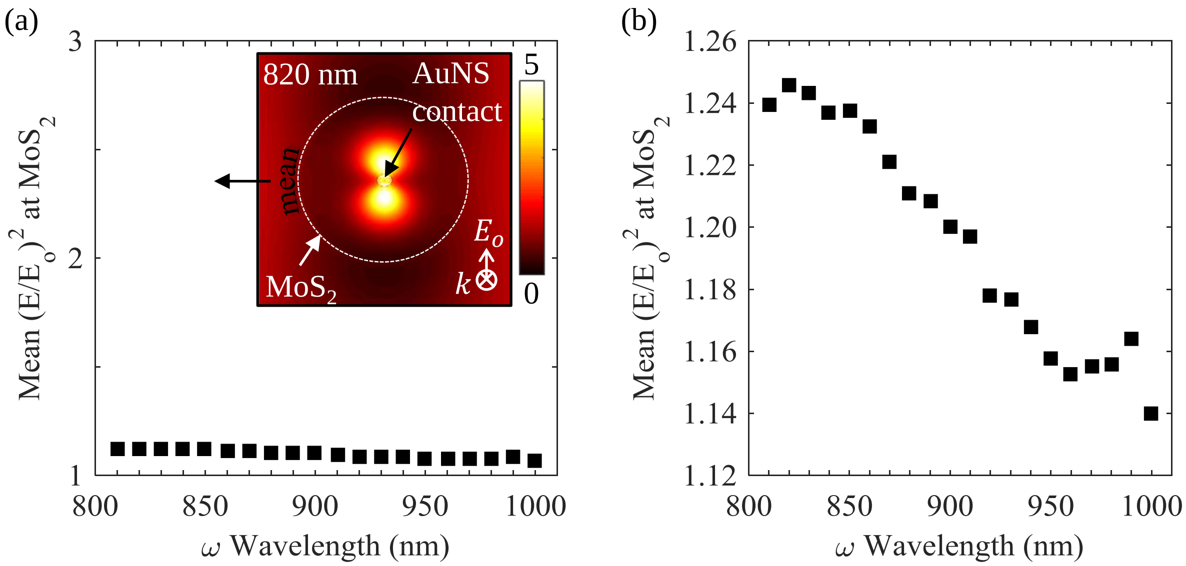

Figure 6.11: Mean enhanced optical power incident upon a 300 nm diameter MoS_2 monolayer by a 150 nm Au nanoshell (AuNS; 15 nm Au shell; 120 nm diameter SiO_x core) at 810-1000 nm ω excitation calculated by DDA plotted at (a) 0 to 5 scale and (b) 1.12 to 1.26 scale. The former was chosen according to scale of corresponding enhanced optical power plot at 820 nm, taken verbatim from Figure 6.5.

Conversely, excitation at the 623 nm quadrupole LSPR would have "delivered" more power to the MoS_2 because of closer physical proximity of its oscillating electrons to the MoS_2 monolayer, seen in its electric near-field plot of Figure 6.5. Replacement of the spherical Au nanoshell with an alternative nanoantenna of flat morphology, e.g., a nanorod or nanoring,[75,119,154] could have more effectively "delivered" optical power to the MoS_2.[230] LSPR activity of nanorods, however, are dependent on incident polarization which would have introduced an additional degree of convolution in data interpretation. Spherical nanoshells did not exhibit polarization dependence.[94] Nanorings would have required complex top-down lithography schemes.[120,125]

Figure 6.12(a) shows theoretical η_{norm} for monolayer MoS_2 in the absence (gray line) and presence (red line) of a single plasmonic Au nanoshell, under the conditions that the Au nanoshell (i) did not contribute SHG and (ii) enhanced η_{norm} according to its local electric field.[288] The MoS_2 control exhibited peak η_{norm} of 0.016% W^{-1}, which increased to 0.019% W^{-1} upon addition of a single nanoantenna. By comparison, ca. 10^{-4} % W^{-1} has been reported for lithium niobate technology[305–307] and ca. 1% W^{-1} for a complex Au metasurface coupled to indium gallium arsenide multi-quantum wells.[308]

Superposed as red squares Figure 6.12(a) is MoS_2 η_{norm} multiplied by the measured SHG enhancement factors (X; taken from Figure 6.10).[288] These heuristic "experimental" η_{norm} values agreed well with theoretical estimations in magnitude and frequency dependence. Subtle variances could be interpreted, however, such as the shoulder at 870 nm prevalent in the experimental data. Such subtleties ostensibly arose from differences between MoS_2 samples measured herein and that used by Mukherjee *et al.*,[217] as discussed earlier in § 6.3.1. This analysis was repeated in Figure 6.12(b) with an adjusted MoS_2 $\chi^{(2)}$ profile to resemble the unique sample studied herein. Briefly, the initial DDA-calculated $\chi^{(2)}$ based upon Mukherjee *et al.*[207] was red-shifted 7 nm according to equivalent mismatches in measured versus calculated (i) C exciton transition and (ii) SHG maxima [see Figure 6.7(b)]. Subsequently, the measured normalized SHG profile in Figure 6.7(b) was linearly scaled to their equivalent DDA-calculated $\chi^{(2)}$ magnitudes (see Figure 3.11).

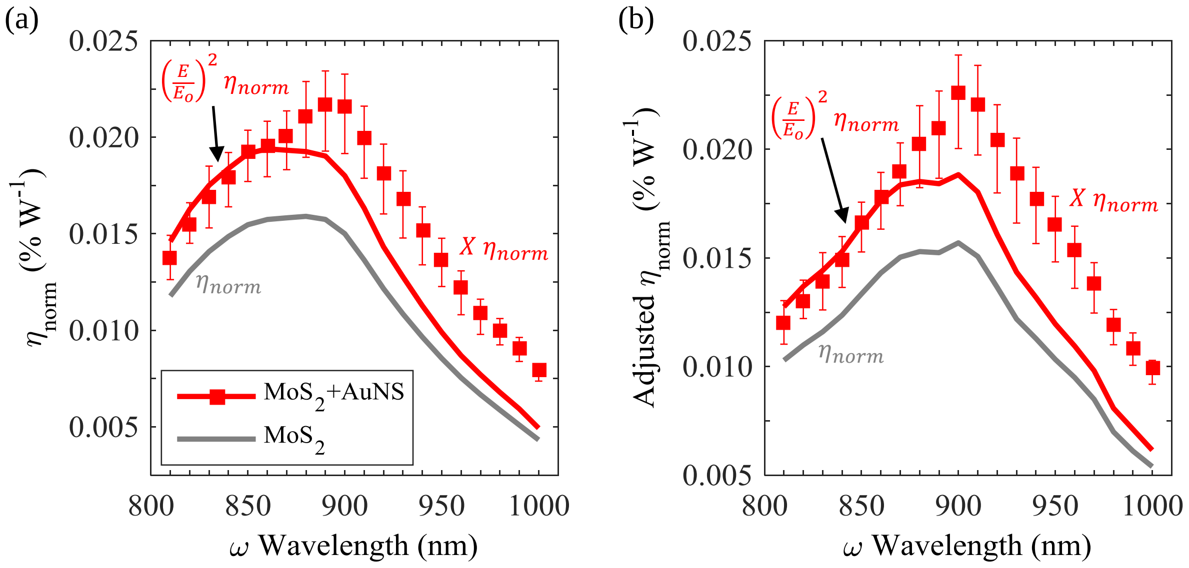

Figure 6.12: The η_{norm} for a MoS$_2$ monolayer in the absence (gray) and presence (red) a single 150 nm Au nanoshell (AuNS; 15 nm Au shell; 120 nm diameter SiO$_x$ core) according to an enhancement in the local electric field. "$(E/E_o)^2\ \eta_{norm}$" represents theoretical η_{norm} for the heterostructure (red line). "$X\ \eta_{norm}$" represents measured η_{norm} for the heterostructure (red squares), where X is the measured SHG enhancement factors (ratio of curves in Figure 6.10). Two approaches to the analysis are presented in (a) and (b), where the latter features an adjusted η_{norm} for each scenario after tuning the MoS$_2$ control η_{norm} to resemble the measured profile in Figure 6.7. Error is the maximum and minimum from the mean.

Agreement improved between the theoretical and heuristic experimental η_{norm} scenarios for the Au nanoshell-MoS$_2$ heterostructure after adjusting the profile of their underlying MoS$_2$ control η_{norm} to resemble measured SHG data in this work, shown in Figure 6.12(b). Taken together with underlying assumptions of the analysis, the overall agreement in magnitude and frequency dependence throughout Figure 6.12 implied that plasmonic electric-field augmentation was primarily responsible for measured SHG enhancement in the Au nanoshell-MoS$_2$ heterostructure. Ultimate $\eta_{2\omega}$ for the heterostructure improved to 9x10^{-10}% at 5 mW irradiation, per Equation 6.2. Other influences leading to measured SHG gain remain to be identified. Similar analyses were recently performed on SHG from tungsten diselenide (WSe$_2$) enhanced by a Si photonic crystal,[309] but absence of a negative control and convolution of the SH with broad luminescence made a rigorous comparison difficult.

6.5 Second Harmonic Generation Enhanced by Gold Nanoshell Dimers

Nonlinear SHG intensity from ca. 1 µm length MoS_2 monolayers interfaced with dimers of 150 nm Au nanoshells (15 nm Au shell; 120 nm diameter SiO_x core) exhibited enhancements consistent with surface plasmon-augmentation of the local electric field. Figure 6.13 shows measured SHG intensity enhancement factors, X, by a Au nanoshell dimer with (blue) 320 nm and (black) 150 nm gap relative to their negative controls. Strength of the local electric field within nanoantenna dimers scales with decreasing gap size due to capacitive coupling.[310–312] Corresponding SEM images are inset. Second-order dependence of SHG on excitation intensity was measured with 1.87 and 1.82 dependencies for 320 nm and 150 nm gap dimers, respectively (data not shown). Error bars represent the maximum and minimum from the mean arising from differences in MoS_2 control sample size, which was two in each case. Only one Au nanoshell dimer was measured at each gap size.

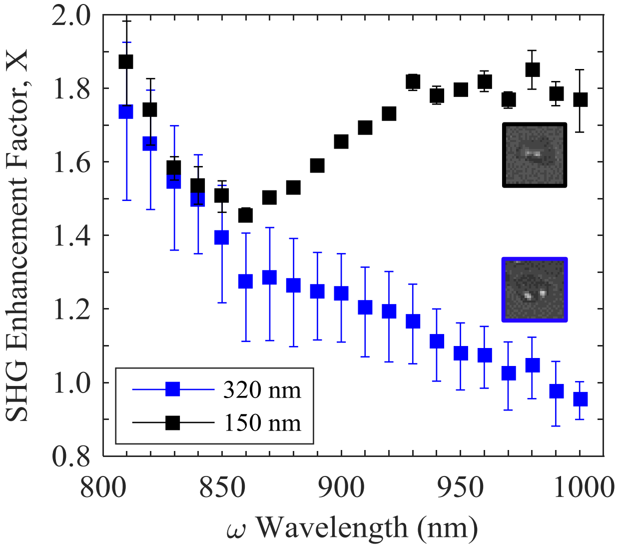

Figure 6.13: Measured SHG enhancement factor for ca. 1 µm monolayer MoS_2 crystals at 810-1000 nm ω excitation (10 nm step) by 150 nm Au nanoshell (AuNS; 15 nm Au shell; 120 nm diameter SiO_x core) dimers with (blue) 320 nm and (black) 150 nm gaps. Error is the maximum and minimum from the mean enhancement over two MoS_2 negative controls; one dimer was measured for each gap size.

Enhancement of SHG from MoS_2 at the nanoshell LSPR was highest for the 150 nm gap Au nanoshell dimer, reaching up to an 88% enhancement. Expanding the gap to 320 nm appeared to decrease the maximum enhancement to 74%, consistent with reduced inter-nanoshell coupling within the dimer. SHG enhancement decreased as the excitation wavelength was detuned from the LSPR, closely resembling profile of the DDA-calculated $(E/E_o)^2$ factors in Figure 6.11. Beyond 860 nm excitation, however, the measured SHG enhancement factor increased for the 150 nm gap dimer, ostensibly due to the emergence of a secondary plasmon resonance around 960 nm. Emergence of secondary plasmonic resonances at lower energies to the LSPR for nanosphere and nanorod dimers has been observed theoretically and experimentally,[133,148,313] arising from the coupled interaction. Appearance of such a coupled resonance was confirmed by DDA simulation for longitudinal excitation of the Au nanoshells arranged in a chain with 320 nm constant. Detailed characterization of these Au nanoshell dimer-based heterostructures is ongoing.

6.6 Summary

Nonlinear SHG from a ca. 1 µm length MoS_2 monolayer was broadband enhanced 17-84% by the surface plasmon activity of a single 150 nm Au nanoshell. Intensity of SHG from ten MoS_2 monolayers, five Au nanoshells, and a Au nanoshell-MoS_2 heterostructure were measured using a tunable Ti:sapphire laser coupled to a multi-photon confocal microscope with hyperspectral imaging capability. Plasmonic mode structure of Au-SiO_x nanoshell was characterized for the first time using EELS, revealing a 1.60 eV dark mode and 1.89 eV bright LSPR which red-shifted to 1.52 eV upon immersion into water. The 1.52 eV LSPR was responsible for measured SHG enhancement of the heterostructure. The SHG behavior of monolayer MoS_2 was measured to follow its frequency-dependent $\chi^{(2)}$ profile calculated by the DDA and agreed with other reports.

The Au nanoshells did not exhibit SHG in favor of broadband luminescence. Performance of the heterostructure was examined heuristically using a first-principles SHG conversion efficiency metric and enhanced optical power calculations from the DDA. Enhanced SHG from MoS_2 consistent with local field augmentation was also observed for Au nanoshell dimers. Overall, nonlinear SHG from MoS_2 in the presence of plasmonic fields was measured and described using *ab initio* theory and numerical computation.

CHAPTER 7

CONCLUDING REMARKS

Resonant photon-electron interactions in heterostructures of plasmonic nanoantennas and two-dimensional (2D) transition metal dichalcogenides (TMD) were examined, with emphasis in their infrared energy conversion capabilities through plasmonic hot electron transport and nonlinear frequency mixing. Plasmonic activity of nanoantennas in the presence of 2D TMD exhibited augmented damping characteristics, ostensibly due to hot electron transport. Nonlinear second harmonic generation (SHG) from monolayer molybdenum disulfide (MoS_2) was enhanced by the nanoantennas through their ability to localize energy into intense electric fields. Both findings supported the hypothesis. This chapter summarizes broader importance of the research, findings to date, and ongoing efforts in pursuit of nanoantenna-decorated 2D TMD as an optoelectronic material platform with improved heat rejection beyond conventional thermodynamic paths.

7.1 Importance of Work

Passive recycling of waste infrared energy for optoelectronic signal functionality has short-term importance in enhanced heat rejection and long-term impacts in device power consumption towards energy sustainability. Modern electronic devices (e.g., communication devices and medical sensors) are powered from environmentally toxic batteries or fossil fuel energies, of which approximately 60% of generated energy is wasted to radiation.[4,5] Concomitantly at the device level, efficient power consumption is limited by up to 80% losses across their electrical interconnects.[12,13] Rapid heat rejection mechanisms via nonlinear frequency conversion and/or hot electron transport could complement conventional thermodynamic mechanisms. Integration of such components could provide infrastructure to integrate all-optical, low loss interconnects at 10^3x higher data densities.[12,13] The U.S. Department of Energy has advocated that energy decarbonization and improving energy yield are keys to a sustainable future.[1]

7.2 Summary of Findings

Conversion of infrared energy through (i) plasmonic hot electron transport and (ii) nonlinear frequency mixing was examined in heterostructures of plasmonic nanoantennas and 2D TMD. Nonlinear SHG from infrared irradiation of a MoS_2 monolayer was enhanced 17-84% in the presence of a localized surface plasmon resonance (LSPR) on a gold (Au) nanoshell with efficiency up to 0.023% W^{-1}.[288] Capacitive coupling within nanoshell dimers further enhanced SHG from MoS_2. A 150 nm Au nanoshell was chosen for the heterostructure prototype, designed for an infrared LSPR according to discrete/coupled dipole models (i.e., DDA and CDA) for light extinction and electron energy loss spectroscopy (EELS).[82,94,287] Monolayer MoS_2 was chosen as the nonlinear optical source in the heterostructure prototype because of its intrinsically high second-order nonlinear susceptibility, $\chi^{(2)}$, measured to be 660±130 pm V^{-1} by Hyper Rayleigh Scattering.[207]

Transport of plasmonic hot electrons into 2D TMD was measured using EELS in a scanning transmission electron microscope (STEM). Initial studies on 80 nm Au nanospheres physically deposited onto MoS_2 suggested up to 4±2% quantum efficient hot electron transport over a 26 fs timescale.[218] Optimization of the nanoantenna-TMD ohmic junction by physicochemically bonding 20 nm Au nanoantennas to the TMD improved quantum efficiency to 11±5% and accelerated transport time to 7 fs.[261] Measured LSPR bandwidth expansion in the presence of TMD allowed quantitation of putative hot electron injection, after subtracting known damping contributions using DDA. Reliability of the DDA to describe resonant excitation and damping in metal-TMD heterostructures was explored using 80 nm Au nanospheres and 53 nm silver (Ag) nanoprisms interfaced with monolayer MoS_2.[230] Transmission UV-vis extinction measurements corroborated DDA-simulated resonant energies within 2% across different metals, shapes, proximity of LSPR to the MoS_2 bandgap energy, and nanoantenna-MoS_2 contact area. These studies allowed interpretation of their demonstrably enhanced SHG performance and plasmonic damping, ostensibly via hot electron transport.

Material and morphological parameters for designing infrared active plasmonic nanoantennas were expounded by Drude-Lorentz theory and the DDA.[75,82,94] Although aluminum-doped zinc oxide (Al:ZnO) and indium tin oxide (ITO) appeared well-suited for plasmon-functionalized infrared energy conversion because of their temperature stability above 1500 ºC, immature characterization and synthesis protocols precluded their use in favor of Au. Mimicking EELS in the DDA comprehensively characterized the morphological influences of radial elongation and annulation on the appearance of plasmonic modes in Au nanoantennas.[94] Infrared plasmonic activity of spherical Au nanoshells at ca. 1.5 eV was characterized by EELS in a STEM.[287] Overall, new insights into the resonant optoelectronics of coupled plasmonic and excitonic materials spanning the linear and nonlinear optical regimes were introduced in the contact of enhanced infrared energy conversion.

7.3 Future Directions

Understanding passive conversion of infrared energy via nonlinear frequency mixing or plasmonic hot electron injection could provide foundations to engineer heat rejection/harvesting strategies using surface plasmon resonance. Alternative plasmonic materials, namely aluminum-doped zinc oxide (Al:ZnO) or indium tin oxide (ITO), would be prime candidates for practical implementation of such strategies. Future nanoantenna-TMD heterostructure prototypes should consider use of Al:ZnO or ITO as their synthesis and electrodynamic understanding matures. Low losses relative to noble metals and resistance to structural deformation from greater than 1000 ˚C thermal gradients support their use as nanoantennas for such systems.[115]

Nonlinear SHG from ITO across a 1150-1670 nm infrared range was recently examined, showing broadband SHG from a 37 nm ITO that was equivalent to a 0.5 mm quartz plate.[314] Hence, ITO could serve a secondary energy conversion source. Nanoantenna morphology could reflect a recently proposed trapezoidal log-periodic architecture that was engineered for broadband infrared resonances with greater than 100x local power augmentation.[315] In lieu of nonlinear frequency mixing processes, infrared photons could also be upconverted to higher energies at 25% quantum efficiency though radiative recombination of plasmonic hot electrons injected into a quantum well.[28]

Efficiency of SHG conversion could be increased by engineering a secondary, higher-energy plasmon resonance with high scattering activity to emerge at the 2ω wavelength. Many nanoantenna designs have been proposed,[315–319] taking advantage of multi-pole resonances or near-field Fano coupling. Irradiation at the characteristic Fano dip, a dark plasmon resonance, avoids associated intrinsic losses in favor of improved field augmentation metrics over isolated or randomly arranged nanoantennas.[318] However, little experimental work has been performed[318,319] to date to corroborate frequency conversion performance of proposed designs. Such concepts could be extended to ITO or Al:ZnO nanoantennas to further improve SHG from TMD. Coupling the 2ω-active plasmon resonance with TMD excitonic transitions could further enhance SHG from heterostructures.[53] Unfortunately prototyping on these premises is hampered by laser technology and detection deficiencies of modern spectroscopy instrumentation.

Far-field Fano resonant coupling between surface plasmons and lattice diffraction in periodic lattices, resulting in a coupled lattice resonance (CLR), offer order-of-magnitude enhancements to TMD SHG in next-generation prototypes. Irradiation at the CLR of a Au dimer lattice has been shown to enhance its intrinsic SHG response by 30x.[311] Appearance of the CLR persists in the presence of TMD, whereby photoluminescence (PL) from monolayer molybdenum diselenide ($MoSe_2$) was recently enhanced 25x by the CLR of a Au nanorod lattice.[320] It is proposed herein to engineer a nanoantenna lattice with localized and coupled resonances (i.e., a surface plasmon and CLR) occurring at the 2ω and ω frequencies, respectively, to leverage their favorable electrodynamic behavior towards facilitating energy conversion processes for optoelectronics.

REFERENCES

1. S. Chu and A. Majumdar, "Opportunities and challenges for a sustainable energy future," *Nature* (2012), 488, 294.

2. International Energy Agency, *World Energy Outlook 2013* (2013).

3. R. Lee, "The outlook for population growth," *Science* (2011), 333, 569.

4. R. Segalman, J. Urban, and K. See, *Solution-Based Hybrid Thermoelectric Materials* (2013).

5. A. I. Hochbaum, R. Chen, R. D. Delgado, W. Liang, E. C. Garnett, M. Najarian, A. Majumdar, and P. Yang, "Enhanced thermoelectric performance of rough silicon nanowires," *Nature* (2008), 451, 163.

6. U.S. Energy Information Administration, *Annual Energy Review 2011* (2012).

7. C. J. Vineis, A. Shakouri, A. Majumdar, and M. G. Kanatzidis, "Nanostructured thermoelectrics: big efficiency gains from small features," *Advanced Materials* (2010), 22, 3970.

8. L. E. Bell, "Cooling, heating, generating power, and recovering waste heat with thermoelectric systems," *Science* (2008), 321, 1457.

9. M. Maldovan, "Sound and heat revolutions in phononics," *Nature* (2013), 503, 209.

10. R. E. Nelson, "A brief history of thermophotovoltaic development," *Semiconductor Science and Technology* (2003), 18, S141.

11. G. Min, "Thermoelectric Energy Harvesting," in *Energy Harvesting 2011* (Engineering and Physical Sciences Research Council, 2011).

12. E. Ozbay, "Plasmonics: merging photonics and electronics at nanoscale dimensions," *Science* (2006), 311, 189.

13. D. Miller, "Device requirements for optical interconnects to silicon chips," *Proceedings of the IEEE* (2009), 97, 1166.

14. D. Liang and J. E. Bowers, "Recent progress in lasers on silicon," *Nature Photonics* (2010), 4, 511.

15. W. L. Barnes, A. Dereux, and T. W. Ebbesen, "Surface plasmon subwavelength optics," *Nature* (2003), 424, 824.

16. M. L. Brongersma, N. J. Halas, and P. Nordlander, "Plasmon-induced hot carrier science and technology," *Nature Nanotechnology* (2015), 10, 25.

17. H. Hovel, S. Fritz, A. Hilger, U. Kreibig, and M. Vollmer, "Width of cluster plasmon

resonances: Bulk dielectric functions and chemical interface damping," *Physical Review B* (1993), 48, 18178.

18. C. Sönnichsen, T. Franzl, T. Wilk, G. von Plessen, J. Feldmann, O. Wilson, and P. Mulvaney, "Drastic reduction of plasmon damping in gold nanorods," *Physical Review Letters* (2002), 88, 77402.

19. A. Pinchuk and U. Kreibig, "Interface decay channel of particle surface plasmon resonance," *New Journal of Physics* (2003), 5, 151.

20. D. K. Roper, W. Ahn, and M. Hoepfner, "Microscale heat transfer transduced by surface plasmon resonant gold nanoparticles," *Journal of Physical Chemistry C* (2007), 111, 3636.

21. U. Kreibig, "Interface-induced dephasing of Mie plasmon polaritons," *Applied Physics B* (2008), 93, 79.

22. C. Clavero, "Plasmon-induced hot-electron generation at nanoparticle/metal-oxide interfaces for photovoltaic and photocatalytic devices," *Nature Photonics* (2014), 8, 95.

23. C. S. Kumarasinghe, M. Premaratne, Q. Bao, and G. P. Agrawal, "Theoretical analysis of hot electron dynamics in nanorods," *Scientific Reports* (2015), 5, 12140.

24. S. Dimitrijev, *Principles of Semiconductor Devices*, 2nd ed. (Oxford University Press, 2012), pg. 253-263.

25. K. Wu, W. E. Rodríguez-Córdoba, Y. Yang, and T. Lian, "Plasmon-induced hot electron transfer from the Au tip to CdS rod in CdS-Au nanoheterostructures," *Nano Letters* (2013), 13, 5255.

26. Y. Keun Lee, J. Lee, H. Lee, J.-Y. Lee, and J. Young Park, "Probing polarization modes of Ag nanowires with hot electron detection on Au/TiO2 nanodiodes," *Applied Physics Letters* (2013), 102, 123112.

27. G. Kaur, K. L. Yadav, and A. Mitra, "Localized surface plasmon induced enhancement of electron-hole generation with silver metal island at n-Al:ZnO/p-Cu2O heterojunction," *Applied Physics Letters* (2015), 107, 53901.

28. G. V. Naik and J. A. Dionne, "Photon upconversion with hot carriers in plasmonic systems," *Applied Physics Letters* (2015), 107, 133902.

29. Z. Fang, Y. Wang, Z. Liu, A. Schlather, P. M. Ajayan, F. H. L. Koppens, P. Nordlander, and N. J. Halas, "Plasmon-induced doping of graphene," *ACS Nano* (2012), 6, 10222.

30. Y. Kang, Y. Gong, Z. Hu, Z. Li, Z. Qiu, X. Zhu, P. M. Ajayan, and Z. Fang, "Plasmonic hot electron enhanced MoS_2 photocatalysis in hydrogen evolution," *Nanoscale* (2015), 7, 4482.

31. J. D. Jackson, *Classical Electrodynamics*, 2nd ed. (Wiley, 1975), pg. 27-30, 143-146, 658-662.

32. Y. R. Shen, *The Principles of Nonlinear Optics* (Wiley, 1984), pg. 2-5, 37-38, 42-52, 76, 86-93.

33. R. W. Boyd, *Nonlinear Optics*, 3rd ed. (Academic Press, 2008), pg. 1-17, 27-28, 74-84, 96-128.

34. P. Franken, A. Hill, C. Peters, and G. Weinreich, "Generation of optical harmonics," *Physical Review Letters* (1961), 7, 118.

35. N. Bloembergen and P. Pershan, "Light waves at the boundary of nonlinear media," *Physical Review* (1962), 128, 606.

36. J. A. Giordmaine, "Mixing of light beams in crystals," *Physical Review Letters* (1962), 8, 19.

37. M. Bass, P. A. Franken, J. F. Ward, and G. Weinreich, "Optical rectification," *Physical Review Letters* (1962), 9, 446.

38. M. J. Colles and C. R. Pidgeon, "Tunable lasers," *Reports on Progress in Physics* (1975), 38, 329.

39. Y. R. Shen, "Surface properties probed by second-harmonic and sum-frequency generation," *Nature* (1989), 337, 519.

40. P. F. Curley, A. I. Ferguson, J. G. White, and W. B. Amos, "Application of a femtosecond self-sustaining mode-locked Ti:sapphire laser to the field of laser scanning confocal microscopy," *Optical and Quantum Electronics* (1992), 24, 851.

41. Y. Guo, P. P. Ho, H. Savage, D. Harris, P. Sacks, S. Schantz, F. Liu, N. Zhadin, and R. R. Alfano, "Second-harmonic tomography of tissues," *Optics Letters* (1997), 22, 1323.

42. K. F. Mak, C. Lee, J. Hone, J. Shan, and T. F. Heinz, "Atomically thin MoS_2: a new direct-gap semiconductor," *Physical Review Letters* (2010), 105, 136805.

43. K. F. Mak and J. Shan, "Photonics and optoelectronics of 2D semiconductor transition metal dichalcogenides," *Nature Photonics* (2016), 10, 216.

44. O. V. Yazyev and A. Kis, "MoS_2 and semiconductors in the flatland," *Materials Today* (2014), 18, 20.

45. M. L. Brongersma and V. M. Shalaev, "The case for plasmonics," *Science* (2010), 328, 440.

46. J. A. Schuller, E. S. Barnard, W. Cai, Y. C. Jun, J. S. White, and M. L. Brongersma, "Plasmonics for extreme light concentration and manipulation," *Nature Materials* (2010), 9, 193.

47. D. Neshev and Y. Kivshar, "Nonlinear optics pushed to the edge," *Science* (2014), 344, 483.

48. N. Kumar, S. Najmaei, Q. Cui, F. Ceballos, P. Ajayan, J. Lou, and H. Zhao, "Second

harmonic microscopy of monolayer MoS_2," *Physical Review B* (2013), 87, 161403.

49. D. J. Clark, V. Senthilkumar, C. T. Le, D. L. Weerawarne, B. Shim, J. I. Jang, J. H. Shim, J. Cho, Y. Sim, M.-J. Seong, S. H. Rhim, A. J. Freeman, K.-H. Chung, and Y. S. Kim, "Strong optical nonlinearity of CVD-grown MoS_2 monolayer as probed by wavelength-dependent second-harmonic generation," *Physical Review B* (2014), 90, 121409.

50. L. M. Malard, T. V. Alencar, A. P. M. Barboza, K. F. Mak, and A. M. de Paula, "Observation of intense second harmonic generation from MoS_2 atomic crystals," *Physical Review B* (2013), 87, 201401.

51. Y. Li, Y. Rao, K. F. Mak, Y. You, S. Wang, C. R. Dean, and T. F. Heinz, "Probing symmetry properties of few-layer MoS_2 and h-BN by optical second-harmonic generation," *Nano Letters* (2013), 13, 3329.

52. C. Janisch, Y. Wang, D. Ma, N. Mehta, A. L. Elías, N. Perea-López, M. Terrones, V. Crespi, and Z. Liu, "Extraordinary second harmonic generation in tungsten disulfide monolayers," *Scientific Reports* (2014), 4, 5530.

53. M. L. Trolle, G. Seifert, and T. G. Pedersen, "Theory of excitonic second-harmonic generation in monolayer MoS_2," *Physical Review B* (2014), 89, 235410.

54. S. H. Rhim, Y. S. Kim, and A. J. Freeman, "Strain-induced giant second-harmonic generation in monolayered 2H-MoX_2 (X = S, Se, Te)," *Applied Physics Letters* (2015), 107, 241908.

55. M. Kauranen and A. V Zayats, "Nonlinear plasmonics," *Nature Photonics* (2012), 6, 737.

56. Y. Kang, S. Najmaei, Z. Liu, Y. Bao, Y. Wang, X. Zhu, N. J. Halas, P. Nordlander, P. M. Ajayan, J. Lou, and Z. Fang, "Plasmonic hot electron induced structural phase transition in a MoS_2 monolayer," *Advanced Materials* (2014), 26, 6467.

57. J. Lin, H. Li, H. Zhang, and W. Chen, "Plasmonic enhancement of photocurrent in MoS_2 field-effect-transistor," *Applied Physics Letters* (2013), 102, 203109.

58. Z. Yin, B. Chen, M. Bosman, X. Cao, J. Chen, B. Zheng, and H. Zhang, "Au nanoparticle-modified MoS_2 nanosheet-based photoelectrochemical cells for water splitting," *Small* (2014), 10, 3537.

59. K. M. Mayer and J. H. Hafner, "Localized surface plasmon resonance sensors," *Chemical Reviews* (2011), 111, 3828.

60. S. A. Maier and H. A. Atwater, "Plasmonics: localization and guiding of electromagnetic energy in metal/dielectric structures," *Journal of Applied Physics* (2005), 98, 11101.

61. H. J. Lezec, J. A. Dionne, and H. A. Atwater, "Negative refraction at visible frequencies," *Science* (2007), 316, 430.

62. T. W. Ebbesen, H. J. Lezec, H. F. Ghaemi, T. Thio, and P. A. Wolff, "Extraordinary optical transmission through sub-wavelength hole arrays," *Nature* (1998), 391, 667.

63. J. Z. Zhang and C. Noguez, "Plasmonic optical properties and applications of metal nanostructures," *Plasmonics* (2008), 3, 127.

64. G. Mie, "Beiträge zur Optik trüber Medien, speziell kolloidaler Metallösungen," *Annalen der Physik* (1908), 330, 377.

65. D. DeJarnette, J. Norman, and D. K. Roper, "Attribution of Fano resonant features to plasmonic particle size, lattice constant, and dielectric wavenumber in square nanoparticle lattices," *Photonics Research* (2014), 2, 15.

66. P. K. Jain, K. S. Lee, I. H. El-Sayed, and M. A. El-Sayed, "Calculated absorption and scattering properties of gold nanoparticles of different size, shape, and composition: applications in biological imaging and biomedicine," *Journal of Physical Chemistry B* (2006), 110, 7238.

67. S. Link and M. A. El-Sayed, "Size and temperature dependence of the plasmon absorption of colloidal gold nanoparticles," *Journal of Physical Chemistry B* (1999), 103, 4212.

68. C. L. Nehl and J. H. Hafner, "Shape-dependent plasmon resonances of gold nanoparticles," *Journal of Materials Chemistry* (2008), 18, 2415.

69. C. J. Orendorff, T. K. Sau, and C. J. Murphy, "Shape-dependent plasmon-resonant gold nanoparticles," *Small* (2006), 2, 636.

70. P. R. West, S. Ishii, G. V. Naik, N. K. Emani, V. M. Shalaev, and A. Boltasseva, "Searching for better plasmonic materials," *Laser and Photonics Reviews* (2010), 4, 795.

71. Y. Zhong, S. D. Malagari, T. Hamilton, and D. Wasserman, "Review of mid-infrared plasmonic materials," *Journal of Nanophotonics* (2015), 9, 93791.

72. U. Guler, V. M. Shalaev, and A. Boltasseva, "Nanoparticle plasmonics: Going practical with transition metal nitrides," *Materials Today* (2015), 18, 227.

73. J. N. Anker, W. P. Hall, O. Lyandres, N. C. Shah, J. Zhao, and R. P. Van Duyne, "Biosensing with plasmonic nanosensors," *Nature Materials* (2008), 7, 442.

74. D. K. Roper, W. Ahn, B. Taylor, and A. G. D. Asen, "Enhanced spectral sensing by electromagnetic coupling with localized surface plasmons on subwavelength structures," *IEEE Sensors* (2010), 10, 531.

75. G. T. Forcherio, P. Blake, D. DeJarnette, and D. K. Roper, "Nanoring structure, spacing, and local dielectric sensitivity for plasmonic resonances in Fano resonant square lattices," *Optics Express* (2014), 22, 17791.

76. E. M. Hicks, S. Zou, G. C. Schatz, K. G. Spears, R. P. Van Duyne, L. Gunnarsson, T.

Rindzevicius, B. Kasemo, and M. Käll, "Controlling plasmon line shapes through diffractive coupling in linear arrays of cylindrical nanoparticles fabricated by electron beam lithography," *Nano Letters* (2005), 5, 1065.

77. Y. Francescato, V. Giannini, and S. a Maier, "Plasmonic systems unveiled by Fano resonances," *ACS Nano* (2012), 6, 1830.

78. B. Luk'yanchuk, N. I. Zheludev, S. A. Maier, N. J. Halas, P. Nordlander, H. Giessen, and C. T. Chong, "The Fano resonance in plasmonic nanostructures and metamaterials," *Nature Materials* (2010), 9, 707.

79. D. DeJarnette, D. K. Roper, and B. Harbin, "Geometric effects on far-field coupling between multipoles of nanoparticles in square arrays," *Journal of the Optical Society of America B* (2012), 29, 88.

80. D. DeJarnette, G. G. Jang, P. Blake, and D. K. Roper, "Polarization angle affects energy of plasmonic features in Fano resonant regular lattices," *Journal of Optics* (2014), 16, 105006.

81. P. Blake, S. Kühne, G. T. Forcherio, and D. K. Roper, "Diffraction in nanoparticle lattices increases sensitivity of localized surface plasmon resonance to refractive index changes," *Journal of Nanophotonics* (2014), 8, 83084.

82. G. T. Forcherio, P. Blake, M. Seeram, D. DeJarnette, and D. K. Roper, "Coupled dipole plasmonics of nanoantennas in discontinuous, complex dielectric environments," *Journal of Quantitative Spectroscopy and Radiative Transfer* (2015), 166, 93.

83. F. Hao, Y. Sonnefraud, P. Van Dorpe, S. A. Maier, N. J. Halas, and P. Nordlander, "Symmetry breaking in plasmonic nanocavities: subradiant LSPR sensing and a tunable Fano resonance," *Nano Letters* (2008), 8, 3983.

84. Y. Zhang, F. Wen, Y.-R. Zhen, P. Nordlander, and N. J. Halas, "Coherent Fano resonances in a plasmonic nanocluster enhance optical four-wave mixing," *Proceedings of the National Academy of Sciences of the United States of America* (2013), 110, 9215.

85. J. A. Fan, K. Bao, L. Sun, J. Bao, V. N. Manoharan, P. Nordlander, and F. Capasso, "Plasmonic mode engineering with templated self-assembled nanoclusters," *Nano Letters* (2012), 12, 5318.

86. F. Hao, P. Nordlander, Y. Sonnefraud, P. Van Dorpe, and S. A. Maier, "Tunability of subradiant dipolar and Fano-type plasmon resonances in metallic ring/disk cavities: implications for nanoscale optical sensing," *ACS Nano* (2009), 3, 643.

87. K. Yee, "Numerical solution of initial boundary value problems involving Maxwell's equations in isotropic media," *IEEE Transactions on Antennas and Propagation* (1966), 14, 302.

88. M. I. Mishchenko, L. D. Travis, and D. W. Mackowski, "T-matrix method and its applications to electromagnetic scattering by particles: a current perspective," *Journal of*

Quantitative Spectroscopy and Radiative Transfer (2010), 111, 1700.

89. E. Purcell and C. Pennypacker, "Scattering and absorption of light by nonspherical dielectric grains," *The Astrophysical Journal* (1973), 186, 705.

90. B. T. Draine, "The discrete-dipole approximation and its application to interstellar graphite grains," *The Astrophysical Journal* (1988), 333, 848.

91. F. J. García de Abajo, "Optical excitations in electron microscopy," *Reviews of Modern Physics* (2010), 82, 209.

92. D. DeJarnette, P. Blake, G. T. Forcherio, and D. K. Roper, "Far-field Fano resonance in nanoring arrays modeled from extracted, point dipole polarizability," *Journal of Applied Physics* (2014), 115, 24306.

93. J. C. Norman, D. F. DeJarnette, and D. K. Roper, "Polylogarithm-Based Computation of Fano Resonance in Arrayed Dipole Scatterers," *Journal of Physical Chemistry C* (2014), 118, 627.

94. G. T. Forcherio, D. DeJarnette, M. Benamara, and D. K. Roper, "Electron energy loss spectroscopy of surface plasmon resonances on aberrant gold nanostructures," *Journal of Physical Chemistry C* (2016), 120, 24950.

95. D. DeJarnette, J. Norman, and D. K. Roper, "Spectral patterns underlying polarization-enhanced diffractive interference are distinguishable by complex trigonometry," *Applied Physics Letters* (2012), 101, 183104.

96. B. Auguié and W. Barnes, "Collective resonances in gold nanoparticle arrays," *Physical Review Letters* (2008), 101, 143902.

97. K. L. Kelly, E. Coronado, L. L. Zhao, and G. C. Schatz, "The optical properties of metal nanoparticles: the influence of size, shape, and dielectric environment," *Journal of Physical Chemistry B* (2003), 107, 668.

98. A. Mary, D. Koller, A. Hohenau, J. Krenn, A. Bouhelier, and A. Dereux, "Optical absorption of torus-shaped metal nanoparticles in the visible range," *Physical Review B* (2007), 76, 245422.

99. E. Simsek, "Full analytical model for obtaining surface plasmon resonance modes of metal nanoparticle structures embedded in layered media," *Optics Express* (2010), 18, 1722.

100. B. T. Draine and P. J. Flatau, "Discrete-dipole approximation for scattering calculations," *Journal of the Optical Society of America A* (1994), 11, 1491.

101. D. Gutkowicz-Krusin and B. T. Draine, "Propagation of Electromagnetic Waves on a Rectangular Lattice of Polarizable Points," *http://arxiv.org/abs/astro-ph/0403082* (2004),.

102. P. J. Flatau and B. T. Draine, "Fast near field calculations in the discrete dipole

approximation for rectangular rectilinear grids," *Optics Express* (2012), 20, 1247.

103. B. T. Draine and P. J. Flatau, "Discrete-dipole approximation for periodic targets: theory and tests," *Journal of the Optical Society of America A* (2008), 25, 2693.

104. N. W. Bigelow, A. Vaschillo, V. Iberi, J. P. Camden, and D. J. Masiello, "Characterization of the electron- and photon-driven plasmonic excitations of metal nanorods," *ACS Nano* (2012), 6, 7497.

105. N. Geuquet and L. Henrard, "EELS and optical response of a noble metal nanoparticle in the frame of a discrete dipole approximation," *Ultramicroscopy* (2010), 110, 1075.

106. A. Curry, G. Nusz, A. Chilkoti, and A. Wax, "Substrate effect on refractive index dependence of plasmon resonance for individual silver nanoparticles observed using darkfield micro-spectroscopy," *Optics Express* (2005), 13, 2668.

107. J. C. M. Garnett, "Colours in metal glasses and in metallic films," *Philosophical Transactions of the Royal Society A* (1904), 203, 385.

108. G. A. Niklasson, C. G. Granqvist, and O. Hunderi, "Effective medium models for the optical properties of inhomogeneous materials," *Applied Optics* (1981), 20, 26.

109. M. Faraday, "Experimental relations of gold (and other metals) to light," *Philosophical Transactions of the Royal Society London* (1857), 147, 145.

110. M. Fox, *Optical Properties of Solids,* 2nd ed. (Oxford University Press, 2010), pg. 33-41, 79-82.

111. R. Clausius, "L," *Die mechanische U'grmetheorie* (1879), 2, 62.

112. G. V. Naik, J. Kim, and A. Boltasseva, "Oxides and nitrides as alternative plasmonic materials in the optical range," *Optical Materials Express* (2011), 1, 1090.

113. P. B. Johnson and R. W. Christy, "Optical constants of the noble metals," *Physical Review B* (1972), 6, 4370.

114. M. A. Ordal, L. L. Long, R. J. Bell, S. E. Bell, R. R. Bell, R. W. Alexander, and C. A. Ward, "Optical properties of the metals Al, Co, Cu, Au, Fe, Pb, Ni, Pd, Pt, Ag, Ti, and W in the infrared and far infrared," *Applied Optics* (1983), 22, 1099.

115. D. R. Lide, *Handbook of Chemistry and Physics*, 87th ed. (CRC Press, 2006).

116. G. V. Naik, V. M. Shalaev, and A. Boltasseva, "Alternative plasmonic materials: Beyond gold and silver," *Advanced Materials* (2013), 25, 3264.

117. G. H. Chan, J. Zhao, E. M. Hicks, G. C. Schatz, and R. P. Van Duyne, "Plasmonic properties of copper nanoparticles fabricated by nanosphere lithography," *Nano Letters* (2007), 7, 1947.

118. R. D. Glover, J. M. Miller, and J. E. Hutchison, "Generation of metal nanoparticles from silver and copper objects: nanoparticle dynamics on surfaces and potential sources of nanoparticles in the environment," *ACS Nano* (2011), 5, 8950.

119. J. Aizpurua, P. Hanarp, D. Sutherland, M. Käll, G. Bryant, and F. J. García de Abajo, "Optical Properties of Gold Nanorings," *Physical Review Letters* (2003), 90, 57401.

120. C. Huang, J. Ye, S. Wang, T. Stakenborg, and L. Lagae, "Gold nanoring as a sensitive plasmonic biosensor for on-chip DNA detection," *Applied Physics Letters* (2012), 100, 173114.

121. E. M. Larsson, J. Alegret, M. Käll, and D. S. Sutherland, "Sensing characteristics of NIR localized surface plasmon resonances in gold nanorings for application as ultrasensitive biosensors," *Nano Letters* (2007), 7, 1256.

122. H. Liu, X. Wu, B. Li, C. Xu, G. Zhang, and L. Zheng, "Fano resonance in two-intersecting nanorings: Multiple layers of plasmon hybridizations," *Applied Physics Letters* (2012), 100, 153114.

123. N. Large, J. Aizpurua, V. K. Lin, S. L. Teo, R. Marty, S. Tripathy, and A. Mlayah, "Plasmonic properties of gold ring-disk nano-resonators: fine shape details matter," *Optics Express* (2011), 19, 5587.

124. Y. Cai, Y. Li, P. Nordlander, and P. S. Cremer, "Fabrication of elliptical nanorings with highly tunable and multiple plasmonic resonances," *Nano Letters* (2012), 12, 4881.

125. A. R. Halpern and R. M. Corn, "Lithographically patterned electrodeposition of gold, silver, and nickel nanoring arrays with widely tunable near-infrared plasmonic resonances," *ACS Nano* (2013), 7, 1755.

126. C. L. Haynes and R. P. Van Duyne, "Nanosphere lithography: a versatile nanofabrication tool for studies of size-dependent nanoparticle optics," *Journal of Physical Chemistry B* (2001), 105, 5599.

127. P. Blake, W. Ahn, and D. K. Roper, "Enhanced uniformity in arrays of electroless plated spherical gold nanoparticles using tin presensitization," *Langmuir* (2010), 26, 1533.

128. Y. Wang, A. Capretti, and L. Dal Negro, "Wide tuning of the optical and structural properties of alternative plasmonic materials," *Optical Materials Express* (2015), 5, 2415.

129. A. Calzolari, A. Ruini, and A. Catellani, "Transparent conductive oxides as near-IR plasmonic materials: the case of Al-doped ZnO derivatives," *ACS Photonics* (2014), 1, 703.

130. G. V Naik, J. Liu, A. V Kildishev, V. M. Shalaev, and A. Boltasseva, "Demonstration of Al:ZnO as a plasmonic component for near-infrared metamaterials," *Proc Natl Acad Sci U S A* (2012), 109, 8834.

131. Y. E. Kesim, E. Battal, and A. K. Okyay, "Plasmonic materials based on ZnO films and

their potential for developing broadband middle-infrared absorbers," *AIP Advances* (2014), 4, 77106.

132. E. Ringe, J. M. McMahon, K. Sohn, C. Cobley, Y. Xia, J. Huang, G. C. Schatz, L. D. Marks, and R. P. Van Duyne, "Unraveling the effects of size, composition, and substrate on the localized surface plasmon resonance frequencies of gold and silver nanocubes: A systematic single-particle approach," *Journal of Physical Chemistry C* (2010), 114, 12511.

133. M. Pelton, J. Aizpurua, and G. Bryant, "Metal-nanoparticle plasmonics," *Laser & Photonics Review* (2008), 2, 136.

134. F.-P. Schmidt, H. Ditlbacher, U. Hohenester, A. Hohenau, F. Hofer, and J. R. Krenn, "Dark plasmonic breathing modes in silver nanodisks," *Nano Letters* (2012), 12, 5780.

135. U. Hohenester, H. Ditlbacher, and J. Krenn, "Electron-Energy-Loss Spectra of Plasmonic Nanoparticles," *Physical Review Letters* (2009), 103, 106801.

136. R. Arenal, L. Henrard, L. Roiban, O. Ersen, J. Burgin, and M. Treguer-Delapierre, "Local plasmonic studies on individual core-shell gold-silver and pure gold nano-bipyramids," *Journal of Physical Chemistry C* (2014), 118, 25643.

137. L. Gu, W. Sigle, C. T. Koch, B. Ögüt, P. A. Van Aken, N. Talebi, R. Vogelgesang, J. Mu, X. Wen, and J. Mao, "Resonant wedge-plasmon modes in single-crystalline gold nanoplatelets," *Physical Review B* (2011), 83, 195433.

138. J. Nelayah, M. Kociak, O. Stéphan, N. Geuquet, L. Henrard, F. J. De García Abajo, I. Pastoriza-Santos, L. M. Liz-Marzán, and C. Colliex, "Two-dimensional quasistatic stationary short range surface plasmons in flat nanoprisms," *Nano Letters* (2010), 10, 902.

139. A. L. Koh, A. I. Fernández-Domínguez, D. W. McComb, S. A. Maier, and J. K. W. Yang, "High-resolution mapping of electron-beam-excited plasmon modes in lithographically defined gold nanostructures," *Nano Letters* (2011), 11, 1323.

140. M.-W. Chu, V. Myroshnychenko, C. H. Chen, J.-P. Deng, C.-Y. Mou, and F. J. García de Abajo, "Probing bright and dark surface-plasmon modes in individual and coupled noble metal nanoparticles using an electron beam," *Nano Letters* (2009), 9, 399.

141. G. Boudarham, N. Feth, V. Myroshnychenko, S. Linden, J. García De Abajo, M. Wegener, and M. Kociak, "Spectral imaging of individual split-ring resonators," *Physical Review Letters* (2010), 105, 255501.

142. F. P. Schmidt, H. Ditlbacher, F. Hofer, J. R. Krenn, and U. Hohenester, "Morphing a plasmonic nanodisk into a nanotriangle," *Nano Letters* (2014), 14, 4810.

143. G. Boudarham and M. Kociak, "Modal decompositions of the local electromagnetic density of states and spatially resolved electron energy loss probability in terms of geometric modes," *Physical Review B* (2012), 85, 245447.

144. F. J. Garcia de Abajo and M. Kociak, "Probing the photonic local density of states with electron energy loss spectroscopy," *Physical Review Letters* (2008), 100, 106804.

145. M. Kociak and O. Stéphan, "Mapping plasmons at the nanometer scale in an electron microscope," *Chemical Society Reviews* (2014), 43, 3865.

146. C. Cherqui, N. W. Bigelow, A. Vaschillo, H. Goldwyn, and D. J. Masiello, "Combined tight-binding and numerical electrodynamics understanding of the STEM/EELS magneto-optical responses of aromatic plasmon-supporting metal oligomers," *ACS Photonics* (2014), 1, 1013.

147. W. Sigle, J. Nelayah, C. T. Koch, B. Ögüt, L. Gu, and P. A. van Aken, "EFTEM study of surface plasmon resonances in silver nanoholes," *Ultramicroscopy* (2010), 110, 1094.

148. S. Kadkhodazadeh, J. R. De Lasson, M. Beleggia, H. Kneipp, J. B. Wagner, and K. Kneipp, "Scaling of the surface plasmon resonance in gold and silver dimers probed by EELS," *Journal of Physical Chemistry C* (2014), 118, 5478.

149. Y. B. Zheng, B. K. Juluri, X. Mao, T. R. Walker, and T. J. Huang, "Systematic investigation of localized surface plasmon resonance of long-range ordered Au nanodisk arrays," *Journal of Applied Physics* (2008), 103, 14308.

150. J. A. Scholl, A. L. Koh, and J. A. Dionne, "Quantum plasmon resonances of individual metallic nanoparticles," *Nature* (2012), 483, 421.

151. M. Bosman, V. J. Keast, M. Watanabe, A. I. Maaroof, and M. B. Cortie, "Mapping surface plasmons at the nanometre scale with an electron beam," *Nanotechnology* (2007), 18, 165505.

152. C. Diaz-Egea, W. Sigle, P. A. van Aken, and S. I. Molina, "High spatial resolution mapping of surface plasmon resonance modes in single and aggregated gold nanoparticles assembled on DNA strands," *Nanoscale Research Letters* (2013), 8, 337.

153. C. Matyssek, V. Schmidt, W. Hergert, and T. Wriedt, "The T-Matrix method in electron energy loss and cathodoluminescence spectroscopy calculations for metallic nano-particles," *Ultramicroscopy* (2012), 117, 46.

154. P. K. Jain, S. Eustis, and M. A. El-Sayed, "Plasmon coupling in nanorod assemblies: optical absorption, discrete dipole approximation simulation, and exciton-coupling model," *Journal of Physical Chemistry B* (2006), 110, 18243.

155. S. Panaro, A. Nazir, C. Liberale, G. Das, H. Wang, F. De Angelis, R. Proietti Zaccaria, E. Di Fabrizio, and A. Toma, "Dark to bright mode conversion on dipolar nanoantennas: a symmetry-breaking approach," *ACS Photonics* (2014), 1, 310.

156. J. Ye, P. Van Dorpe, L. Lagae, G. Maes, and G. Borghs, "Observation of plasmonic dipolar anti-bonding mode in silver nanoring structures," *Nanotechnology* (2009), 20, 465203.

157. M. Prieto, R. Arenal, L. Henrard, L. Gomez, V. Sebastian, and M. Arruebo, "Morphological tunability of the plasmonic response: from hollow gold nanoparticles to gold nanorings," *Journal of Physical Chemistry C* (2014), 118, 28804.

158. A. R. Klots, A. K. M. Newaz, B. Wang, D. Prasai, H. Krzyzanowska, D. Caudel, N. J. Ghimire, J. Yan, B. L. Ivanov, K. A. Velizhanin, A. Burger, D. G. Mandrus, N. H. Tolk, S. T. Pantelides, and K. I. Bolotin, "Probing excitonic states in ultraclean suspended two-dimensional semiconductors by photocurrent spectroscopy," *Scientific Reports* (2014), 4, 6608.

159. R. F. Frindt and A. D. Yoffe, "Physical properties of layer structures: optical properties and photoconductivity of thin crystals of molybdenum disulphide," *Proceedings of the Royal Society A* (1963), 273, 69.

160. R. F. Frindt, "Optical absorption of a few unit-cell layers of MoS_2," *Physical Review* (1965), 140, A536.

161. R. F. Frindt, "Single crystals of MoS_2 several molecular layers thick," *Journal of Applied Physics* (1966), 37, 1928.

162. K. S. Novoselov, A. K. Geim, S. V Morozov, D. Jiang, Y. Zhang, S. V Dubonos, I. V Grigorieva, and A. A. Firsov, "Electric field effect in atomically thin carbon films," *Science* (2004), 306, 666.

163. T. F. Jaramillo, K. P. Jorgensen, J. Bonde, J. H. Nielsen, S. Horch, and I. Chorkendorff, "Identification of active edge sites for electrochemical H_2 evolution from MoS_2 nanocatalysts," *Science* (2007), 317, 100.

164. B. Radisavljevic, M. B. Whitwick, and A. Kis, "Integrated circuits and logic operations based on single-layer MoS_2," *ACS Nano* (2011), 5, 9934.

165. Q. H. Wang, K. Kalantar-Zadeh, A. Kis, J. N. Coleman, and M. S. Strano, "Electronics and optoelectronics of two-dimensional transition metal dichalcogenides," *Nature Nanotechnology* (2012), 7, 699.

166. R. Suzuki, M. Sakano, Y. J. Zhang, R. Akashi, D. Morikawa, A. Harasawa, K. Yaji, K. Kuroda, K. Miyamoto, T. Okuda, K. Ishizaka, R. Arita, and Y. Iwasa, "Valley-dependent spin polarization in bulk MoS_2 with broken inversion symmetry," *Nature Nanotechnology* (2014), 9, 611.

167. M. Acerce, D. Voiry, and M. Chhowalla, "Metallic 1T phase MoS_2 nanosheets as supercapacitor electrode materials," *Nature Nanotechnology* (2015), 10, 313.

168. G. Eda, H. Yamaguchi, D. Voiry, T. Fujita, M. Chen, and M. Chhowalla, "Photoluminescence from chemically exfoliated MoS_2," *Nano Letters* (2011), 11, 5111.

169. D. Li, W. Xiong, L. Jiang, Z. Xiao, H. Rabiee Golgir, M. Wang, X. Huang, Y. Zhou, Z. Lin, J. Song, S. Ducharme, L. Jiang, J.-F. Silvain, and Y. Lu, "Multimodal nonlinear optical

imaging of MoS_2 and MoS_2-based van der Waals heterostructures," *ACS Nano* (2016), 10, 3766.

170. G. Aivazian, Z. Gong, A. M. Jones, R.-L. Chu, J. Yan, D. G. Mandrus, C. Zhang, D. Cobden, W. Yao, and X. Xu, "Magnetic control of valley pseudospin in monolayer WSe_2," *Nature Physics* (2015), 11, 148.

171. A. Fert, "Nobel Lecture: Origin, development, and future of spintronics," *Reviews of Modern Physics* (2008), 80, 1517.

172. B. Radisavljevic, A. Radenovic, J. Brivio, V. Giacometti, and A. Kis, "Single-layer MoS_2 transistors," *Nature Nanotechnology* (2011), 6, 147.

173. B. W. H. Baugher, H. O. H. Churchill, Y. Yang, and P. Jarillo-Herrero, "Intrinsic electronic transport properties of high-quality monolayer and bilayer MoS_2," *Nano Letters* (2013), 13, 4212.

174. M. B. Dines, "Lithium intercalation via -Butyllithium of the layered transition metal dichalcogenides," *Materials Research Bulletin* (1975), 10, 287.

175. L. Niu, J. N. Coleman, H. Zhang, H. Shin, M. Chhowalla, and Z. Zheng, "Production of Two-Dimensional Nanomaterials via Liquid-Based Direct Exfoliation," *Small* (2016), 12, 272.

176. J. N. Coleman, M. Lotya, A. O’Neill, S. D. Bergin, P. J. King, U. Khan, K. Young, A. Gaucher, S. De, R. J. Smith, I. V Shvets, S. K. Arora, G. Stanton, H.-Y. Kim, K. Lee, G. T. Kim, G. S. Duesberg, T. Hallam, J. J. Boland, J. J. Wang, J. F. Donegan, J. C. Grunlan, G. Moriarty, A. Shmeliov, R. J. Nicholls, J. M. Perkins, E. M. Grieveson, K. Theuwissen, D. W. McComb, P. D. Nellist, and V. Nicolosi, "Two-dimensional nanosheets produced by liquid exfoliation of layered materials," *Science* (2011), 331, 568.

177. V. Nicolosi, M. Chhowalla, M. G. Kanatzidis, M. S. Strano, and J. N. Coleman, "Liquid Exfoliation of Layered Materials," *Science* (2013), 340, 1226419.

178. M. M. Benameur, B. Radisavljevic, J. S. Héron, S. Sahoo, H. Berger, and A. Kis, "Visibility of dichalcogenide nanolayers," *Nanotechnology* (2011), 22, 125706.

179. H.-L. Tsai, J. Heising, J. L. Schindler, C. R. Kannewurf, and M. G. Kanatzidis, "Exfoliated−Restacked Phase of WS_2," *Chemistry of Materials* (1997), 9, 879.

180. C. Backes, R. J. Smith, N. McEvoy, N. C. Berner, D. McCloskey, H. C. Nerl, A. O’Neill, P. J. King, T. Higgins, D. Hanlon, N. Scheuschner, J. Maultzsch, L. Houben, G. S. Duesberg, J. F. Donegan, V. Nicolosi, and J. N. Coleman, "Edge and confinement effects allow in situ measurement of size and thickness of liquid-exfoliated nanosheets," *Nature Communications* (2014), 5, 4576.

181. C. Backes, B. M. Szydłowska, A. Harvey, S. Yuan, V. Vega-Mayoral, B. R. Davies, P. Zhao, D. Hanlon, E. J. G. Santos, M. I. Katsnelson, W. J. Blau, C. Gadermaier, and J. N.

Coleman, "Production of Highly Monolayer Enriched Dispersions of Liquid-Exfoliated Nanosheets by Liquid Cascade Centrifugation," *ACS Nano* (2016), 10, 1589.

182. Y. Zhan, Z. Liu, S. Najmaei, P. M. Ajayan, and J. Lou, "Large-area vapor-phase growth and characterization of MoS_2 atomic layers on a SiO_2 substrate," *Small* (2012), 8, 966.

183. Y. H. Lee, X. Q. Zhang, W. Zhang, M. T. Chang, C. Te Lin, K. Di Chang, Y. C. Yu, J. T. W. Wang, C. S. Chang, L. J. Li, and T. W. Lin, "Synthesis of large-area MoS_2 atomic layers with chemical vapor deposition," *Advanced Materials* (2012), 24, 2320.

184. X. Wang, Y. Gong, G. Shi, W. L. Chow, K. Keyshar, G. Ye, R. Vajtai, J. Lou, Z. Liu, E. Ringe, B. K. Tay, and P. M. Ajayan, "Chemical Vapor Deposition Growth of Crystalline Monolayer $MoSe_2$," *ACS Nano* (2014), 8, 5125.

185. C. Cong, J. Shang, X. Wu, B. Cao, N. Peimyoo, C. Qiu, L. Sun, and T. Yu, "Synthesis and optical properties of large-area single-crystalline 2D semiconductor WS_2 monolayer from chemical vapor deposition," *Advanced Optical Materials* (2014), 2, 131.

186. S. Najmaei, Z. Liu, W. Zhou, X. Zou, G. Shi, S. Lei, B. I. Yakobson, J.-C. Idrobo, P. M. Ajayan, and J. Lou, "Vapour phase growth and grain boundary structure of molybdenum disulphide atomic layers," *Nature Materials* (2013), 12, 754.

187. A. M. van der Zande, P. Y. Huang, D. A. Chenet, T. C. Berkelbach, Y. You, G.-H. Lee, T. F. Heinz, D. R. Reichman, D. A. Muller, and J. C. Hone, "Grains and grain boundaries in highly crystalline monolayer molybdenum disulphide," *Nature Materials* (2013), 12, 554.

188. Y. Kim, H. Bark, G. H. Ryu, Z. Lee, and C. Lee, "Wafer-scale monolayer MoS2 grown by chemical vapor deposition using a reaction of MoO_3 and H_2S," *Journal of Physics: Condensed Matter* (2016), 28, 6.

189. K. Kang, S. Xie, L. Huang, Y. Han, P. Y. Huang, K. F. Mak, C.-J. Kim, D. Muller, and J. Park, "High-mobility three-atom-thick semiconducting films with wafer-scale homogeneity," *Nature* (2015), 520, 656.

190. R. J. Smith, P. J. King, M. Lotya, C. Wirtz, U. Khan, S. De, A. O'Neill, G. S. Duesberg, J. C. Grunlan, G. Moriarty, J. Chen, J. Wang, A. I. Minett, V. Nicolosi, and J. N. Coleman, "Large-scale exfoliation of inorganic layered compounds in aqueous surfactant solutions," *Advanced Materials* (2011), 23, 3944.

191. M. Lotya, A. Rakovich, J. F. Donegan, and J. N. Coleman, "Measuring the lateral size of liquid-exfoliated nanosheets with dynamic light scattering," *Nanotechnology* (2013), 24, 265703.

192. A. O'Neill, U. Khan, and J. N. Coleman, "Preparation of high concentration dispersions of exfoliated MoS_2 with increased flake size," *Chemistry of Materials* (2012), 24, 2414.

193. K. M. McCreary, A. T. Hanbicki, G. G. Jernigan, J. C. Culbertson, and B. T. Jonker, "Synthesis of large-area WS_2 monolayers with exceptional photoluminescence," *Scientific*

Reports (2016), 6, 19159.

194. B. Liu, L. Chen, G. Liu, A. N. Abbas, M. Fathi, and C. Zhou, "High-performance chemical sensing using Schottky-contacted chemical vapor deposition grown monolayer MoS_2 transistors," *ACS Nano* (2014), 8, 5304.

195. X. Ling, Y. Lee, Y. Lin, W. Fang, L. Yu, M. S. Dresselhaus, and J. Kong, "Role of the seeding promoter in MoS_2 growth by chemical vapor deposition," *Nano Letters* (2014), 14, 140129131422004.

196. Y.-H. Chang, W. Zhang, Y. Zhu, Y. Han, J. Pu, J.-K. Chang, W.-T. Hsu, J.-K. Huang, C.-L. Hsu, M.-H. Chiu, T. Takenobu, H. Li, C.-I. Wu, W.-H. Chang, A. T. S. Wee, and L.-J. Li, "Monolayer $MoSe_2$ grown by chemical vapor deposition for fast photodetection," *ACS Nano* (2014), 8, 8582.

197. J.-K. Huang, J. Pu, C.-L. Hsu, M.-H. Chiu, Z.-Y. Juang, Y.-H. Chang, W.-H. Chang, Y. Iwasa, T. Takenobu, and L.-J. Li, "Large-area synthesis of highly crystalline WSe_2 monolayers and device applications," *ACS Nano* (2014), 8, 923.

198. D. Kozawa, R. Kumar, A. Carvalho, K. Kumar Amara, W. Zhao, S. Wang, M. Toh, R. M. Ribeiro, a H. Castro Neto, K. Matsuda, and G. Eda, "Photocarrier relaxation pathway in two-dimensional semiconducting transition metal dichalcogenides," *Nature Communications* (2014), 5, 4543.

199. D. Y. Qiu, F. H. Da Jornada, and S. G. Louie, "Optical spectrum of MoS_2: Many-body effects and diversity of exciton states," *Physical Review Letters* (2013), 111, 216805.

200. 2Dsemiconductors, "Electronic-mail correspondence: Raman and PL spectroscopy of CVD-MOS2," May 14 2015.

201. A. Splendiani, L. Sun, Y. Zhang, T. Li, J. Kim, C. Y. Chim, G. Galli, and F. Wang, "Emerging photoluminescence in monolayer MoS_2," *Nano Letters* (2010), 10, 1271.

202. W. Li, A. G. Birdwell, M. Amani, R. A. Burke, X. Ling, Y. Lee, X. Liang, L. Peng, C. a Richter, J. Kong, D. J. Gundlach, and N. V Nguyen, "Broadband optical properties of large-area monolayer CVD molybdenum disulfide," *Physical Review B* (2014), 90, 195434.

203. 2Dsemiconductors, "Electronic-mail correspondence: Raman spectroscopy of MOS2SOL," April 2 2015.

204. H. Li, Q. Zhang, C. C. R. Yap, B. K. Tay, T. H. T. Edwin, A. Olivier, and D. Baillargeat, "From bulk to monolayer MoS_2: Evolution of Raman scattering," *Advanced Functional Materials* (2012), 22, 1385.

205. A. Molina-Sánchez and L. Wirtz, "Phonons in single-layer and few-layer MoS_2 and WS_2," *Physical Review B* (2011), 84, 155413.

206. C. Y. Wang and G. Y. Guo, "Nonlinear Optical Properties of Transition-Metal

Dichalcogenide MX_2 (M = Mo, W; X = S, Se) Monolayers and Trilayers from First-Principles Calculations," *Journal of Physical Chemistry C* (2015), 119, 13268.

207. G. T. Forcherio, J. Riporto, J. R. Dunklin, Y. Mugnier, R. Le Dantec, L. Bonacina, and D. K. Roper, "Second order nonlinear coefficient of monolayer transition metal disulfides measured by Hyper Rayleigh Scattering," in preparation.

208. E. Hendrickx, K. Clays, and A. Persoons, "Hyper-Rayleigh Scattering in Isotropic Solution," *Accounts of Chemical Research* (1998), 31, 675.

209. R. Le Dantec, Y. Mugnier, G. Djanta, L. Bonacina, J. Extermann, L. Badie, C. Joulaud, M. Gerrmann, D. Rytz, J. P. Wolf, and C. Galez, "Ensemble and Individual Characterization of the Nonlinear Optical Properties of ZnO and BaTiO3 Nanocrystals," *Journal of Physical Chemistry C* (2011), 115, 15140.

210. C. Joulaud, Y. Mugnier, G. Djanta, M. Dubled, J.-C. Marty, C. Galez, J.-P. Wolf, L. Bonacina, and R. Le Dantec, "Characterization of the nonlinear optical properties of nanocrystals by Hyper Rayleigh Scattering," *Journal of Nanobiotechnology* (2013), 11, S1.

211. K. Das, A. Uppal, R. K. Saini, G. K. Varshney, P. Mondal, and P. K. Gupta, "Hyper-Rayleigh scattering from gold nanoparticles: Effect of size and shape," *Spectrochimica Acta Part A: Molecular and Biomolecular Spectroscopy* (2014), 128, 398.

212. S. Houbrechts, K. Clays, A. Persoons, Z. Pikramenou, and J. M. Lehn, "Hyper-Rayleigh scattering investigation of nitrobenzyl pyridine model compounds for optical modulation of the hyperpolarisability," *Chemical Physics Letters* (1996), 258, 485.

213. F. L. Huyskens, P. L. Huyskens, and A. P. Persoons, "Solvent dependence of the first hyperpolarizability of p-nitroanilines: Differences between nonspecific dipole-dipole interactions and solute-solvent H-bonds," *Journal of Chemical Physics* (1998), 108, 8161.

214. Y. Li, A. Chernikov, X. Zhang, A. Rigosi, H. M. Hill, A. M. van der Zande, D. A. Chenet, E.-M. Shih, J. Hone, and T. F. Heinz, "Measurement of the optical dielectric function of monolayer transition-metal dichalcogenides: MoS_2, $MoSe_2$, WS_2, and WSe_2," *Physical Review B* (2014), 90, 205422.

215. H. Yu, D. Talukdar, W. Xu, J. B. Khurgin, and Q. Xiong, "Charge-induced second-harmonic generation in bilayer WSe_2," *Nano Letters* (2015), 15, 5653.

216. R. C. Miller, "Optical second harmonic generation in piezoelectric Crystals," *Applied Physics Letters* (1964), 5, 17.

217. B. Mukherjee, F. Tseng, D. Gunlycke, K. Kumar, G. Eda, and E. Simsek, "Complex electrical permittivity of the monolayer molybdenum disulfide (MoS_2) in near UV and visible," *Optical Materials Express* (2015), 5, 447.

218. G. T. Forcherio, M. Benamara, and D. K. Roper, "Electron energy loss spectroscopy of hot electron transport between gold nanoantennas and molybdenum disulfide by plasmon

excitation," *Advanced Optical Materials* (2017), 5, 1600572.

219. A. Sobhani, A. Lauchner, S. Najmaei, C. Ayala-Orozco, F. Wen, J. Lou, and N. J. Halas, "Enhancing the photocurrent and photoluminescence of single crystal monolayer MoS_2 with resonant plasmonic nanoshells," *Applied Physics Letters* (2014), 104, 31112.

220. J. Miao, W. Hu, Y. Jing, W. Luo, L. Liao, A. Pan, S. Wu, J. Cheng, X. Chen, and W. Lu, "Surface plasmon-enhanced photodetection in few layer MoS_2 phototransistors with Au nanostructure arrays," *Small* (2015), 11, 2392.

221. J. Kern, A. Trügler, I. Niehues, J. Ewering, R. Schmidt, R. Schneider, S. Najmaei, A. George, J. Zhang, J. Lou, U. Hohenester, S. Michaelis de Vasconcellos, and R. Bratschitsch, "Nanoantenna-enhanced light–matter interaction in atomically thin WS_2," *ACS Photonics* (2015), 2, 1260.

222. L. Yang, D. Zhong, J. Zhang, Z. Yan, S. Ge, P. Du, J. Jiang, D. Sun, X. Wu, Z. Fan, S. A. Dayeh, and B. Xiang, "Optical properties of metal–molybdenum disulfide hybrid nanosheets and their application for enhanced photocatalytic hydrogen evolution," *ACS Nano* (2014), 8, 6979.

223. P. Zhang, M. Fujitsuka, and T. Majima, "Hot electron-driven hydrogen evolution using anisotropic gold nanostructure assembled monolayer MoS_2," *Nanoscale* (2017), 9, 1520.

224. X. Yang, W. Liu, M. Xiong, Y. Zhang, T. Liang, J. Yang, M. Xu, J. Ye, and H. Chen, "Au nanoparticles on ultrathin MoS_2 sheets for plasmonic organic solar cells," *Journal of Materials Chemistry A* (2014), 2, 14798.

225. S. Najmaei, A. Mlayah, A. Arbouet, C. Girard, J. Leotin, and J. Lou, "Plasmonic pumping of excitonic photoluminescence in hybrid MoS_2-Au nanostructures," *ACS Nano* (2014), 8, 12682.

226. B. Mukherjee, N. Kaushik, R. P. N. Tripathi, A. M. Joseph, P. K. Mohapatra, S. Dhar, B. P. Singh, G. V. P. Kumar, E. Simsek, and S. Lodha, "Exciton emission intensity modulation of monolayer MoS_2 via Au plasmon coupling," *Scientific Reports* (2017), 7, 41175.

227. U. Bhanu, M. R. Islam, L. Tetard, and S. I. Khondaker, "Photoluminescence quenching in gold-MoS_2 hybrid nanoflakes," *Scientific Reports* (2014), 4, 5575.

228. J. D. Torrey, T. L. Kirschling, and L. F. Greenlee, "Processing and characterization of nanoparticle coatings for quartz crystal microbalance measurements," *Journal of Research of the National Institute of Standards and Technology* (2015), 120, 1.

229. J. R. Dunklin, P. Lafargue, T. M. Higgins, G. T. Forcherio, M. Benamara, N. McEnvoy, D. K. Roper, J. N. Coleman, Y. Vaynzof, and C. Backes, "Exploiting the redox edge chemistry of liquid-exfoliated 2H-WS_2 to yield highly monolayer-rich gold decorated nanosheets in dispersion," in preparation.

230. G. T. Forcherio and D. K. Roper, "Spectral characteristics of noble metal nanoparticle-

molybdenum disulfide heterostructures," *Advanced Optical Materials* (2016), 4, 1288.

231. D. Merki and X. Hu, "Recent developments of molybdenum and tungsten sulfides as hydrogen evolution catalysts," *Energy & Environmental Science* (2011), 4, 3878.

232. X. Huang, Z. Zeng, S. Bao, M. Wang, X. Qi, Z. Fan, and H. Zhang, "Solution-phase epitaxial growth of noble metal nanostructures on dispersible single-layer molybdenum disulfide nanosheets," *Nature Communications* (2013), 4, 1444.

233. M. D. Malinsky, K. L. Kelly, G. C. Schatz, and R. P. Van Duyne, "Nanosphere lithography: effect of substrate on the localized surface plasmon resonance spectrum of silver nanoparticles," *J. Phys. Chem. B* (2001), 105, 2343.

234. J. Wu, W. Shi, and N. Chopra, "Optical properties of gold/multilayer-graphene/carbon nanotube hybrid materials," *Carbon* (2014), 68, 708.

235. V. Amendola, "Surface plasmon resonance of silver and gold nanoparticles in the proximity of graphene studied using the discrete dipole approximation method," *Physical Chemistry Chemical Physics* (2016), 18, 2230.

236. B. Mukherjee and E. Simsek, "Plasmonics enhanced average broadband absorption of monolayer MoS_2," *Plasmonics* (2016), 11, 285.

237. X. Yin, Z. Ye, D. a Chenet, Y. Ye, K. O'Brien, J. C. Hone, and X. Zhang, "Edge nonlinear optics on a MoS_2 atomic monolayer," *Science* (2014), 344, 488.

238. Y. Shi, J.-K. Huang, L. Jin, Y.-T. Hsu, S. F. Yu, L.-J. Li, and H. Y. Yang, "Selective decoration of Au nanoparticles on monolayer MoS_2 single crystals," *Scientific Reports* (2013), 3, 1839.

239. K. M. McCreary, A. T. Hanbicki, S. Singh, R. K. Kawakami, G. G. Jernigan, M. Ishigami, A. Ng, T. H. Brintlinger, R. M. Stroud, and B. T. Jonker, "The effect of preparation conditions on Raman and photoluminescence of monolayer WS_2," *Scientific Reports* (2016), 6, 35154.

240. D. DeJarnette and D. K. Roper, "Electron energy loss spectroscopy of gold nanoparticles on graphene," *Journal of Applied Physics* (2014), 116, 54313.

241. G. Li, C. Cherqui, N. W. Bigelow, G. Duscher, P. J. Straney, J. E. Millstone, D. J. Masiello, and J. P. Camden, "Spatially mapping energy transfer from single plasmonic particles to semiconductor substrates via STEM/EELS," *Nano Letters* (2015), 15, 3465.

242. A. Hoggard, L. Y. Wang, L. Ma, Y. Fang, G. You, J. Olson, Z. Liu, W. S. Chang, P. M. Ajayan, and S. Link, "Using the plasmon linewidth to calculate the time and efficiency of electron transfer between gold nanorods and graphene," *ACS Nano* (2013), 7, 11209.

243. T. Jensen, K. L. Kelly, A. Lazarides, and G. C. Schatz, "Electrodynamics of noble metal nanoparticles and nanoparticle clusters," *Journal of Cluster Science* (1999), 10, 295.

244. S. Butun, S. Tongay, and K. Aydin, "Enhanced light emission from large-area monolayer MoS_2 using plasmonic nanodisc arrays," *Nano Letters* (2015), 15, 2700.

245. A. Manjavacas, J. G. Liu, V. Kulkarni, and P. Nordlander, "Plasmon-induced hot carriers in metallic nanoparticles," *ACS Nano* (2014), 8, 7630.

246. L. Shao, X. Wang, H. Xu, J. Wang, J. Bin Xu, L. M. Peng, and H. Q. Lin, "Nanoantenna-sandwiched graphene with giant spectral tuning in the visible-to-near-infrared region," *Advanced Optical Materials* (2014), 2, 162.

247. M. Bosman, E. Ye, S. F. Tan, C. A. Nijhuis, J. K. W. Yang, R. Marty, A. Mlayah, A. Arbouet, C. Girard, and M.-Y. Han, "Surface plasmon damping quantified with an electron nanoprobe," *Scientific Reports* (2013), 3, 1312.

248. R. F. Egerton, "Electron energy-loss spectroscopy in the TEM," *Reports on Progress in Physics* (2009), 72, 16502.

249. A. Gloter, A. Douiri, M. Tencé, and C. Colliex, "Improving energy resolution of EELS spectra: an alternative to the monochromator solution," *Ultramicroscopy* (2003), 96, 385.

250. B. Goris, G. Guzzinati, C. Ferna, J. Pe, L. M. Liz-marza, A. Tru, U. Hohenester, J. Verbeeck, S. Bals, and G. Van Tendeloo, "Plasmon mapping in Au @ Ag nanocube assemblies," *Journal of Physical Chemistry C* (2014), 118, 15356.

251. M. Bosman and V. J. Keast, "Optimizing EELS acquisition," *Ultramicroscopy* (2008), 108, 837.

252. Z. Li, Y. Xiao, Y. Gong, Z. Wang, Y. Kang, S. Zu, P. M. Ajayan, P. Nordlander, and Z. Fang, "Active light control of the MoS_2 monolayer exciton binding energy," *ACS Nano* (2015), 9, 10158.

253. Y. Yu, Z. Ji, S. Zu, B. Du, Y. Kang, Z. Li, Z. Zhou, K. Shi, and Z. Fang, "Ultrafast plasmonic hot electron transfer in Au nanoantenna/MoS_2 heterostructures," *Advanced Functional Materials* (2016), 26, 6394.

254. J. J. Olivero and R. L. Longbothum, "Empirical fits to the Voigt line width: A brief review," *Journal of Quantitative Spectroscopy and Radiative Transfer* (1977), 17, 233.

255. I. H. Malitson, "Interspecimen comparison of the refractive index of fused silica," *Journal of the Optical Society of America* (1965), 55, 1205.

256. J. Brivio, D. T. L. Alexander, and A. Kis, "Ripples and layers in ultrathin MoS_2 membranes," *Nano Letters* (2011), 11, 5148.

257. M. Bar-Sadan, A. N. Enyashin, S. Gemming, R. Popovitz-Biro, S. Y. Hong, Y. Prior, R. Tenne, and G. Seifert, "Structure and stability of molybdenum sulfide fullerenes," *Journal of Physical Chemistry B* (2006), 110, 25399.

258. S. Zu, B. Li, Y. Gong, Z. Li, P. M. Ajayan, and Z. Fang, "Active control of plasmon-exciton coupling in MoS_2 -Ag hybrid nanostructures," *Advanced Optical Materials* (2016), 4, 1463.

259. C. Sönnichsen, T. Franzl, T. Wilk, G. von Plessen, and J. Feldmann, "Plasmon resonances in large noble-metal clusters," *New Journal of Physics* (2002), 4, 93.

260. H. S. Lee, M. S. Kim, Y. Jin, G. H. Han, Y. H. Lee, and J. Kim, "Efficient exciton-plasmon conversion in Ag nanowire/monolayer MoS_2 hybrids: direct imaging and quantitative estimation of plasmon coupling and propagation," *Advanced Optical Materials* (2015), 3, 943.

261. G. T. Forcherio, J. R. Dunklin, C. Backes, Y. Vaynzof, M. Benamara, and D. K. Roper, "Gold nanoparticles reduced onto tungsten disulfide nanosheet edges exhibit augmented plasmonic damping," in preparation.

262. S. Bandyopadhyay, S. Chattopadhyay, and A. Dey, "The protonation state of thiols in self-assembled monolayers on roughened Ag/Au surfaces and nanoparticles," *Physical Chemistry Chemical Physics* (2015), 17, 24866.

263. C. Battocchio, F. Porcaro, S. Mukherjee, E. Magnano, S. Nappini, I. Fratoddi, M. Quintiliani, M. V. Russo, and G. Polzonetti, "Gold manoparticles stabilized with aromatic thiols: interaction at the molecule–metal interface and ligand arrangement in the molecular shell investigated by SR-XPS and NEXAFS," *Journal of Physical Chemistry C* (2014), 118, 8159.

264. S. Thongrattanasiri, A. Manjavacas, and F. J. García de Abajo, "Quantum finite-size effects in graphene plasmons," *ACS Nano* (2012), 6, 1766.

265. Z. Zhang, J. Zhang, N. Chen, and L. Qu, "Graphene quantum dots: an emerging material for energy-related applications and beyond," *Energy & Environmental Science* (2012), 5, 8869.

266. S. Hwan Lee, D. Lee, W. Sik Hwang, E. Hwang, D. Jena, and W. Jong Yoo, "High-performance photocurrent generation from two-dimensional WS_2 field-effect transistors," *Applied Physics Letters* (2014), 104, 193113.

267. M. Garcia, J. de la Venta, P. Crespo, J. LLopis, S. Penadés, A. Fernández, and A. Hernando, "Surface plasmon resonance of capped Au nanoparticles," *Physical Review B* (2005), 72, 241403(R).

268. M. Minsky, "Microscopy apparatus," U.S. patent US3013467A (1957).

269. W. R. Zipfel, R. M. Williams, and W. W. Webb, "Nonlinear magic: multiphoton microscopy in the biosciences," *Nature Biotechnology* (2003), 21, 1369.

270. M. Sheik-Bahae, A. A. Said, T. H. Wei, D. J. Hagan, and E. W. Van Stryland, "Sensitive measurement of optical nonlinearities using a single beam," *IEEE Journal of Quantum Electronics* (1990), 26, 760.

271. R. Desalvo, D. J. Hagan, M. Sheik-Bahae, G. Stegeman, E. W. Van Stryland, and H. Vanherzeele, "Self-focusing and self-defocusing by cascaded second-order effects in KTP," *Optics Letters* (1992), 17, 28.

272. H. Kuzmany, *Solid-State Spectroscopy*, 2nd ed. (Springer, 2010), pg. 73, 94-97.

273. K. Chen, C. Durak, J. R. Heflin, and H. D. Robinson, "Plasmon-enhanced second-harmonic generation from ionic self-assembled multilayer films," *Nano Letters* (2007), 7, 254.

274. M. Ishifuji, M. Mitsuishi, and T. Miyashita, "Bottom-up design of hybrid polymer nanoassemblies elucidates plasmon-enhanced second harmonic generation from nonlinear optical dyes," *Journal of the American Chemical Society* (2009), 4418.

275. Y. Pu, R. Grange, C. L. Hsieh, and D. Psaltis, "Nonlinear optical properties of core-shell nanocavities for enhanced second-harmonic generation," *Physical Review Letters* (2010), 104, 207402.

276. G. Grinblat, M. Rahmani, E. Cortes, M. Caldarola, D. Comedi, S. A. Maier, and A. V. Bragas, "High-efficiency second harmonic generation from a single hybrid ZnO nanowire/Au plasmonic nano-oligomer," *Nano Letters* (2014), 14, 6660.

277. L. Sánchez-García, C. Tserkezis, M. O. Ramírez, P. Molina, J. J. Carvajal, M. Aguiló, F. Díaz, J. Aizpurua, and L. E. Bausá, "Plasmonic enhancement of second harmonic generation from nonlinear RbTiOPO4 crystals by aggregates of silver nanostructures," *Optics Express* (2016), 24, 8491.

278. H. Aouani, M. Rahmani, M. Navarro-Cía, and S. a Maier, "Third-harmonic-upconversion enhancement from a single semiconductor nanoparticle coupled to a plasmonic antenna," *Nature Nanotechnology* (2014), 9, 290.

279. B. Metzger, M. Hentschel, T. Schumacher, M. Lippitz, X. Ye, C. B. Murray, B. Knabe, K. Buse, and H. Giessen, "Doubling the efficiency of third harmonic generation by positioning ITO nanocrystals into the hot-spot of plasmonic gap-antennas," *Nano Letters* (2014), 14, 2867.

280. H. Aouani, M. Navarro-Cía, M. Rahmani, and S. A. Maier, "Unveiling the origin of third harmonic generation in hybrid ITO-plasmonic crystals," *Advanced Optical Materials* (2015), 3, 1059.

281. J. R. Heflin, M. T. Guzy, P. J. Neyman, K. J. Gaskins, C. Brands, Z. Wang, H. W. Gibson, R. M. Davis, and K. E. Van Cott, "Efficient, thermally stable, second order nonlinear optical response in organic hybrid covalent/ionic self-assembled films," *Langmuir* (2006), 22, 5723.

282. K. Geren, S. W. Liu, H. J. Zhou, Y. Zhang, R. Tian, and M. Xiao, "Second-order susceptibilities of ZnO nanorods from forward second-harmonic scattering," *Journal of Applied Physics* (2009), 105, 63531.

283. M. V. Pack, D. J. Armstrong, and A. V. Smith, "Measurement of the χ(2) tensors of KTiOPO4, KTiOAsO4, RbTiOPO4, and RbTiOAsO4 crystals," *Applied Optics* (2004), 43, 3319.

284. E. Kim, A. Steinbrück, M. T. Buscaglia, V. Buscaglia, T. Pertsch, and R. Grange, "Second-harmonic generation of single BaTiO3 nanoparticles down to 22 nm diameter," *ACS Nano* (2013), 7, 5343.

285. nanoComposix, Transmission UV-vis spectra and TEM analysis of lot#MGM1774.

286. Y.-Y. Chen, M. Dong, Z. Qin, X.-D. Wen, W. Fan, and J. Wang, "A DFT study on the adsorption and dissociation of methanol over MoS_2 surface," *Journal of Molecular Catalysis A: Chemical* (2011), 338, 44.

287. G. T. Forcherio, M. Benamara, and D. K. Roper, "Bright and dark surface plasmon resonances of gold nanoshells," in preparation.

288. G. T. Forcherio, L. Bonacina, J.-P. Wolf, and D. K. Roper, "Surface plasmon enhanced second harmonic generation from two-dimensional molybdenum disulfide," in preparation.

289. C. K. Chen, A. R. B. De Castro, and Y. R. Shen, "Surface-enhanced second-harmonic generation," *Physical Review Letters* (1981), 46, 145.

290. H. F. Wang, T. B. Huff, D. A. Zweifel, W. He, P. S. Low, A. Wei, and J. X. Cheng, "In vitro and in vivo two-photon luminescence imaging of single gold nanorods," *Proceedings of the National Academy of Sciences of the United States of America* (2005), 102, 15752.

291. M. Lippitz, M. A. van Dijk, M. Orrit, M. a Dijk, and M. Orrit, "Third-harmonic generation from single gold nanoparticles," *Nano Letters* (2005), 5, 799.

292. M. Eichelbaum, B. E. Schmidt, H. Ibrahim, and K. Rademann, "Three-photon-induced luminescence of gold nanoparticles embedded in and located on the surface of glassy nanolayers," *Nanotechnology* (2007), 18, 355702.

293. S. Palomba, M. Danckwerts, and L. Novotny, "Nonlinear plasmonics with gold nanoparticle antennas," *Journal of Optics A: Pure and Applied Optics* (2009), 11, 114030.

294. G. F. Walsh and L. D. Negro, "Engineering plasmon-enhanced Au light emission with planar arrays of nanoparticles," *Nano Letters* (2013), 13, 786.

295. G. F. Walsh and L. Dal Negro, "Enhanced second harmonic generation from Au nanoparticle arrays by femtosecond laser irradiation," *Nanoscale* (2013), 5, 7795.

296. A. Capretti, G. F. Walsh, S. Minissale, J. Trevino, C. Forestiere, G. Miano, and L. Dal Negro, "Multipolar second harmonic generation from planar arrays of Au nanoparticles," *Optics Express* (2012), 20, 15797.

297. M. McMahon, R. Lopez, R. Haglund Jr., E. Ray, and P. Bunton, "Second-harmonic

generation from arrays of symmetric gold nanoparticles," *Physical Review B* (2006), 73, 41401.

298. M. D. McMahon, D. Ferrara, C. T. Bowie, R. Lopez, and R. F. Haglund Jr., "Second harmonic generation from resonantly excited arrays of gold nanoparticles," *Applied Physics B* (2007), 87, 259.

299. G. Bachelier, J. Butet, I. Russier-Antoine, C. Jonin, E. Benichou, and P.-F. Brevet, "Origin of optical second-harmonic generation in spherical gold nanoparticles: Local surface and nonlocal bulk contributions," *Physical Review B* (2010), 82, 235403.

300. J. Nappa, G. Revillod, I. Russier-Antoine, E. Benichou, C. Jonin, and P. Brevet, "Electric dipole origin of the second harmonic generation of small metallic particles," *Physical Review B* (2005), 71, 165407.

301. J. Butet, J. Duboisset, G. Bachelier, I. Russier-Antoine, E. Benichou, C. Jonin, and P.-F. Brevet, "Optical second harmonic generation of single metallic nanoparticles embedded in a homogeneous medium," *Nano Letters* (2010), 10, 1717.

302. S. C. Kumar, G. K. Samanta, K. Devi, and M. Ebrahim-Zadeh, "High-efficiency, multicrystal, single-pass, continuous-wave second harmonic generation," *Optics Express* (2011), 19, 11152.

303. N. A. Chaitanya, A. Aadhi, S. C. Kumar, M. V. Jabir, G. K. Samanta, and M. Ebrahim-Zadeh, "Frequency-doubling of femtosecond pulses in “thick” nonlinear crystals with different temporal and spatial walk-off parameters," *IEEE Photonics Journal* (2016), 8, 6100613.

304. Y. Liu and X. Zhang, "Metamaterials: a new frontier of science and technology," *Chemical Society Reviews* (2011), 40, 2494.

305. M. H. Chou, I. Brener, M. M. Fejer, E. E. Chaban, and S. B. Christman, "1.5-μm-band wavelength conversion based on cascaded second-order nonlinearity in LiNbO3 waveguides," *IEEE Photonics Technology Letters* (1999), 11, 653.

306. K. Gallo, G. Assanto, and G. I. Stegeman, "Efficient wavelength shifting over the erbium amplifier bandwidth via cascaded second order processes in lithium niobate waveguides," *Applied Physics Letters* (1997), 71, 1020.

307. S. Kurimura, Y. Kato, M. Maruyama, Y. Usui, and H. Nakajima, "Quasi-phase-matched adhered ridge waveguide in LiNbO[sub 3]," *Applied Physics Letters* (2006), 89, 191123.

308. J. Lee, N. Nookala, J. S. Gomez-Diaz, M. Tymchenko, F. Demmerle, G. Boehm, M. C. Amann, A. Alù, and M. A. Belkin, "Ultrathin second-harmonic metasurfaces with record-high nonlinear optical response," *Advanced Optical Materials* (2016), 4, 664.

309. T. K. Fryett, K. L. Seyler, J. Zheng, C. Liu, X. Xu, and A. Majumdar, "Silicon photonic crystal cavity enhanced second-harmonic generation from monolayer WSe_2," *2D Materials*

(2016), 4, 15031.

310. C.-Y. Tsai, J.-W. Lin, C.-Y. Wu, P.-T. Lin, T.-W. Lu, and P.-T. Lee, "Plasmonic coupling in gold nanoring dimers: observation of coupled bonding mode," *Nano Letters* (2012), 12, 1648.

311. G. F. Walsh and L. Dal Negro, "Enhanced second harmonic generation by photonic-plasmonic Fano-type coupling in nanoplasmonic arrays," *Nano Letters* (2013), 13, 3111.

312. W. An, T. Zhu, and Q. Zhu, "Numerical investigation of radiative properties and surface plasmon resonance of silver nanorod dimers on a substrate," *Journal of Quantitative Spectroscopy and Radiative Transfer* (2014), 132, 28.

313. S. C. Quillin, C. Cherqui, N. P. Montoni, G. Li, J. P. Camden, and D. J. Masiello, "Imaging plasmon hybridization in metal nanoparticle aggregates with electron energy-loss spectroscopy," *Journal of Physical Chemistry C* (2016), 120, 20852.

314. A. Capretti, Y. Wang, N. Engheta, and L. Dal Negro, "Comparative study of second-harmonic generation from epsilon-near-zero indium tin oxide and titanium nitride nanolayers excited in the near-infrared spectral sange," *ACS Photonics* (2015), 2, 1584.

315. M. Navarro-Cia and S. A. Maier, "Broad-band near-infrared plasmonic nanoantennas for higher harmonic generation," *ACS Nano* (2012), 6, 3537.

316. K. Thyagarajan, S. Rivier, A. Lovera, and O. J. F. Martin, "Enhanced second-harmonic generation from double resonant plasmonic antennae," *Optics Express* (2012), 20, 12860.

317. P. Ginzburg, A. Krasavin, Y. Sonnefraud, A. Murphy, R. J. Pollard, S. A. Maier, and A. V. Zayats, "Nonlinearly coupled localized plasmon resonances: Resonant second-harmonic generation," *Physical Review B* (2012), 86, 85422.

318. K. Thyagarajan, J. Butet, and O. J. F. Martin, "Augmenting second harmonic generation using Fano resonances in plasmonic systems," *Nano Letters* (2013), 13, 1847.

319. M. Celebrano, X. Wu, M. Baselli, S. Großmann, P. Biagioni, A. Locatelli, C. De Angelis, G. Cerullo, R. Osellame, B. Hecht, L. Duò, F. Ciccacci, and M. Finazzi, "Mode matching in multiresonant plasmonic nanoantennas for enhanced second harmonic generation," *Nature Nanotechnology* (2015), 10, 412.

320. H. Taghinejad, S. Hamed Shams-Mousavi, Y. Gong, M. Taghinejad, A. A. Eftekhar, P. Ajayan, and A. Adibi, "Lattice plasmon induced large enhancement of excitonic emission in monolayer metal dichalcogenides," *Plasmonics* (2016), 1.

Appendix A: Description of Research for Popular Publication

The global progression towards “green energy” has reduced fossil fuel consumption by improving performance and consumer acceptance of alternative energy technologies, such as solar cells and hybrid cars. However almost 60% of energy generated by traditional and alternative methods is wasted away as heat, never to be used in our smart phones or car engines. Gregory Forcherio, a student at the University of Arkansas under the guidance of Dr. D. Keith Roper, is working to recapture that wasted heat energy and use it to power the next generation of technology.

Recycling heat energy is not a new idea. Products developed and tested to date, from body-heat powered watches to combustion engines without alternators, were unsuccessful because of efficiency limitations inherent to the materials that were used. Forcherio and Roper hypothesize entirely new ways to recover heat energy.

At the heart of this new technology are engineered nano-sized structures, called nanoparticles, which can guide light and heat in ways not typically seen in nature. Decorating specific materials with intrinsic frequency conversion properties, such as atomically-thick molybdenum disulfide, a common machining lubricant, with nanoparticles has the ability to transform heat into optical or electronic signals. “Nanoparticles have the ability to focus light for strengthening conversion of heat radiation frequencies to telecom frequencies,” says Forcherio.

Still in the prototyping stage, the combination of nanoparticles and atomically thick materials can potentially revolutionize the way our devices are powered and function. Personal power networks, battery-less medical monitors, and faster computers are a few examples of where Forcherio and Roper’s efforts could lead down the road.

Appendix B: Newly Created Intellectual Property

The following list indicates newly created intellectual items.

1. Method to simulate optical interactions between nanoantennas and arbitrary, multi-scale, complex dielectric materials by discrete dipole approximation
2. Method to simulate optical properties for two-dimensional regular lattices of arbitrarily-shaped nanoantennas embedded in inhomogeneous, complex dielectric environments
3. Method to measure orientation-averaged second nonlinear coefficients (β and $\chi^{(2)}$) for two-dimensional materials by Hyper Rayleigh Scattering
4. Mechanisms for heat recycling/rejection from temperature gradients by (i) plasmonic hot electron transport and/or (ii) multi-order nonlinear frequency conversion

Appendix C: Potential Patent & Commercialization Aspects

C.1 Patentability of Intellectual Property

Potential patentability of each item in Appendix B was considered. It was determined that one of the items could be patented. This is described in detail for each item below:

1. An open-source computational technique based on Maxwell's equations was used to simulate optical properties of nanocomposites featuring two-dimensional material components. The approach was published by John Wiley & Sons on June 8, 2016 [G. T. Forcherio *et al*., *Adv. Opt. Mater.* (2016), 4, 1288]. The item is patentable for one month. It is of the opinion of the author pursuit of a patent is not warranted.
2. Use of an established modeling technique to synthesize the coupled and discrete dipole approximations was extended to account for inhomogeneous, complex dielectric environments. The approach was published by Elsevier on August 4, 2015 [G. T. Forcherio *et al*., *J. Quant. Spectrosc. Radiat. Transfer* (2015), 166, 93]. The item is no longer patentable. It is of the opinion of the author pursuit of a patent was unwarranted.
3. An established technique in nonlinear optical characterization was used for the first time to examine nonlinear coefficients of a two-dimensional material. Intellectual property is shared in part with University of Geneva in Switzerland and University of Savoy in France. It is of the opinion of the author pursuit of a patent is not warranted.
4. Two mechanisms were proposed for passive heat management (e.g., rejection or recycling) applications utilizing quantum electrodynamic processes in a novel way. This item could be patentable. It is of the opinion of the author further studies are required to examine practicality and gauge economic feasibility prior to pursuit of a patent.

C.2 Commercialization Aspects of Intellectual Property

Commercialization opportunities for each item in Appendix B was considered. It was determined that one of the items exhibited commercial appeal. These opportunities are described in detail for each item below:

1. The underlying computational algorithm is open-source freeware and thus does not exhibit commercial appeal.
2. The individual, underlying computational algorithms are open-source freeware and thus do not exhibit commercial appeal. A streamlined software package could be of interest to a minute subset of the scientific community, but is too limited in its applicability to appeal to a broader scientific community.
3. The measurement technique is highly accessible in optics laboratories featuring pulsed lasers and does not require special optical components or apparatuses. This item, in of itself, does not exhibit commercial appeal.
4. Design and implementation of novel nanomaterials for thermal energy management exhibits commercial appeal as an alternative to thermoelectric materials. However, it is of the opinion of the author the path to market timeline, at this stage, exceed the 20 year patent term of protection.

C.3 Possible Prior Disclosure of Intellectual Property

Disclosure of each item in Appendix B which could impact patentability was considered. These disclosures described in detail for each item below:

1. The underlying software is open-source. The approach was published by John Wiley & Sons on June 8, 2016 [G. T. Forcherio *et al*., *Adv. Opt. Mater.* (2016), 4, 1288] and SPIE

on September 16, 2016 [G. T. Forcherio *et al*., Proceedings of SPIE 9919, Nanophotonic Materials XIII, 991911]. The approach was presented to an audience without non-disclosure agreements on August 31, 2016 at the SPIE Optics + Photonics conference. A computational tool enabling other researchers to re-create published results and generate new results was published open-source on nanoHUB [M. Seeram *et al*., nanoHUB, DOI: 10.4231/D3J960B3D].

2. The underlying software used are open-source, although one was modified to obtain the intellectual property. The approach was published by Elsevier on August 4, 2015 [G. T. Forcherio *et al*., *J. Quant. Spectrosc. Radiat. Transfer* (2015), 166, 93] and SPIE on March 14, 2016 [G. T. Forcherio *et al*., Proceedings of SPIE 9756, Photonic and Phononic Properties of Engineered Nanostructures VI, 975615]. The approach was presented to an audience without non-disclosure agreements on February 17, 2016 at the SPIE Photonics West conference.
3. Experiments and data interpretation were conducted in collaboration with colleagues at University of Geneva in Switzerland and University of Savoy Mont Blanc in France.
4. This item has not been disclosed publically.

Appendix D: Broader Impact of Research

D.1 Applicability of Research Methods to Other Problems

Theoretical and experimental methods employed in this work are directly applicable to research problems throughout the nanoscience community. The open-source discrete dipole approximation (DDA) is readily available to describe electrodynamic behavior of non-metallic nanoantennas, two-dimensional materials beyond transition metal dichalcogenides (e.g., phosphorene), and bulk media. Electron energy loss spectroscopy (EELS) may be used for chemical mapping/identification of materials or studying time-resolved phase change mechanisms. Identification of plasmon decay pathways not yet known is possible. Multi-photon confocal microscopy can three-dimensionally reconstruct or track nanoparticle-labeled biomolecules.

D.2 Impact of Research Results on U.S. & Global Society

Recovering and utilization of waste heat, which comprises 60% of all generated energy, complements policies set by the International Energy Agency to save 160 gigatonnes of projected carbon emissions by 2033. Reducing power requirements of optoelectronic devices and developing emission-less energy sources is advocated by the U.S. Department of Energy. Convergence of thermal energy harvesting and electronics hybridized with optical data transmission could manifest as novel communication devices, wearable medical monitors, and personal power networks with performance unprecedented in the commercial market.

Improved fundamental understanding of plasmon excitation and decay in various environments (e.g., carrier channels in CMOS transistors or biological analyte) accelerates optimization of nanoantenna-based materials into practical devices. Mitigation of ohmic losses in noble metal plasmons to exploit radiative or hot electron damping could provide new avenues towards improved solar photovoltaics, photodetectors, and biosensors with documented plasmon enhancement. Significant ohmic losses has, to date, prevented their advancement into commercial markets. An experimental and theoretical framework was described herein to assess plasmonic losses in functional devices.

D.3 Impact of Research Results on the Environment

The aim of energy recycling schemes is reduce fossil fuel dependence and shrink the global carbon footprint. Recycling thermal energy within optoelectronics by heat rejection and/or transduction into electric or optical signals could lower effective electric grid power consumption. In niche applications, it is also possible to disrupt reliance on batteries through advancing photocatalytic solar fuel generation. Batteries are known to leak heavy metals (e.g., lithium and lead) into the Earth’s soil and water as a consequence of improper disposal. Research is ongoing to determine environmental toxicity of nanoparticles; no adverse effects are known to date. Recent work on bulk silver and copper suggests nanoparticle formation is a naturally occurring process in natural environments.

Appendix E: Microsoft Project for Ph.D. Degree Plan

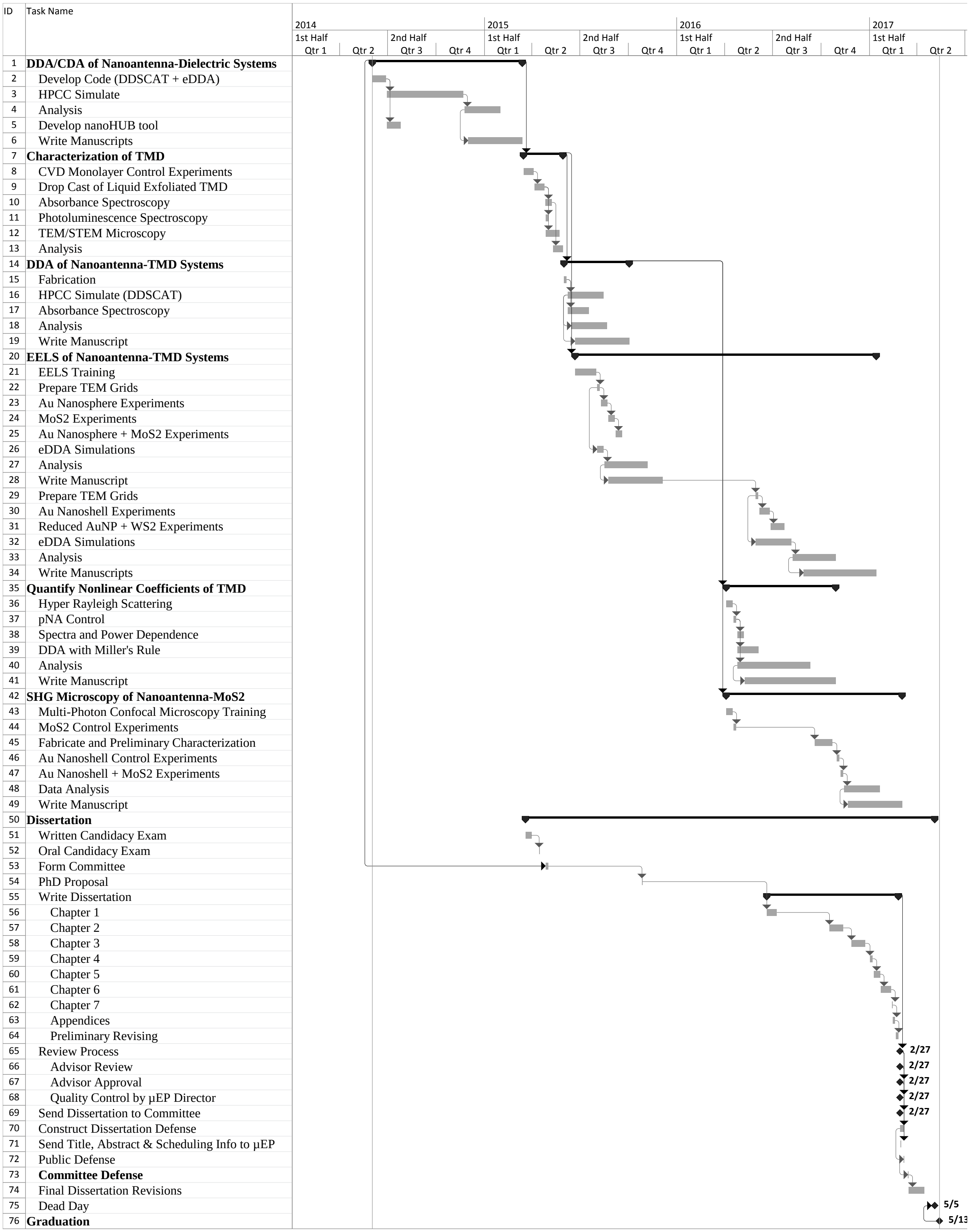

ID	Task Name
1	**DDA/CDA of Nanoantenna-Dielectric Systems**
2	Develop Code (DDSCAT + eDDA)
3	HPCC Simulate
4	Analysis
5	Develop nanoHUB tool
6	Write Manuscripts
7	**Characterization of TMD**
8	CVD Monolayer Control Experiments
9	Drop Cast of Liquid Exfoliated TMD
10	Absorbance Spectroscopy
11	Photoluminescence Spectroscopy
12	TEM/STEM Microscopy
13	Analysis
14	**DDA of Nanoantenna-TMD Systems**
15	Fabrication
16	HPCC Simulate (DDSCAT)
17	Absorbance Spectroscopy
18	Analysis
19	Write Manuscript
20	**EELS of Nanoantenna-TMD Systems**
21	EELS Training
22	Prepare TEM Grids
23	Au Nanosphere Experiments
24	MoS2 Experiments
25	Au Nanosphere + MoS2 Experiments
26	eDDA Simulations
27	Analysis
28	Write Manuscript
29	Prepare TEM Grids
30	Au Nanoshell Experiments
31	Reduced AuNP + WS2 Experiments
32	eDDA Simulations
33	Analysis
34	Write Manuscripts
35	**Quantify Nonlinear Coefficients of TMD**
36	Hyper Rayleigh Scattering
37	pNA Control
38	Spectra and Power Dependence
39	DDA with Miller's Rule
40	Analysis
41	Write Manuscript
42	**SHG Microscopy of Nanoantenna-MoS2**
43	Multi-Photon Confocal Microscopy Training
44	MoS2 Control Experiments
45	Fabricate and Preliminary Characterization
46	Au Nanoshell Control Experiments
47	Au Nanoshell + MoS2 Experiments
48	Data Analysis
49	Write Manuscript
50	**Dissertation**
51	Written Candidacy Exam
52	Oral Candidacy Exam
53	Form Committee
54	PhD Proposal
55	Write Dissertation
56	Chapter 1
57	Chapter 2
58	Chapter 3
59	Chapter 4
60	Chapter 5
61	Chapter 6
62	Chapter 7
63	Appendices
64	Preliminary Revising
65	Review Process
66	Advisor Review
67	Advisor Approval
68	Quality Control by μEP Director
69	Send Dissertation to Committee
70	Construct Dissertation Defense
71	Send Title, Abstract & Scheduling Info to μEP
72	Public Defense
73	**Committee Defense**
74	Final Dissertation Revisions
75	Dead Day
76	**Graduation**

Appendix F: Identification of Software Used for Dissertation Generation

Computer #1:
- Model: Dell Precision T3500
- Serial Number: DCRB3L1
- Location: Institute for Nanoscience and Engineering, Room 301
- Owner: NanoBio Photonics Group, University of Arkansas

Software #1:
- Name: Microsoft Office, Professional Plus 2013
- Purchased By: Department of Chemical Engineering, University of Arkansas
- License: 00216-40000-00000-AA837

Software #2:
- Name: Mendeley (v1.16)
- Purchased By: Gregory T. Forcherio
- License: Freeware

Software #3:
- Name: Matlab R2015b (v8.6)
- Purchased By: Department of Chemical Engineering, University of Arkansas
- License: 601103

Computer #2:
- Model: ASUS VivoBook X202E
- Serial Number: D2N0BC006118059
- Location: Home
- Owner: Gregory T. Forcherio

Software #1:
- Name: Microsoft Office 365, 2013
- Purchased By: Gregory T. Forcherio
- License: 00201-10029-87936-AA207

Software #2:
- Name: Mendeley (v1.16)
- Purchased By: Gregory T. Forcherio
- License: Freeware

Software #3:
- Name: Matlab R2015b (v8.6, student version)
- Purchased By: Gregory T. Forcherio

Appendix G: Published Peer-Reviewed Articles & Conference Proceedings

Peer-Reviewed Articles

- **G. T. Forcherio**, M. Benamara, and D. K. Roper, “Electron energy loss spectroscopy of hot electron transport between gold nanoantennas and molybdenum disulfide by plasmon excitation,” Advanced Optical Materials (2017), 5, 1600572.

- J. R. Dunklin, C. Bodinger, **G. T. Forcherio**, and D. K. Roper, “Describing plasmonic extinction in optically dense, multi-scale gold nanoparticle-polymer films,” Journal of Nanophotonics (2017), 11, 016002.

- **G. T. Forcherio**, D. DeJarnette, M. Benamara, and D. K. Roper, “Electron energy loss spectroscopy of surface plasmon resonances on aberrant gold nanostructures,” Journal of Physical Chemistry C (2016), 120, 24950.

- **G. T. Forcherio**, and D. K. Roper, “Spectral characteristics of noble metal nanoparticle-molybdenum disulfide heterostructures,” Advanced Optical Materials (2016), 4, 1288.

- **G. T. Forcherio**, P. Blake, M. Seeram, D. DeJarnette, and D. K. Roper, “Coupled dipole plasmonics of nanoantennas in discontinuous, complex dielectric environments,” Journal of Quantitative Spectroscopy and Radiative Transfer (2015), 166, 93.

- J. R. Dunklin, **G. T. Forcherio**, and D. K. Roper, “Gold nanoparticle-polydimethylsiloxane films reflect light internally by optical diffraction and Mie scattering,” Materials Research Express (2015), 2, 085005.

- J. R. Dunklin, **G. T. Forcherio**, K. R. Berry, and D. K. Roper, “Plasmon optics and thermal dissipation in nanocomposite thin films,” MRS Proceedings (2015), 1788.

- **G. T. Forcherio**, P. Blake, D. DeJarnette, and D. K. Roper, “Nanoring structure, spacing, and local dielectric sensitivity for plasmonic resonances in Fano resonant square lattices,” Optics Express (2014), 22, 17791.

- P. Blake, S. Kühne, **G. T. Forcherio**, and D. K. Roper, “Diffraction in nanoparticle lattices increases sensitivity of localized surface plasmon resonance to refractive index changes,” Journal of Nanophotonics (2014), 8, 083084.

- M. Lisunova, X. Wei, D. DeJarnette, **G. T. Forcherio**, K. R. Berry, P. Blake, and D. K. Roper, “Photothermal response of plasmonic nanoconglomerates in films assembled by electroless plating,” RSC Advances (2014), 4, 20894.

- J. R. Dunklin, **G. T. Forcherio**, K. R. Berry, and D. K. Roper, “Gold nanoparticle-polydimethylsiloxane thin films enhance thermoplasmonic heating by internal reflection,” Journal Physical Chemistry C (2014), 118, 7523.

- J. R. Dunklin, **G. T. Forcherio**, and D. K. Roper, “Geometric optics of gold nanoparticle-polydimethylsiloxane thin film systems,” Optical Materials Express (2014), 4, 375.

- D. DeJarnette, P. Blake, **G. T. Forcherio**, and D. K. Roper, “Far-field Fano resonance in nanoring lattices modeled from extracted, point dipole polarizability,” Journal of Applied Physics (2014), 115, 024306.

- M. Lisunova, J. C. Norman, P. Blake, **G. T. Forcherio**, D. F. DeJarnette, and D. K. Roper, “Modulation of plasmonic Fano resonance by the shape of the nanoparticles in ordered arrays,” Journal of Physics D: Applied Physics (2013), 46, 485103.

- J. R. Dunklin, **G. T. Forcherio**, K. R. Berry, and D. K. Roper, “Asymmetric reduction of gold nanoparticles into thermoplasmonic polydimethylsiloxane thin films,” ACS Applied Materials and Interfaces (2013), 5, 8457.

- **G. T. Forcherio** and D. K. Roper, “Optical attenuation of plasmonic nanocomposites within photonic devices,” Applied Optics (2013), 52, 6417.

Conference Proceedings Published

- **G. T. Forcherio**, M. Benamara, and D.K. Roper, “Plasmon excitation and damping in noble metal nanoparticle-MoS_2 nanocomposites,” Proceedings of SPIE 9919, Nanophotonic Materials XIII, 991911.

- J. R. Dunklin, **G. T. Forcherio**, K. R. Berry, and D. K. Roper, ”Interfacial reflection enhanced optical extinction and thermal dynamics in polymer nanocomposite films,” Proceedings of SPIE 9919, Nanophotonic Materials XIII, 99190X.

- D. K. Roper, **G. T. Forcherio**, and D. DeJarnette, “Compact simulation guides subnanometer, femtosecond measure of energy transfer between quasiparticles and hot carriers at interfaces between metals and two dimensional materials,” Proceedings of SPIE 9923, Physical Chemistry of Interfaces and Nanomaterials XV, 992312.

- D. K. Roper, **G. T. Forcherio**, and D. DeJarnette, “Interactions between confined fields and carriers at interfaces between two dimensional materials and nanoscale metal architectures,” Proceedings of SPIE 9924, Low Dimensional Materials and Devices 2016, 992408. [Invited]

- **G. T. Forcherio**, P. Blake, M. Seeram, D. DeJarnette, and D. K. Roper, “Complex dielectric and geometry influences on plasmon excitation and energy transfer in nanocomposite systems,” Proceedings of SPIE 9756, Photonic and Phononic Properties of Engineered Nanostructures VI, 975615.

- J. R. Dunklin, **G. T. Forcherio**, K. R. Berry, and D. K. Roper, “Plasmon optics and thermal dissipation in nanocomposite thin films,” MRS 2015 Spring Meeting Proceedings, 1788.

- **G. T. Forcherio** and D. K. Roper, “Optical attenuation of plasmonic Au-PDMS nanocomposite thin-film devices,” Proceedings of SPIE 9161, Nanophotonic Materials XI, 916115.

- **G. T. Forcherio**, D. DeJarnette, P. Blake, and D. K. Roper, “Polarizability extraction for rapid computation of Fano resonance in nanoring lattices,” Proceedings of SPIE 9163, Plasmonics: Metallic Nanostructures and Their Optical Properties XII, 91633O.

- J. R. Dunklin, **G. T. Forcherio**, K. R. Berry, and D. K. Roper, “Asymmetric reduction of gold nanoparticles into polydimethylsiloxane thin films,” Proceedings of SPIE 9163, Plasmonics: Metallic Nanostructures and Their Optical Properties XII, 916330.

- J. R. Dunklin, **G. T. Forcherio**, and D. K. Roper, “Geometric optics of gold nanoparticle-polydimethylsiloxane thin films,” Proceedings of SPIE 9163, Plasmonics: Metallic Nanostructures and Their Optical Properties XII, 916332.

- D. K. Roper, D. DeJarnette, **G. T. Forcherio**, J. R. Dunklin, K. R. Berry, G.-G. Jang, M. Lisunova, P. A. Blake, and W. Ahn, “Electron optics of nanoplasmonic metamaterials in bio/opto theranostics,” Proceedings of SPIE 9166, Biosensing and Nanomedicine VII, 91660L. [Invited]

Manuscripts Planned or Submitted for Publication

- **G. T. Forcherio**, J. R. Dunklin, M. Benamara, C. Backes, Y. Vaynzof, and D. K. Roper, “Gold nanoparticles physicochemically bonded onto tungsten disulfide nanosheet edges exhibit augmented plasmon damping.”

- **G. T. Forcherio**, J. Riporto, J. R. Dunklin, Y. Mugnier, R. Le Dantec, L. Bonacina, and D. K. Roper, “Second order nonlinear coefficient of monolayer transition metal disulfides measured by Hyper Rayleigh Scattering.”

- **G. T. Forcherio**, M. Benamara, and D. K. Roper, “Bright and dark surface plasmon resonances of gold nanoshells.”

- **G. T. Forcherio**, L. Bonacina, J. P. Wolf, and D. K. Roper, “Surface plasmon enhanced nonlinear second harmonic generation from two-dimensional molybdenum disulfide.”

- J. R. Dunklin, **G. T. Forcherio**, and D. K. Roper, “Location dependent spectral characteristics of gold nanoparticle-decorated tungsten disulfide nanostructures.”

- V. Bejugam, **G. T. Forcherio**, R. T. French III, and D. K. Roper, “Gold reduction and deposition on soda lime glass from bulk colloidal solutions.”

- T. V. Howard, J. R. Dunklin, **G. T. Forcherio**, and D. K. Roper, “Thermoplasmonic dissipation in gold nanoparticle-polyvinylpyrrolidone thin films.”

- R. T. French III, V. Bejugam, **G. T. Forcherio**, and D. K. Roper, “Optical characteristics of a lattice resonance supported by plasmonic nanoparticles deposited sparsely in a nanoimprinted polymer.”

- J. R. Dunklin, P. Lafargue, T. M. Higgins, **G. T. Forcherio**, M. Benamara, N. McEvoy, D. K. Roper, J. N. Coleman, Y. Vaynzof, and C. Backes, “Exploiting the redox edge chemistry of liquid-exfoliated 2H-WS_2 to yield highly monolayer-rich gold decorated nanosheets in dispersion."

- K. R. Berry, D. K. Roper, J. R. Dunklin, C. Chambers, and **G. T. Forcherio**, "Programmable geometry- and composition-dependent thermal dynamics using refined plasmonic metal-polymer thin films."